Nano-scale heterogeneity of carbon chemical structures in structural materials studied by scanning transmission X-ray microscopy

DOCTORAL THESIS

Takayuki HARANO

Department of Materials Structure Science
School of High Energy Accelerator Science
The Graduate University for Advanced Studies,
SOKENDAI

December, 2020

走査型透過 X 線顕微鏡による構造材料中炭素の化学構造の不均一性に関する研究

博士論文

原野　貴幸

総合研究大学院大学
高エネルギー加速器科学研究科
物質構造科学専攻

2020 年 12 月

Preface

  This thesis marks the completion of my studies under the supervision of Professor Masao Kimura and Assistant Professor Yasuo Takeichi from 2018 to 2021 while I have been a student of Department of Materials Structure Science, School of High Energy Accelerator Science, The Graduate University for Advanced Studies, SOKENDAI.

  This thesis is organized in the main 8 chapters. Chapter 1 describes the general introduction to the importance of chemical structure analysis of carbon for structural materials, and the motivation and proposes of the present study on structural materials using scanning transmission X-ray microscopy (STXM). The experimental methods of STXM and other characterization techniques are described in Chapter 2. In Chapter 3, comparison of π-orbital oriented domains between PAN- and pitch-based carbon fibers is described. The author describes mapping method of π-orbital oriented domains in a pitch-based carbon fiber and visualization of stress concentration points between π-orbital oriented domains in Chapter 4. In Chapter 5, the author describes development of an azimuthal-rotation sample holder for orbital orientation analysis in Photon Factory. Observation results of interface between resin and carbon fiber in carbon fiber reinforced plastics are written in Chapter 6. Chapter 7 describes STXM study on Fe-C alloy to consider the difference of carbon chemical state depended on the microstructure types of carbides. Finally, Chapter 8 is devoted to summary and future prospects.

<div align="right">

December, 2020

Takayuki HARANO

</div>

Abstract

Carbon plays an important role not only in functional materials but also in structural materials. The mechanical properties (among electronic, mechanical, and optical properties) of carbon matrices and carbon-containing materials are determined by their multiscale structures, i.e., the atomic arrangement of carbon atoms (crystal, layer, and domain structures), the chemical structures (the types of chemical bonds, molecular orbital orientation, and electronic states), and the structural heterogeneity (spatial distribution and regularity/irregularity). On the other hand, only a small amount of carbon (typically a low percentage) in steel contributes significantly to its mechanical properties as an additive element in multiscale microstructures. The chemical structure of iron as well as the additive elements is one of the essential factors that determine the mechanical properties of steel. Despite its importance, there have been fewer reports in terms of this factor compared with other factors: (1) the types of crystal phases, size, and spatial distributions of the grains and crystal orientations; (2) the size and spatial distributions of defects, such as the atomic vacancies, dislocations, and voids; (3) the morphology of the additive elements (the interstitial solid solution, substitution solid solution, and compounds) and their spatial distributions (segregation and uniform dispersion); and (4) the chemical structure of iron and the additive elements.

Although many studies have investigated the relationship between the crystal structures/microstructures and the mechanical properties in structural materials, only a few studies have investigated the relationship between the heterogeneity of chemical structures and mechanical properties in structural materials. In this study, to identify the essential role of carbon in its chemical structure, the author has studied the following two types of materials: (A) carbon fibers (CFs) and carbon-fiber-reinforced plastics (CFRPs), which are typical structural composites in which carbon is the main component, and (B) steel as structural materials in which carbon is employed as an additive element to control the mechanical properties. Although investigations on the chemical structures of carbon and its spatial distribution have been essential for improving their mechanical properties, they have rarely been studied. One reason is experimental difficulties in revealing the chemical structures in materials with nano- to micro-scales through conventional analytical methods. Therefore, by employing a

relatively newly developed spectro-microscopy technique, scanning transmission X-ray microscopy (STXM), the author has attempted to establish analytical methods to quantify the heterogeneity of the chemical structure of structural materials at the nanometer scale.

It is known that the heterogeneity of the chemical structure can determine the mechanical properties of structural materials. Structural materials exhibit a multiscale hierarchy. The mechanical properties of structural materials can be understood by examining not only single crystals or single phases but also hierarchical microstructures and their heterogeneity. The author focused on the relationship between the types and heterogeneity of the chemical structures and the mechanical properties, and aimed to establish analytical methods to identify their relationships. Furthermore, the author also considered that this study's findings could have industrial benefits, such as guidelines for selecting raw materials, new processes, and insights for developing high-quality materials.

The chemical structures of carbon in carbon composite materials (polyacrylonitrile (PAN) and pitch-based CFs and CFRP) and Fe–C alloy studied by STXM with linear polarized X-rays and azimuthal sample rotation were investigated. It was shown that STXM is one of the most powerful analytical approaches for characterizing the heterogeneity in the chemical structure of carbon on the nanometer scale. Studies on the relationship between the spatial distribution of the chemical structure in the microstructure and the macroscopic mechanical properties have revealed essential factors for controlling macroscopic mechanical properties: (a) the distribution of the π-orbital orientation or the π-orbital–oriented domains in CFs and CFRP, and (b) the chemical states of carbon as a solid solution in iron and/or as a secondary phase (Fe_3C).

These findings, obtained through STXM with a high spatial resolution, have shown that the analytical results from the microstructures and chemical structures can be different and that, in such a case, the chemical structures will be essential in understanding their mechanical properties. Thus, the approaches developed in this study provide new insights and methodologies to understand the macroscopic mechanical properties of structural materials in terms of chemical structures.

Contents

Chapter 1

General Introduction

1.1 Background

Carbon is one of the most important constituent elements of living organisms, including plants and humans. As the main constituent of coal and natural gas, carbon plays an important role in energy sustainability. Additionally, carbon exists in various materials, including functional and structural materials. As a functional material, carbon is utilized in electric-field transistors (Heinze *et al.*, 2002), electroluminescence devices (Misewich *et al.*, 2004) that utilize carbon nanotubes (Iijima, 1991), graphene (Novoselov *et al.*, 2004), and photodetectors (Qui *et al.*, 2005). Carbon materials are applied as negative electrodes in various batteries (Kamali *et al.*, 2010), and recently, they have been applied as flexible transparent electrodes (Wu *et al.*, 2004). Conversely, for structural material, carbon is the main constituent of rubber, resins, carbon fibers (CFs), and carbon fiber-reinforced plastics (CFRPs). CFRPs are characterized by their high strength per unit mass and small coefficient of thermal expansion compared to other materials. Therefore, they are widely utilized as structural materials in aircrafts and industrial equipment (Soo-Jin, 2018). Furthermore, carbon is one of the most important elements that controls the strength and formability of steel, which is widely considered as one of the most important infrastructure materials with various applications (including in automobiles, shipbuilding, transportation equipment, building materials, infrastructure (bridges, power generation), and food containers) (Pickering *et al.*, 1978).

The mechanical properties of structural materials are determined by integrating the characteristics of each of the multiple spatial scales. For example, in the case of CFRPs, as shown in Fig. 1.1, (I) in millimeter scale, the arrangement and direction of CFs in the resin, (II) in micrometer scale, surface cracks and internal defects of CFs, and (III) in nanometer scale, the crystallite size of the graphite microcrystals, the size of the domain formed by assembling them, the orientation distribution in CFs, and the adhesion state between the resin and the

CFs, determine the mechanical properties of CFRPs. in the case of steel, as shown in Fig. 1.1, (I) in millimeter scale, the distribution of crystal grain size and crystal orientation, (II) in micrometer scale, the distribution of types and sizes of precipitates and defects, and (III) in nanometer scale, the characteristics of grain boundaries between ferrite and ferrite/carbide, determine the mechanical properties of steel. In this study, the author focused on the chemical states ((III) for CFRPs and steel) that have not been sufficiently investigated in the conventional studies, and tried to establish the measurement technology to characterize them.
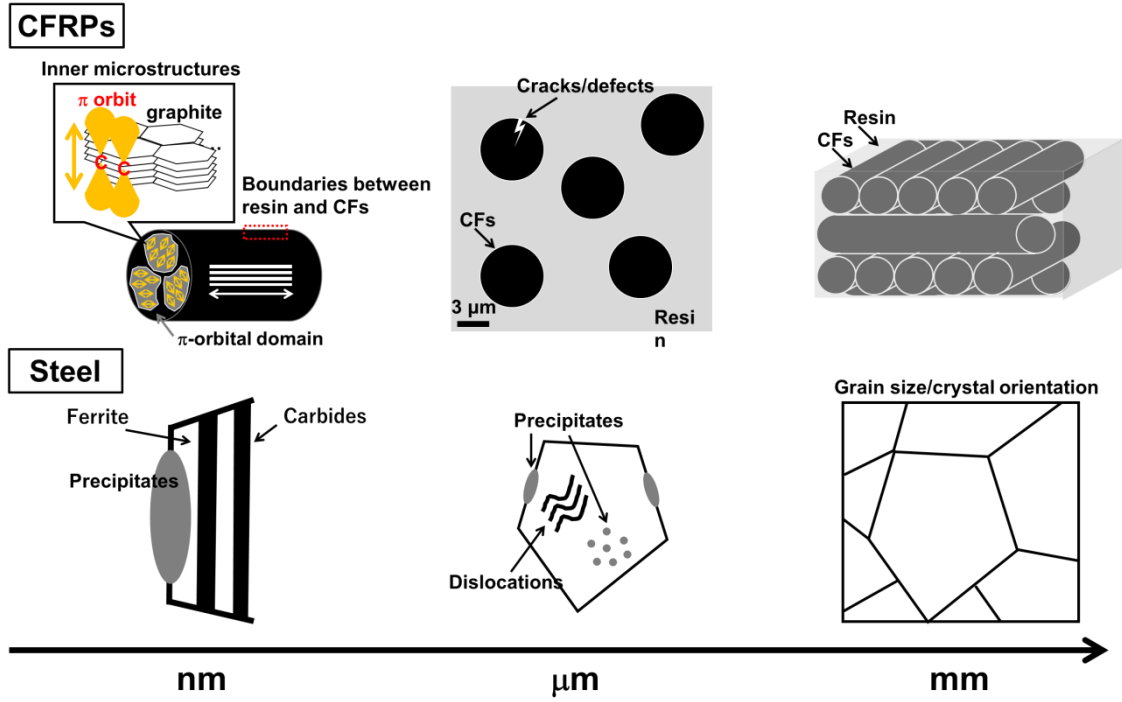
Figure 1.1 Spatial scale of structural materials (CFRPs and steel) focused on in this study.

The mechanical properties (electronic, mechanical, and optical properties) of carbon-matrix and carbon-containing materials are determined by their multiscale structures, i.e., the atomic arrangement of carbon atoms (layer, crystal, and random structures), the chemical structures (the types of chemical bonds, molecular orbital orientation, and electronic states), and the structural heterogeneity (spatial distribution and regularity/irregularity) (Xu *et al.*, 2017; Tanaka *et al.*, 2011) (Fig. 1.2). For example, CF is a typical structural material that features a high tensile strength, high tensile modulus, good vibration damping property, etc. The typical raw materials of CFs are polyacrylonitrile (PAN) and tar pitch derived from coal and petroleum (Chand, 2000). CF is an aggregate of graphite crystals having sizes of several nm to several 10 nm. The mechanical properties of CFs are controlled by (1) the crystallinity of the microcrystal graphite in CFs, (2) the size and

spatial distributions of the defects (voids) in the CFs and their surface cracks, and (3) the crystal and π-orbital oriented domains of the microcrystal graphite in CFs, as shown in Fig. 1.2.

Further, only a small amount of carbon is contained (typically a low percentage) in steel, although it contributes significantly to the mechanical properties of steel as an additive element in multiscale microstructures (Fig. 1.3). The essential factors that determine the mechanical properties of steel are (1) the types of crystal phases, size, and spatial distributions of the grains and crystal orientations; (2) the size and spatial distributions of defects, such as the atomic vacancies, dislocations, and voids; (3) the morphology of the additive elements (the interstitial solid solution, substitution solid solution, and compounds) and their spatial distributions (segregation and uniform dispersion); and (4) the chemical structure of iron and the additive elements.
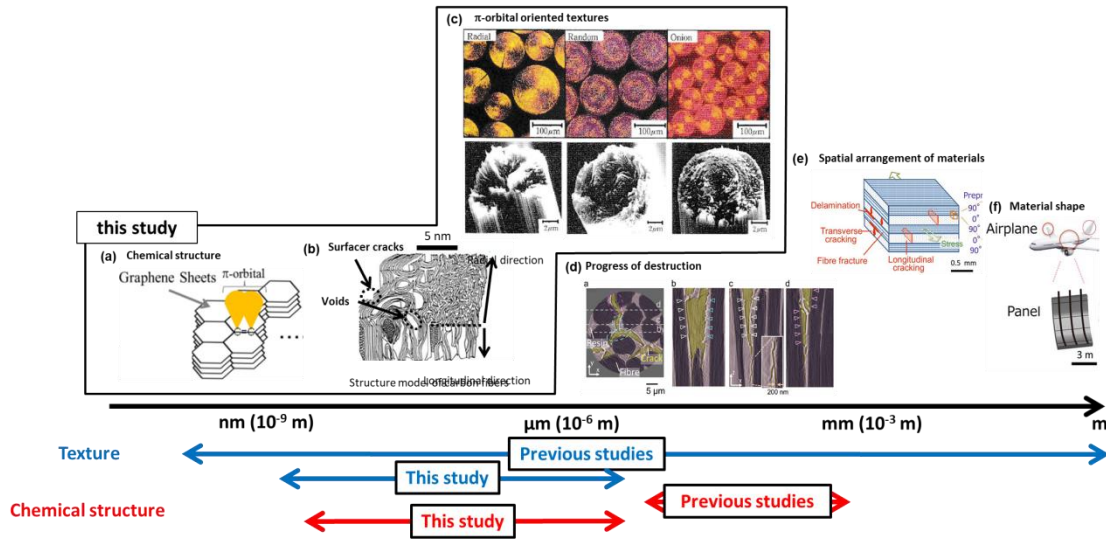
Figure 1.2 Multiscale analysis of carbon fibers (CFs) and carbon fiber-reinforced plastics (CFRPs), and the scope of this study. (a) π-orbital derived from the C=C bonds in the graphite crystals of CFs, (b) microstructures of the graphene sheets in CFs (Matsui *et al.*, 1997), (c) cross-sectional images of CFs obtained by polarization microscopy and scanning electron microscopy (SEM) (Arai, 1993), (d) analysis of the CFRP crack-propagation process in CFs by phase-contrast computed tomography (CT) (Kimura *et al.*, 2019, Watanabe *et al.*, 2020), (e) scheme of the spatial arrangements of the CFs and resin in CFRPs (Kimura *et al.*, 2019), and (f) scheme of an aircraft and its components (Kimura *et al.*, 2019).

Figure 1.3 Multiscale analysis of steel and the scope of this study. (a) atomic arrangement of titan carbide (TiC) in bcc-Fe (ferrite, α), (b) cosegregation of boron and molybdenum by 3D-atom probe tomography (APT) (Takahashi *et al.*, 2018), (c) progress of the generation of dislocation monitored by TEM compression experiments, (d) observation of crys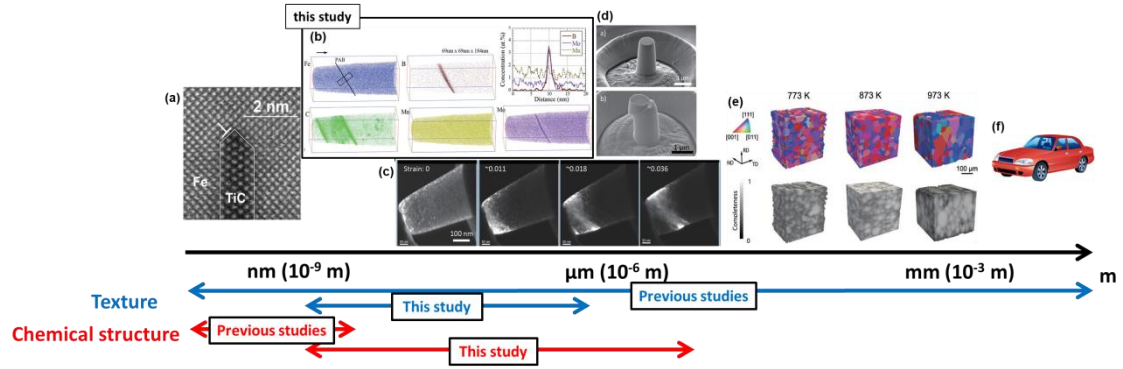tal plane slips by TEM compression experiments (Taniguchi *et al.*, 2018), (e) dependence of the crystal orientation and grain size on heat treatment by in-house X-ray CT (X‑CT) (Sun *et al.*, 2019), and (f) schematic of an automobile.

In steel, carbon exists as an interstitial solid-solution element in bcc-Fe (ferrite, α) and fcc-Fe (austenite, γ), as carbides combined with iron and additive alloy elements (vanadium, titan, niobium, etc.) (particle size: 1–10 μm), and as segregation elements among the grain boundaries.

Various analytical methods have been employed to clarify these multiscale characteristics. Table 1 summarizes the characteristics of the major analytical methods for determining the chemical structures. For example, in CFs, (1) the crystallinity has been investigated by X-ray diffraction (XRD) or electron diffraction (Vazquez-Santos *et al.*; 2012, Matumoto *et al.*, 1985); (2) the defects have been observed by optical/electron microscopy (SEM and TEM) and 3D observation methods employing X-rays (e.g. X-CT, pychography) (Kikuzuki *et al.*, 2020; Wan *et al.*, 2016; Szmyt *et al.*, 2017); (3) regarding the π-orbital orientation domains, the distribution of the *c*-axis orientation of the microcrystal graphite or the π-orbital-derived domains originated from the C=C bonds extending perpendicularly to the graphene sheets in graphite was investigated by electron microscopy (SEM and TEM) or polarization microscopy (Newcomb *et al.*; 2016, Lafdi *et al.*, 1994; Gerald *et al.*, 1991; White *et al.*, 1978).

Table 1.1 Summary of the characteristics of the major analytical methods for the chemical structure

	TEM	PM	EPMA/EDS	EELS	Nano-IR	XPS(PEEM)	XAS(STXM)
Observation object Texture(T) /Chemical structure(C) /Elemental distribution(E)	T	T/C	E	C	C	C	C
Probe	Electron	Visible light	Electron	Electron	Laser	X-ray	X-ray
Detect	Electron	Visible light	X-ray	Electron	Vibration of Cantilever	Electron	X-ray
Spatial Resolution	< 1 nm	1 μm	10-100 nm	< 1 nm	10-100 nm	30-50 nm	30-50 nm
Exited efficiency	low	high	low	low	low	high	high
Beam damage	large	small	large	large	large	large	small
Probing depth	100 nm	～2-3 μm	～2-3 μm	100 nm	～2-3 μm	～2-30 nm	50-100 nm
Excitation process Electron(E) /Laser(L)	E	-	E	E	L	E	E
Orbital orientation	△	×	×	×	×	○	○

When CFRPs were employed in an aircraft with a meter scale, as shown in Fig. 1.2, attention was mainly devoted to designing the shapes of the CFRP parts based on mechanics at the macroscopic scale. However, the mechanical properties are governed by the size and spatial distribution of the defects and features of the boundaries between the resin and CFs on the microscopic scale, ranging from millimeter to micrometer. However, it is challenging to apply these conventional analytical techniques to understand the distribution of the π-orbital orientation in CFs, because the diameter of commercial CFs is approximately 5–10 μm. Moreover, the observation and design of CFRPs at the nanometer scale, with special attention to their chemical states, have not been investigated thus far because of experimental shortcomings. Thus, the design of CFRPs has been pursued on a trial and error or empirical basis at the microscopic scale, and it is important to consider the trigger sites of fracture or degradation.

The investigations of carbon to understand its effect on the mechanical properties of steel regarding its microstructures, crystal structure, and elemental partitioning were mainly performed by electron microscopy (Fig. 1.3). Special attention has been paid to the relationship between the microstructures, mechanical properties, and dislocation movements that govern the mechanical properties of metals (Clemens *et al.*, 2017). The effects of additive elements have been considered in terms of these two aspects, and the elastic and plastic deformations of carbides and the dynamics of the carbon atoms could be considered in classical mechanics, where they are considered as rigid bodies. However, the relationship between the carbon chemical structure and the mechanical properties of steel has not been clearly identified. This is expected to afford a fundamental and in-depth understanding of the interactions among carbon atoms, carbides, dislocations, voids, and grain

boundaries, which is essential for controlling the physical properties of steel. Further, this approach can be applied to profoundly understand the embrittlement mechanism of phosphorus and manganese, which segregate at the grain boundaries.

1.2 Purpose of this study

As mentioned in Section 1.1, carbon plays important roles not only in functional materials but also in structural materials. In this study, to identify the essential role of carbon regarding its chemical structure, the author studied the following two types of materials: (A) CFs and CFRPs, which are typical structural materials in which carbon is the main component, and (B) steel as structural materials in which carbon is employed as an additive element to control the mechanical properties. Although the investigations on the chemical structures of carbon and its spatial distribution have been considered to be essential for the improvement of the mechanical properties of these two structural materials, they have been rarely studied. This is because of the challenge of investigating them through conventional analytical methods. Therefore, employing scanning transmission X-ray microscopy (STXM), described below, the author attempted to establish analytical methods to quantify the heterogeneity of the chemical structure of structural materials at the nanometer scale. The author focused on the relationship between the difference and heterogeneity of the chemical structures and the mechanical properties and aimed to establish analytical methods to identify their relationships. Furthermore, the author also considered that the findings in this study could have industrial benefits, such as guidelines for selecting raw materials, new processes, and insights for developing high-quality materials.

1.2.1 Carbon in CFRPs

To understand the essence of the mechanical properties of structural materials regarding the multiscale analysis and to promote the development of the materials, the author has concluded that the information on the chemical states of carbon was the most important among the aforementioned three factors. When the materials were utilized in products, it was important to consider the shape of the materials, the spatial arrangement of each material, and the form of destruction, as shown in Fig. 1.1 (d)–(f). Additionally, it was also important to understand the type of phase and the chemical structure of the materials, as shown in (c). CF is an aggregate of microcrystal graphite with several tens of nanometers, which varies depending on the raw material. On a large scale, CF could be considered as aggregates of the regions (π-orbital orientated domains) in which the graphite microcrystals are oriented in a specific direction. It is difficult to observe the size, shape, and distribution of the

domains in commercial CFs by polarization microscopy and electron microscopy, which are widely employed. This was because of the limited available methods for investigating their information in commercial CFs with a diameter of approximately 5–10 μm. The orientation distribution was composed of winding features of the graphene sheets in CFs and the defects in the microcrystals and between their boundaries, which were assumed to affect their mechanical properties. Put differently, to consider the mechanical properties of structural materials, not only the average information, but also the phenomena and microstructures that matter at various spatial scales should be analyzed, and the results should be comprehensively applied to evaluating the degree of the effect of each scale on the mechanical properties. Hence, the author focused on analytical methods at the nanoscale, which were suitable for observing the inside of CFs and the boundaries between the different materials.

For the analysis of the orientation distribution in CFs, electron diffractions, polarization microscopy, and other spectroscopic techniques were conventionally performed. However, the electron diffraction could investigate the crystallinity at a high spatial resolution of several nm but it consumes time to measure the diffraction patterns. Electron diffraction might be inappropriate for organic and carbon compounds because the electron beams could damage these materials. Polarizing microscopy could afford an expanded field of view but the quantitativity of its orientation angle is low and the spatial resolution was ~1 μm, making it challenging to observe commercial CFs. Employing electron probe microanalysis (EPMA) and energy-dispersive X-ray spectroscopy (EDS), it was possible to obtain an element distribution on the μm scale. However, it was challenging to observe the internal heterogeneity and boundaries between the different materials because CFs and resins are almost composed of carbon.

The analysis of the chemical states of carbon in CFs required spectroscopic methods. It is possible to investigate the π-orbital oriented domains directly by photoelectron spectroscopy (PES), photoemission electron microscopy (PEEM), and X-ray absorption spectroscopy (XAS) with linearly polarized synchrotron radiation X-rays.

The efficiency of the X-ray excitation was 100 times higher than that of the electron beam excitation. However, it was complicating to analyze the chemical structure in commercial CFs by PES and XAS because PES was too surface-sensitive with a probing depth of a few nm, and the diameter of conventional XAS was 10–1 mm.

1.2.2 Carbon in steel

The relationship between the chemical structures and mechanical properties is important for materials containing carbon as the main component and as an additional element. Conventionally, regarding the microstructure, crystal structure, and element distribution with multiscale, the changes of the polycrystalline microstructures were observed by TEM and X-CT as shown in Figs. 1.2 (a), (e), (f), (h). The spatial distributions of the dislocations and voids, shown in Figs. 1.2 (d) and (g), were investigated by TEM and optical microscopy with serial sectioning, respectively. Additionally, the spatial distributions of the elements, as shown in Figs. 1.2 (b) and (c) were mainly investigated by ATP and TEM–EELS. However, when it was essential to consider carbides, which do not possess a crystal structure that melted during the heat treatment or the chemical bond between Fe and carbon at the grain boundary the investigations of the conventional microstructure and crystal structure were not enough to identify the essential role of carbon in their mechanical properties. Therefore, it was important to analyze the chemical states of carbon in steel (one of the structural materials) on a nanoscale, which was general for functional materials. Regarding the analysis of the chemical structure, the same discussion could be applied to other additive elements in steel.

1.2.3 Outline of each chapter

To achieve the goal, i.e., understanding the role of carbon in CFRP and steel regarding the chemical states of carbon and its heterogeneity on a nm scale, the analyses of its molecular orientation and chemical structure whose spatial resolution was < 1 μm were necessary. Therefore, in the various analytical methods that are summarized in Fig. 1.2, the author selected STXM, which is described as follows: STXM is an analytical method that can obtain the two-dimensional (2D) mapping of XAS by irradiating a thin film sample with synchrotron radiation X-rays focused at approximately 50 nm and scanning the sample in 2D. Although the spatial resolution of STXM is approximately 100 times inferior to that of TEM, the XAS spectra with better signal to noise (S/N) ratio could be acquired since the efficiency of the X-ray excitation is higher than that of electron-beam excitation as described above. The spatial distribution of the molecular orbitals could be investigated utilizing linearly polarized synchrotron radiation X-rays. From the foregoing, the author concluded that STXM could be the suitable analytical method for the investigation of the relationship between the orientation distribution and mechanical properties of carbon materials and the relationship between the chemical structure of carbon and the mechanical properties of steel. The purpose and goal of this thesis and the outline of each chapter are described below.

Chapter 1 (this chapter) summarizes the background and importance of this study.

Chapter 2 describes the experimental methods, namely the principles of XAS and STXM. The details of the experimental method, including the characteristics of the beamline of the synchrotron radiation facility, will be explained. Additionally, the author will explain the analytical methods (XRD and TEM) and the principle of the first-principles calculations that are complementarily employed in STXM.

Chapter 3 describes the study conducted regarding the chemical state of carbon in CFs manufactured from PAN and tar pitch, which are the two typical raw materials of CFs. CF is composed of π-orbital–oriented regions (π-orbital–oriented domains) in which the orientation texture and array of the carbon atoms are aligned. It is assumed that the size and special distribution of the π-orbital–oriented domains could affect the mechanical properties. However, the details of the relationship are still unclear. Therefore, to identify the difference in the texture of the π-orbital–oriented domains, the author focused on clarifying the domain distributions employing STXM measurements with two orthogonal linear polarizations on the two orthogonal sections (cross-section and longitudinal section). Furthermore, complementary measurements, such as the evaluation of the crystallite size of graphite by XRD, were performed. Based on these results, the author examined the relationship between the orientation texture of the π-orbital–oriented domains and the mechanical properties regarding the difference in the raw materials.

In Chapter 4, the author focused on visualizing the spatial distribution and adjacency relationship of the π-orbital–oriented domains in CFs to determine the position of the stress concentration between the domains, which was generated during the shrinking of CFs in the manufacturing process. A 2D map of the π-orbital orientation angles in CF were acquired from the XAS images obtained at various rotation angles.

Chapter 5 describes a new sample rotation holder for STXM, which was developed to improve the accuracy of the parallelism of the rotation axis and sample position, during the azimuthal rotation in the STXM experiments described in Chapter 4. Specifically, the author developed a holder with a cross roller bearing to reduce the deviation between the rotation and optical axes during the azimuthal rotation and the deviation in the sample position due to the azimuthal rotation. Further, the author installed the developed sample rotation holder on the compact STXM instrument at Photon Factory and evaluated its performance. The dependence of OD on the rotational angle was measured to investigate the domain derived from the π-orbitals (the carbon double bonds) in natural spherical graphite.

In Chapter 6, to evaluate the mechanical properties of CFRPs, the author verified the application of STXM in the evaluation of the adhesion between the resin and CFs. The XAS mapping of the C K-edge of the boundary

between the resin and CF was also investigated. When the XAS spectrum of the position of each sample was reproduced from the spectra of the resin, CF, and boundary extracted from the STXM mapping, the difference in whether the boundary-part spectrum was considered or not was evaluated. The chemical structure of the substance in the boundary part was determined.

In Chapter 7, the differences in the chemical structure of carbon were examined regarding its form and structural morphology. In steel, it is well-known that the existence and structural morphology of carbon influences the mechanical properties, and the mechanism is understood as the difference in the dislocation movement. There are few reports on whether the chemical state of carbon changes because of the form or structure of carbon or not, and a clarification is required from the viewpoint of material design. Therefore, the chemical structure mapping of carbon was performed on steel possessing parts with greatly different microstructures (a Fe–C alloy with spherical and lamellar cementite (θ–Fe$_3$C)). The chemical structure of carbon was observed by STXM, and the origin of its difference was determined by the first-principles calculation.

Chapter 8 is a summary of this study and prospects.

References

Arai, Y., *NIPPON STEEL TECHNICAL REPORT*, 1993, **349**, 56-60.

(荒井豊, *新日鉄技報*, 1993, 394, 56-60.)

Chand, S., Review carbon fibers for composites, *Journal of Materials science*, 2000, **35**, 1303.

Clemens, H., Mayer, S., & Scheu, C., Microstructure and properties of engineering materials, *Neutronsand Synchrotron Radiation in Engineering Materials Science: From Fundamentals to Applications: Second Edition*, 2017, 3.

Gerald, J. D. F., Pennock, G. M., Taylor, Domain structure in MP (mesophase pitch)-based fibres, *Carbon*, 1991, **29**, 139.

Heinze, S., Tesoff, J., Martel, R., Derycke, V., Appenzeller, J., Avouris, P., Carbon nanotubes as Schottky Barrier Transistors, *Phys. Rev. Lett.*, 2002, **81**, 4067.

Iijima, S., Helical microtubules of graphitic carbon, *Nature*, 1991, **354**, 56.

Kikuzuki, M., Hayashi, K., Tsunemi, Y., Yabu, S., Matsuno, T., Analysis of microstructures and voids on ductile fracture of ferrite/martensite dual-phase steels through three-dimensional observation, *Tetsu-to-Hagané*, 2020, **106(5)**, 244 (in Japanese).

Kimura, M., Watanabe, T., Takeichi, Y., Niwa, Y., Nanoscopic origin of cracks in carbon fibre-reinforced plastic composites, *Scientific Reports*, 2019, **9**, 19300.

Lafdi, K., Oberlin, A., An attempt to characterize and elaborate anisotropic pitches and derived carbon fibers. Part II: Preparation by separation, *Carbon*, 1994, **32**, 61.

Matsui, J., *Kyoka-prastic* ("Reinforced plastic" in Japanese), 1997, 43, 187. (in Japanese)

(松井醇一, 炭素繊維の話 その1, *強化プラスチックス*, 1997, **43**, 187.)

Matumoto, T., Mesophase pitch and its carbon fibers, *Pure & Appl. Chem.*, 1985, 57, 1553.

Misewich, J. A., Martel, R., Avouris, P., Tsang, J. C., Heinze, S., Tersoff, J, Electrically induced optical emission from a carbon nanotube FET, *Science,* 2003, **300**, 783.

Newcomb, B., A., Processing, structure, and properties of carbon fibers, *Composites: Part A*, 2016, 91, 262.

Novoselov, K. S., Geim, A. K., Morozov, S. V., Jiang, D., Zhang, Y., Dubonos, S. V., Grigorieva, I. V., Firsov. A.,

Electric field effect in atomically thin carbon films, *Science*, 2004, **306**, 666.

Pickering, F., B., Physical metallurgy and the design of steels, *Physical Metallurgy and the Design of Steels*, 1978.

Qui, X., Freitag, M., Perebeinos, V., Avouris, P., Photoconductivity spectra of single-carbon nanotubes: implications on the nature of their excited states, *Nano Lett.*, 2005, **5**, 749.

Soo-Jin, P., *Carbon Fibers*, Springer, 2018.

Sun, J., Holzner, C., Bale, H., Tomita, M., Gueninchault, N., Bachmann, F., Lauridsen, E., Inaguma, T., Kimura, M., 3D crystal orientation mapping of recrystallization in severely cold-rolled pure iron using laboratory diffraction contrast tomography, *ISIJ international*, 2019, **60(3)**, 528.

Szmyt, W., Vogel, S., Diaz, A., Holler, M., Gobrecht, J., Calame, M., Dransfeld, C., Protective effect of ultrathin alumina film against diffusion of iron into carbon fiber during growth of carbon nanotubes for hierarchical composites investigated by ptychographic X-ray computed tomography, *Carbon*, 2017 **115**, 347-362.

Takahashi, J., Kawakami, K., Kobayashi, Y., Haga, J., Ishikawa, K., M., Kubota, N., Progress of atom probe tomography analysis on specific grain boundaries and interfaces in steel, *NIPPON STEEL & SUMITOMO METAL TECHNICAL REPORT,* 2018, **118**, 14-21.

Tanaka, K., Higashihara, H., Shinohara, H., Tanso-gaku ("Carbon science" in Japanese), KAGAKUDOJIN, 2011. (in Japanese)

(田中一義, 東原秀和, 篠原久典, *炭素学: 基礎物性から応用展開まで*, 化学同人, 2011.)

Taniguchi, S., Dehm, G., In-situ electron microscopy mechanical testing for steels, *Nippon steel & Sumitomo metal technical report*, 2018, **118**, 9.

Vazquez-Santos, M. B., Geissler, E., Laszlo, K., Rouzaud, J., Martínez-Alonso, A., Tascon, J. M. D., Comparative XRD, Raman, and TEM study on graphitization of PBO-Derived carbon fibers, *J. Phys. Chem. C* 2012, **116**, 257.

Wan, Y., Straumit, I., Takahashi, J., Lomovb, S. V., Tensile and compressive properties of chopped carbon fiber tapes reinforced thermoplastics with different fiber lengths and molding pressures, *Composites Part A: Applied Science and Manufacturing*, 2016, **91**, 211.

Watanabe, T., Takeichi, Y., Niwa, Y., Hojo, M., Kimura, M, Nanoscale crack initiation and propagation in carbon fiber/epoxy composites using synchrotron: 3D image data, *Composites Science and Technology*, 2020, **197**, 108244.

White, J. L., Zimmer, J. E., Disclination structures in the carbonaceous mesophase, *Carbon*, 1978, **16**, 469.

Wu, Z. C., Chen, Z., Du, X., Logan, J. M., Sippel, J., Nikolou, M., Kamaras, K., Reynold, J . R., Tanner, D. B., Hebard, A. F., Rinzler, A. G., Transparent, conductive carbon nanotube films, *Science*, 2004, **305**, 1273.

Xu, R., Xu, Y., *Modern Inorganic Synthetic Chemistry 2nd Edition*, ScienceDirect, 2017.

Chapter 2

Analytical Approaches for Investigation of Carbon Chemical Structure

2.1 Principles of X-ray absorption spectroscopy

2.1.1 Principles of X-ray absorption near edge structure

The measurement of X-ray absorption by excitation of a core-level electron into unoccupied state as a function of photon energy of X-ray is called X-ray absorption spectroscopy (XAS) or X-ray absorption near edge spectroscopy (XANES). The X-ray absorption intensity is given by

$$I(E) = \sum_f |< f|q\boldsymbol{E} \cdot \boldsymbol{r}|i >|^2 \delta(E_i - E_f - E) \quad (2.1)$$

where q is a charge of electron, $\boldsymbol{E}$ is the electric field of the X-ray, and $\boldsymbol{r} = (x, y, z)$ is the position operator of the electron. E, E_i, E_f are energies of X-ray, initial and final state of wave function of electron, respectively, and $|i>$, $|f>$ are the wave function of electron in initial state, and final state, respectively (Stöhr, 1992). C $1s$ XAS spectra represent the unoccupied C $2p$ partial local density of state (DOS). When other orbitals are hybridized with the C $2p$ orbitals, C $1s$ XAS can be used to investigate the unoccupied local DOS.

In this thesis, the author used two measurement modes for XAS, the transmission mode and the conversion electron yield (CEY) mode. Transmission mode experiments are standard for hard X-rays, while they are also available for soft X-rays in case of thin film sample. An alternative to the transmission mode has been provided by measuring the decay products of the core hole which are created in the absorption processes. The decay of the core hole gives rise to an avalanche of electrons, photons, and ions escaping from the surface of the sample. This is the yield mode experiment and is standard for soft X-rays.

The signal detected by the transmission mode includes information on the liner absorption coefficient and the thickness (X-ray transmission direction) of the sample. Assuming that the X-ray absorption intensities before and after transmission is $I_0(E)$ and the $I(E)$, respectively, the relationship between them is expressed as Eq. (2.2), where $\mu(E)$ is the liner absorption coefficient and t is the sample thickness (Stöhr, 1992). As shown in Eq. (2.3), the energy dependence of optical density (OD) was obtained, which is the product of the linear absorption coefficient and sample thickness. Note that $I_0(E)$ is the X-ray absorption intensity when X-ray directly entering the detector without passing through the sample during measurement.

$$I(E) = I_0(E)e^{-\mu(E)t} \qquad (2.2)$$

$$OD \equiv \mu(E)t = \ln\frac{I_0(E)}{I(E)} \qquad (2.3)$$

The principle of the CEY mode is based on the fact that the X-ray absorption intensity is proportional to the number of Auger electrons, secondary electrons, and photoelectrons. When X-rays irradiated on the sample, Auger electrons generated from the sample surface and secondary electrons that collide with helium atoms as shown as Eq. (2.4) in the chamber were detected as sample current.

$$e^- + He \longrightarrow He^+ + 2e^- \qquad (2.4)$$
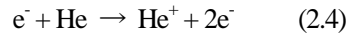
In addition to the transmission method and CEY method, the fluorescence yield (FY) method measures characteristic X-rays absorption intensities generated from the sample. In general, there is a tradeoff between the fluorescence intensities and the number of Auger electrons. Light elements discharge more Auger electrons, and the heavy elements effuse more fluorescence from a few hundred nanometers from the surface of a sample (Nielsen *et al.*, 2001). Therefore, the CEY method is more advantageous than the FY method for carbon as shown in Fig. 2.1 (Briggs *et al.*, 1990). The mean free path of 260 eV Auger electrons from C is of the order of 10 Å. Since the mean free path of the incident X-ray is of the order of 1000 Å, the CEY method is a
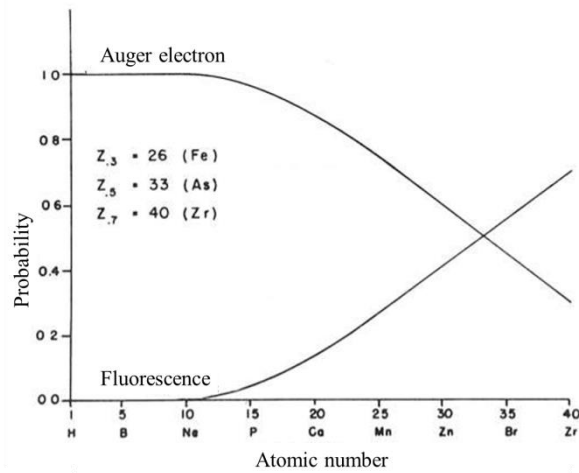

Figure 2.1 Atomic number dependence of Auger electron emission and fluorescent X-ray emission probabilities.

measurement of only 10 Å from the surface of a material, and hence rather surface sensitive. The signal intensity of CEY is proportional to the ratio of the intensity of X-ray I_0 (E) before irradiation and the detected current i (E) after passing through the sample, and is expressed as Eq. (2.5).

$$CEY\ int. \equiv \frac{i(E)}{I_0(E)} \qquad (2.5)$$

The one of purposes in the study in Chapter 7 is to investigate the difference in the chemical structure of carbon depending on the morphology (grain and lamellar) of the sample and compare the difference of chemical structure between the surface and the bulk using transmission and CEY methods.

2.1.2 Principles of scanning transmission X-ray microscopy

The principle of scanning transmission X-ray microscopy (STXM) is explained below. Figure 2.2 is a schematic illustration of STXM. First, synchrotron radiation X-rays are condensed with a Fresnel zone plate (FZP) (Hitchcock, 2012). A FZP is a device with concentrically fabricated multiple grooves. The intervals between the grooves become narrower as it gets closer to the periphery. The zero-order and high-order diffracted light beams passed through the FZP are removed by an order sorting aperture (OSA) and only the first-order diffracted light beams are gathered. The final diameter of the gathered beams is roughly the width of the groove at the most outer side of the FZP. Synchrotron radiation X-rays concentrated to approximately 50 nm were used in these experiments.

In addition, two-dimensional X-ray absorption images of a specific element near the absorption edge are measured (image stacking measurement) and combined to obtain its XANES images. Furthermore, using linearly polarized synchrotron radiation X-rays makes it possible to obtain two-dimensional images of molecular orbital orientation in the spatial resolution of approximately 50 nm. Using circularly polarized synchrotron radiation X-rays makes it possible to obtain two-dimensional images of magnetic states such as spin magnetic moment and orbital magnetic moment (Ueno *et al.*, 2017).
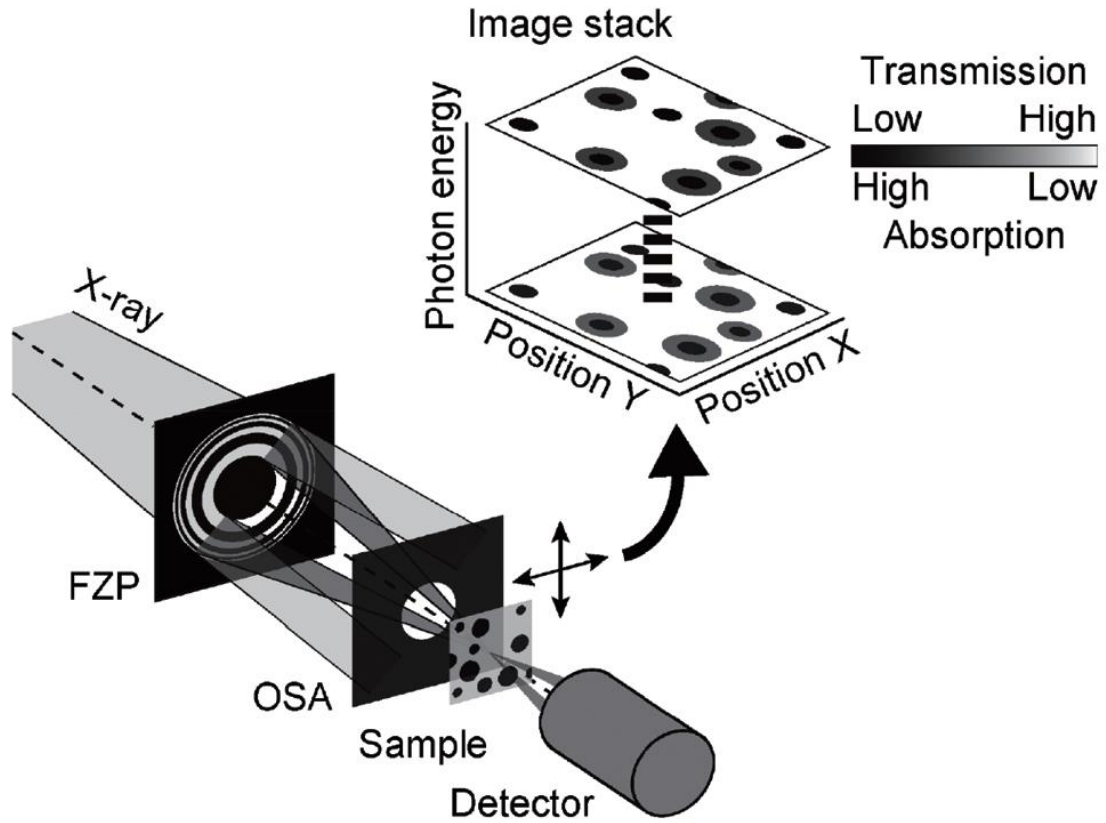
Figure 2.2 Schematic illustration of STXM (Takeichi, 2016).

2.2 Experimental setup

2.2 Experimental setup

2.2.1 Photon Factory

2.2.1.1 Instrument of scanning transmission X-ray microscopy

Figure 2.3 shows a schematic figure of the optical system of compact STXM (cSTXM) at Photon Factory (Takeichi *et al.*, 2016). The X-ray beam was focused at approximately 50 nm by the FZP. This STXM instrument enabled us to obtain the X-ray absorption spectra by the transmission and CEY methods simultaneously. In the experiment, the inside of the measurement chamber had helium gas atmosphere of 0.1 atm to keep thermal conductivity well in the chamber. In the transmission method, the X-ray absorption ratios before and after the transmission of a thin sample were measured with a photomultiplier tube. The signal detected by the transmission method includes information on the liner absorption coefficient and the thickness (X-ray transmission direction) of the sample.
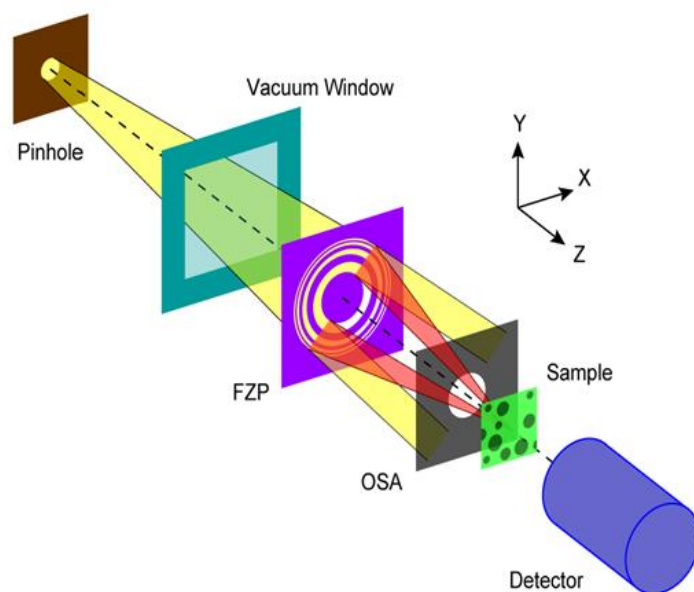
Figure 2.3 Schematic figure of scanning transmission X-ray microscopy (Takeichi, 2016).
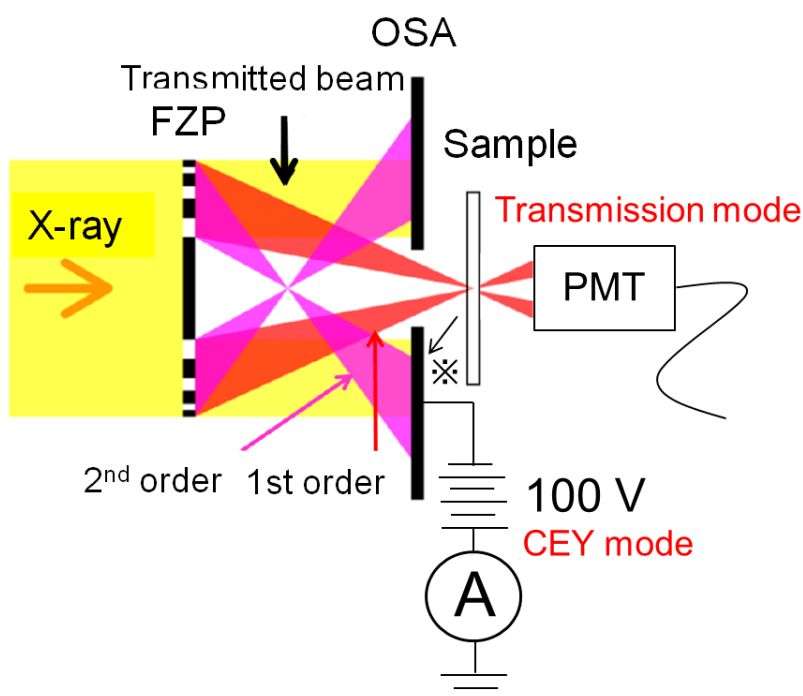

Figure 2.4 Schematic diagrams of transmission method and CEY method in cSTXM.

The data is compatible with the analysis software aXis2000 (A. P. Hitchcock, aXis2000 analysis package is written in an Interactive Data Language (IDL), http://unicorn.mcmaster.ca/aXis2000.html) and Mantis (http://spectromicroscopy.com).

Sample current from the OSA installed upstream of the sample in order to pass only the first-order diffracted light by the FZP. The collision process of Auger electrons, secondary electrons, and photoelectrons and helium atoms as marked as * in Fig. 2.4 is a reaction expressed as Eq. (2.4). The applied voltage in this study was 100 V.

2.2.1.2 Beamline 13 (BL-13)

The beamline BL-13A at KEK-PF is designed for soft X-ray spectroscopy including XAS, photoemission spectroscopy (PES), and angle-resolved photoelectron spectroscopy (ARPES). It is equipped with an APPLE-II type undulator and a varied space plane grating monochromator, which covers the photon energy range of 100-2000 eV and provides soft X-rays with horizontal and vertical linear polarizations. The photon flux is 1×10^8-10^{12} photons/sec at the energy resolution of $E/\Delta E = 7700@244.3$ eV and $7100@401.0$ eV, respectively. A schematic layout of the beamline optics is shown in Fig. 2.5. The undulator radiation is focused by the front collector mirror M1 to the exit slit (S) in the vertical direction and 22.4 m from the light source point in the horizontal direction. It is wavelength-dispersed by a spectroscope consisting of a plane mirror M2 and a plane diffraction grating VLSG (300, 1000 lines/mm are available), and is monochromaticized by an output slit S. The spectroscopic light that has passed through S is focused on the sample position by the post-focusing mirror M3. M3 consists of two switchable toroidal mirrors with different curvature radius, which can focus at the first focus position (F1) and the second focus position (F2), respectively.
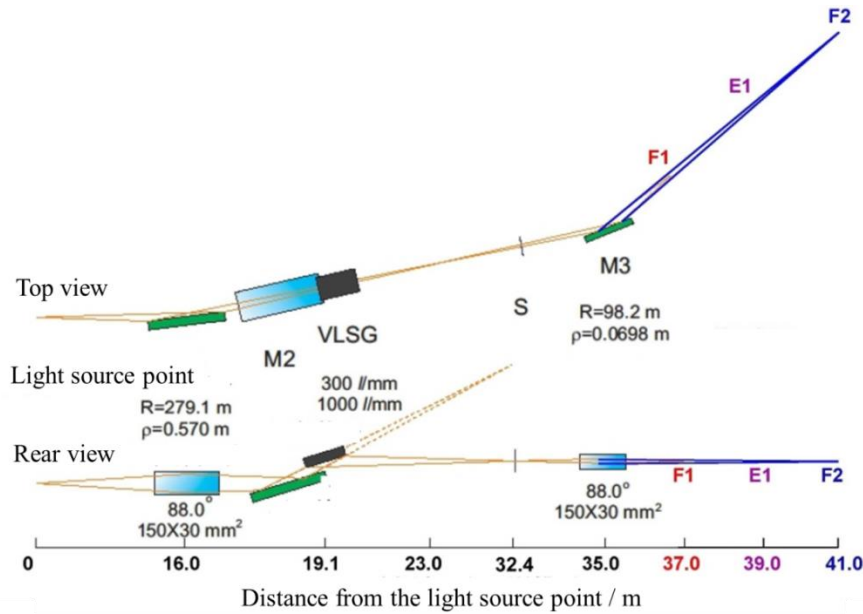

Figure 2.5 Schematic layout of the beamline optics of BL-13A.

2.2.1.3 Beamline 19 (BL-19)

The beamline BL-19 at KEK-PF is designed for soft x-ray spectroscopy including XAS and X-ray magnetic circular dichroism (XMCD). BL-19A is a branch dedicated for STXM and BL-19B has an instrument for bulk XAS measurement by transmission mode, total-electron yield and fluorescence yield and free port for any experiments using soft X-ray. It is equipped with a twin APPLE-II type undulator, which covers the photon energy range of 90-1900 eV and provides soft X-rays with linear, circular, and elliptical polarizations. The photon flux is ~ 1×10^{10}-10^{12} photons/sec with the energy resolution of $E/\Delta E = 4500@244.3$ eV and $4300@401.0$ eV. 160-1900 eV is available in BL-19A. A schematic layout of the beamline optics is shown in Fig. 2.6. The light which has gone through Q slit is vertically converged by the cylindrical mirror M1 and then is irradiated on the monochrometer which consists of a plane mirror M2 and a variable line spacing plane grating monochromator (VLS-PGM). The VLS-PGM is a diffraction grating which has different line spacing depending on the position in order to achieve high resolution in a wide photon-energy range. The monochromated light passes through the exit slit A or B. The cylindrical mirror M3A or M3B is used to direct the beam into one of the two beamline branches (BL-19A or B). The FZP is installed 2 m farther from the exit slit than the BL-13. This makes the focused diameter smaller and the spatial resolution relatively improved.
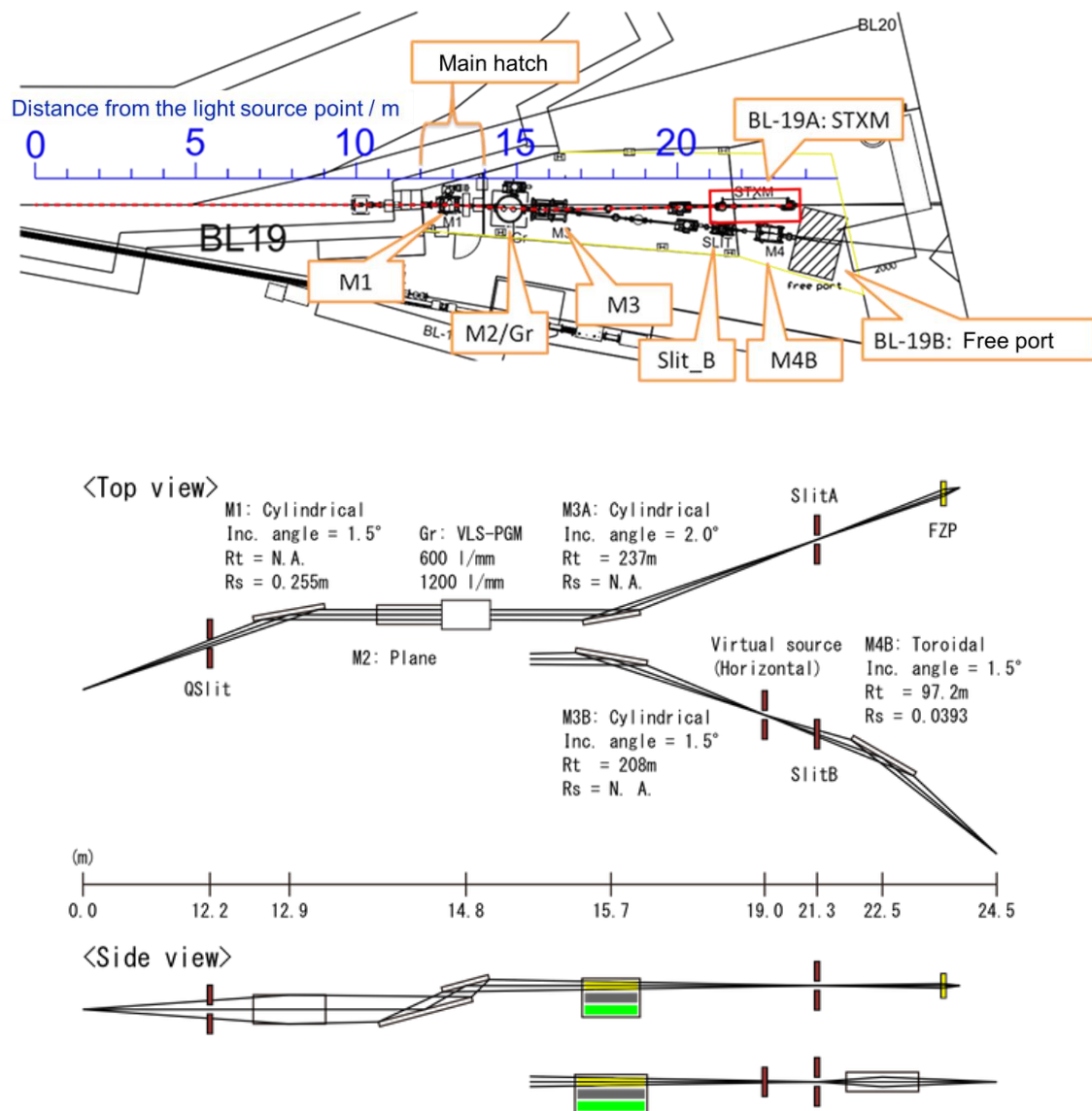
Figure 2.6 Schematic layout of the beamline optics of BL-19.

2.2.2 UVSOR

2.2.2.1 Instrument of scanning transmission X-ray microscopy

The STXM measurements were performed at BL4U, UVSOR Synchrotron in Institute for Molecular Science (Okazaki, Japan) (Ohigashi *et al.*, 2013). Figure 2.7 (a) shows the optical system of the STXM. The incoming monochromatic X-ray is focused on a sample by a FZP through an order select aperture. The X-rays are detected by a photomultiplier tube with a scintillator. By performing 2-dimensional scan of a sample, an X-ray transmission image is acquired.

Two-dimensional map of X-ray absorption spectra can be measured by acquiring the X-ray absorption images with changing the energy of the incoming X-rays continuously. Then, detailed analysis of near edge X-ray absorption fine structure (NEXAFS) brings information of chemical structure of a specific element.

Figure 2.7 (b) shows the azimuthal-rotation sample holder (Hernández-Cruz *et al.*, 2007) used in this measurement. Details regarding the cell have been described previously (Ohigashi *et al.*, 2016). The rotation angle can be rotated clockwise or counterclockwise in 6° increments. The sample is measured in the STXM chamber filled with 0.01 atm of helium gas.
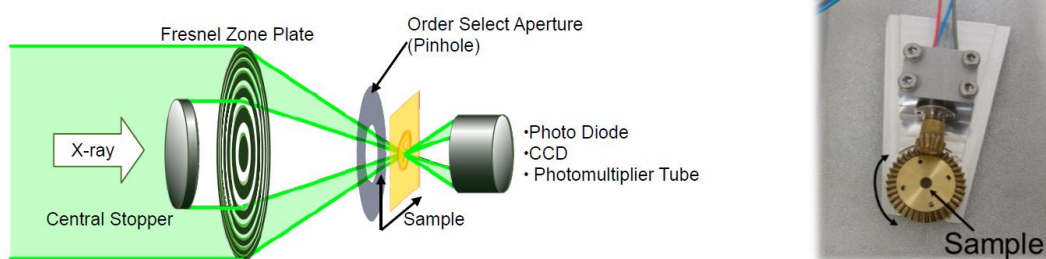
Figure 2.7 (a) Schematic figure of STXM optics and (b) a photo of the azimuthal-rotation sample holder (Ohigashi *et al.*, 2016).

2.2.2.2 Beamline 4U (BL4U)

This beamline equips an in-vacuum undulator, a varied-line-spacing plane grating monochromator and a fixed exit slit. A variable inclined angle monochromator. This combination produces a monochromatic X-ray with horizontal polarization. This beamline covers the photon energy range of 150-770 eV and provides soft X-rays with linear polarizations. The photon flux is 2.4×10^7 photons/sec at the energy resolution of $E/\Delta E = 3000@285.0$ eV. The aperture size of the fixed exit slit determines not only the resolving power but also the size of a microprobe. A Fresnel zone plate is used as a focusing optical device through an order select aperture and its focal spot size of approximately 30-50 nm is available at minimum. An image is acquired by detecting intensities of the transmitted X-rays by a photomultiplier tube with scintillator with scanning a sample two-dimensionally. By changing the energy of the incident beam, each two-dimensional XAS image is stacked. A main chamber of STXM is separated from the beamline optics by a silicon nitride membrane of 100-nm thickness; therefore, sample folders can be handled in vacuum or in helium at 0.01 atm.
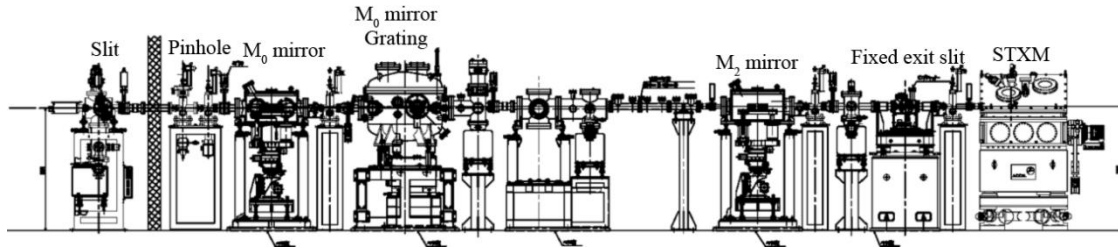
Figure 2.8 Schematic image of BL4U. (Ohigashi, 2021)

2.3 Other Characterization methods

2.3.1 X-ray diffraction

X-ray diffraction (XRD) decides the crystal structure of materials using the diffraction pattern (Waseda *et al.*, 2011). Using X-ray source, it goes inside the crystal, and as a result bulk crystal structures evaluated. The diffraction pattern is governed by the Bragg equation,

$$2d\sin\theta = n\lambda \qquad (2.6)$$

where d is the length of the period, θ is the incident angle of the X-ray, and λ is the wave length of the X-ray.

In Chapters 3 and 4, the author calculated the crystalline sizes of graphite in CFs. The author used Halder-Wagner method (Halder *et al.*, 1966) for the calculations. Halder-Wagner method assumes the physical peak broadening as pseudo-Voigt function and considering that, average size and strain can be estimated from the XRD peak broadening.

2.3.2 Electron diffraction

Electron microscopies (e.g. transmission electron microscopy (TEM) and scanning electron microscopy (SEM)) are usually supplied with equipment to obtain diffraction patterns and micrographs from the same area of a sample (Carter *et al.*, 2016). Electron diffraction patterns are conducted to obtain quantitative information on phase identification, orientation relationship and crystal defects in materials.

In Chapter 4, the author investigated the orientation of c axis of graphite in CFs to compare with the π-orbital orientation determined by STXM. In Chapter 7, the author determine the crystal orientation of θ-Fe$_3$C at some sample positions in bulky θ-Fe$_3$C and lamellar θ-Fe$_3$C to calculate C K-edge XAS spectra considering the anisotropy of crystal orientation.

2.4 The first-principle calculation

The first-principle calculations are based on quantum mechanics and only use the fundamental constants of physics as input to provide detailed insight into the origin of electronic, mechanical properties of materials (Martin, 2004). Both of structural and spectroscopic information is directly obtainable from high-performance computations. Accurate results on thermodynamic stability, atomic positions and lattice parameters in terms of energetics are obtained from calculations within the density functional theory (DFT) formalism. In Chapter 7, the author calculated C K-edge spectra of θ-Fe$_3$C using the Vienna Ab initio Simulation Package (VASP) and the full-potential multiple scattering theory (FPMST).

VASP is an ab initio quantum molecular dynamics (MD) calculation program using pseudopotentials and plane wave bases. VASP calculations were performed assuming periodic boundary conditions for crystals and inorganic solids. The VASP calculation is based on the finite temperature local density approximation (LDA) using free energy as a variation, and uses the effective matrix diagonalization method and Pulay mixing to determine the electronic ground state for each MD step. It is applied to various problems such as band calculation, optimization of stable structure and transition state structure.

The FPMST is the generalization of the multiple scattering theories to overcome the muffin-tin approximation for the shape of the potential. It is widely used due to the strong simplification brought about in the numerical solution of the Schrodinger equation. This approach is based on an alternative derivation of the full potential multiple scattering equations. FPMST is a program for X-ray absorption spectroscopies.

2.5 Sample preparation

2.5.1 Focused ion beam (FIB) processing

The FIB processing is one of the most popular methods for preparing thin film samples for STXM measurements. In FIB processing, the field of view (FOV) of processing can be determined while considering the sample morphology by SEM, and it is easy to pick up sample position desired. On the other hand, the sizes of the thin film samples are limited by the thickness. For example, when the film thickness is approximately 100 nm, the maximum size is approximately 20 μm^2, and the maximum FOV that can be observed as a continuum is narrower than that fabricated by ultramicrotome described in Section 2.5.2. Furthermore, it is necessary to consider the effect of damage caused by ion irradiation during sample processing.

CFRP thin film samples reported in Chapter 6 were prepared as follows; first, the sample was embedded with

resin, and the surface of the sample was smoothed by cross section polisher (CP) processing shown in Fig. 2.9 (a). Then, after determining the region to pick up, the sample was cut out and picked up by FIB shown in Fig. 2.9 (b). After cutting out, a plate-shaped sample (15 μm × 15 μm × 200-300 nm), the thickness were further adjusted by FIB to obtain the desired thickness. In FIB processing, damages caused by FIB irradiation often remain on the surface of the thin film sample. Then, argon milling was used to remove surface damages and adjust the specimens to the desired film thickness (about 100 nm for the sample in Figure 2.9 (c)). Figure 2.9 (c) shows the SEM image of the finished thin film sample. Table 2.1 shows the conditions for FIB processing in this processing.
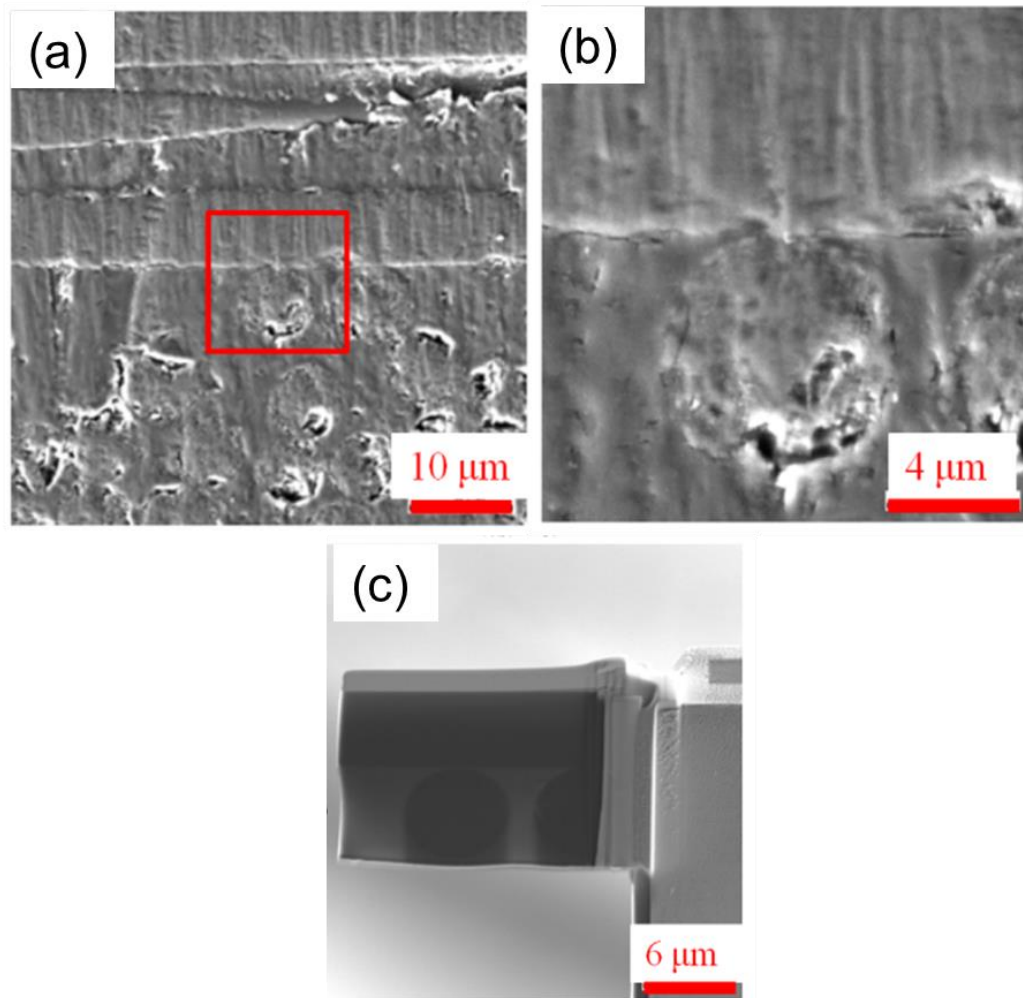
Figure 2.9 Specimen processing procedure (a) the region to be measured with STXM, (b) a picked-up sample and (c) slicing processing by FIB

In FIB processing, the sample temperature rises due to beam irradiation, and the sample may be deformed or deteriorated. The changes on the sample surface of coal that can be softened and deformed at approximately 350 ° C was investigated. Figure 2.10 shows the backscattered electron (BSE) images before and after FIB irradiation on the surface of the sample (Inside the red circle in Fig 2. 10). FIB instruments with a cryogenic system can process at -100 ℃ to room temperature. However, it is advisable to consider processing using ultramicrotome described in the next section for samples that are concerned about thermal effects because it is not possible to monitor the temperature during FIB processing. In this study, FIB processing was used for all samples. This is because Fe-C alloy and carbon fibers have almost no damage from FIB.
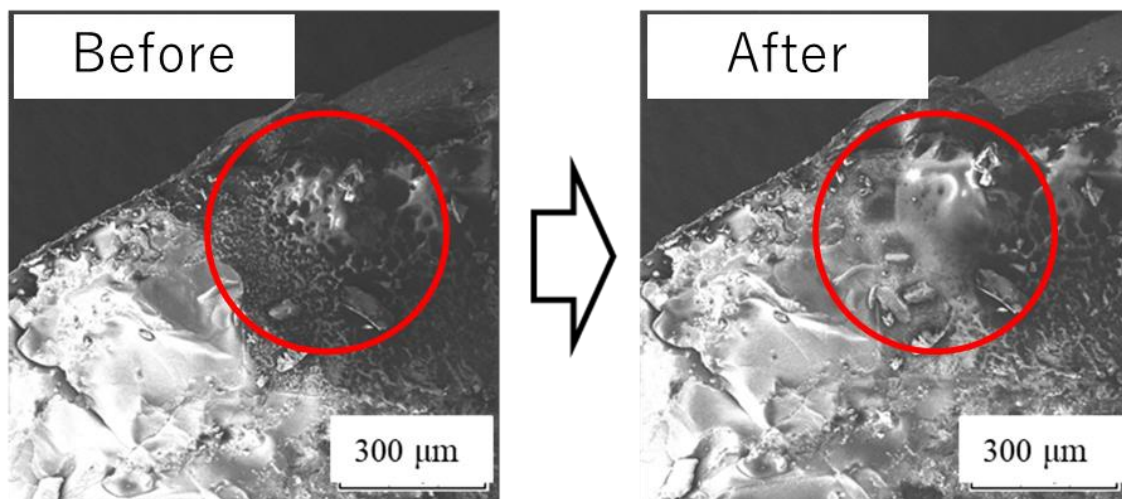
Figure 2.10 BSE images of the surface of coal before and after FIB irradiation

Table 2.1 Example of FIB processing conditions

The name of instrument	Gentle Mill IV5
Oscillation	±30°
Position	10°
Anode Voltage	1kV
Sample Current	29〜31 μA
Bottom Front	8 min
Bottom Back	8 min

2.5.2 Ultramicrotome

Ultramicrotome (UMT) is a method to obtain sample sections and can adjust thickness of samples by bringing a sample close to a fixed knife at a controlled pitch and cutting the surface of samples. It is difficult to determine the processing position as finely as in the FIB processing because the processing position is basically adjusted with an optical microscope. However, using UMT, sections with an area of more than 100 μm^2 can be collected with a thickness of less than 100 nm with a high efficiency. Therefore, UMT is superior to FIB for samples that require wider-area observation. In addition, UMT can also be used with cryogenic system, but unlike FIB, in principle, there is almost no thermal effect during processing. When processing composite materials consisting of brittle samples such as coal and CFRP composed of samples with different hardness, it is better to use an ultrasonically vibrated knife (for example, ultra-sonic, Nisshin EM Co., Ltd.). In many cases, better quality thin film samples can be obtained. Figure 2.11 shows the TEM image of a thin film sample of coal heat-treated at 300 °C for 2 hours in nitrogen atmosphere at 1 atom processed by (a) normal UMT and (b) UMT with an ultrasonic knife.

Using conventional UMT, it was difficult to prepare thin films of brittle samples with less than 100 nm thicknesses, but using ultrasonic knife, it was possible to adjust the film thickness with less than 50 nm as shown in Fig. 2.12 (b). In addition, Fig. 2.12 shows the TEM images of thin film samples of pitch-based CFs embedded with resin processed using (a) conventional UMT and (b) UMT with an ultrasonic knife. It can be confirmed that the cross section samples were deformed using conventional UMT, whereas the shape of samples were relatively maintained using the ultrasonic knife. However, even when an ultrasonic knife was used, many holes were confirmed inside CFs. It was found that UMT was not suitable for observation inside CFs.
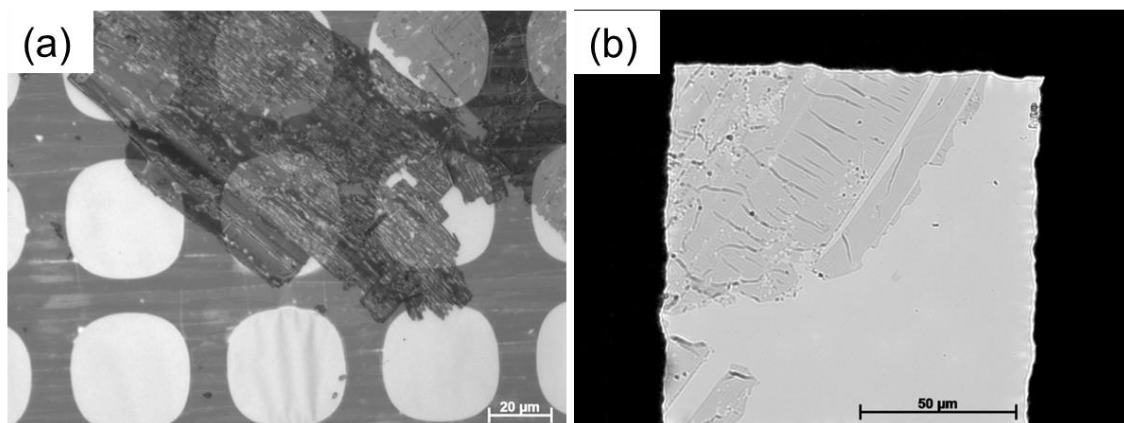
Figure 2.11 TEM images of heat-treated coal processed using (a) conventional UMT and (b) UMT with ultrasonic knife.
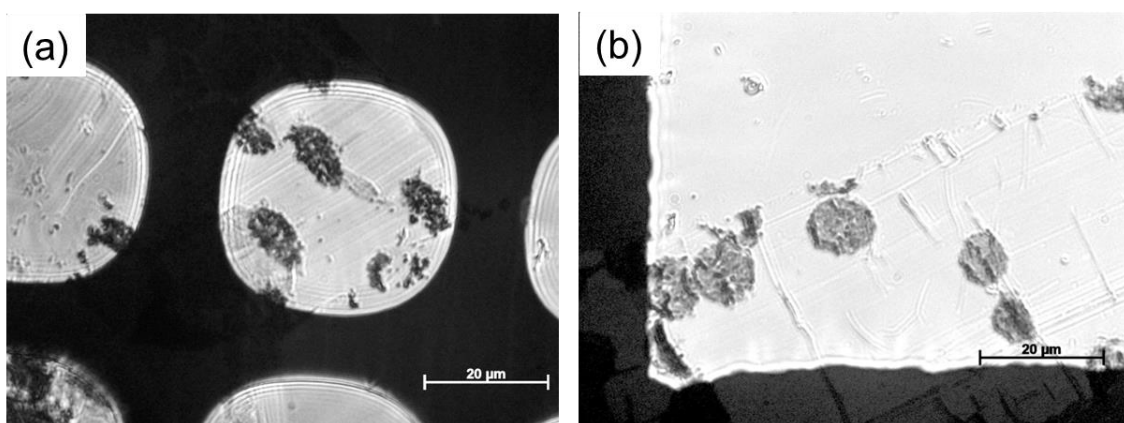

Figure 2.12 TEM images of pitch-based CFs processed using (a) conventional UMT and (b) UMT with ultrasonic knife.

2.5.3 Selection of processing method in this study

Table 2.2 summarizes the features of FIB and UMT described in 2.5.1 and 2.5.2. FIB is superior in terms of spatial accuracy for sampling, but UMT can fabricate approximately 10 times larger thin film samples than using FIB. In case to avoid damages during processing, it is better to choose UMT. In this study, FIB processing was selected because all samples (the CFs (Chapters 3 and 4), natural spheroidal graphite (Chapter 5), CFRP (Chapter 6), and Fe-C alloy (Chapter 7)) had negligible damage caused by FIB processing.

Table 2.2 Comparison of FIB and UMT

	FIB	UMT
Accuracy of positioning the processing field of view	SEM level	Optical microscope level
The size of the thin film samples	$\sim$10 μm^2	$\sim$100 μm^2
Damage due to processing	Need to be considered	Almost negligible
Suitable materials	Carbon fiber, steel, oxide Composite material	Resin, coal, rubber, biological sample

References

Briggs, D., Seah, M. P., *Pratical surface analysis*, 1983.

Carter, C. B., Williams, D. B., *Transmission Electron Microscopy: Diffraction, Imaging, and Spectrometry (English Edition)*, Springer, 2016.

Halder, N.C., Wagner, C.N.J., Separation of particle size and lattice strain in integral breadth measurements, *Acta Crystallogr.*, 1966, **20**, 312.

Hernández-Cruz D., Hitchcock A. P., Tyliszczak T., Rousseau M.-E., Pézolet M., In situ azimuthal rotation device for linear dichroism measurements in scanning transmission x-ray microscopy, *Rev. Sci. Inst.* 2007, **78**, 033703.

Hitchcock, A. P., *Handbook of Nanoscopy*, 2012, 745.

Martin, R. M., *Electronic Structure: Basic Theory and Practical Methods (English Edition)*, 2004.

Nielsen. J. A., McMorrow, D., *Elements of Modern X-ray Physics, 2nd Edition*, 2001.

Ohigashi, T., 2021, https://www.uvsor.ims.ac.jp/beamlines/4U/bl4u.html

Ohigashi, T., Arai, H., Araki, T., Kondo, N., Shigemasa, E., Ito, A., Kosugi, N., Katoh, M., Construction of the scanning transmission X-ray microscope beamline at UVSOR, *J. Phys.: Conf. Ser.*, 2013, **463**, 012006.

Ohigashi, T., Nagasaka, M., Horigome, T., Kosugi, N., Rosendahl, S. M., Hichcock, A. P., Development of in-situ sample cells for scanning transmission x-ray microscopy, *AIP Conf. Ser.*, 2016, **1741**, 050002.

Stöhr, J., *NEXAFS Spectroscopy* 1992.

Takeichi, Y., *Journal of the Japanese Society for Synchrotron Radiation Research*, 2016, **29**, 282-286. (in Japanese)

Takeichi, Y., Inami, N., Suga, H., Miyamoto, C., Ueno, T., Mase, K., Takahashi, Y., Ono, K., Design and performance of a compact scanning transmission X-ray microscope at the Photon Factory, *Rev. Sci. Instrum.,* 2016, **87,** 013704-1.

Ueno, T., Hashimoto, A., Takeichi, Y., Ono, K., Quantitative magnetic-moment mapping of a permanent-magnet material by X-ray magnetic circular dichroism nano-spectroscopy, *AIP Advances*, 2017, **7,** 056804.

Waseda, Y., Matsubara, E., Shinoda, K., *X-Ray Diffraction Crystallography: Introduction, Examples and Solved Problems (English Edition)*, 2011.

Chapter 3

Comparison between the π-orbital Oriented Domains of PAN- and Pitch-based Carbon Fibers

3.1 Introduction

The microstructure of carbon fibers (CFs) plays a dominant role in controlling their physical properties (e.g., tensile strength, tensile modulus) (Miller *et al.*, 1987; Otani *et al.*, 1986; Soo-Jin *et al*., 2018). However, useful information on the nanoscopic structure cannot be obtained via conventional elemental mapping techniques (e.g., electron probe microanalyzer) because CFs are composed entirely of carbon. This has necessitated advanced techniques of illustrating the chemical structure of CFs (e.g., functional groups, orbital orientation of chemical bonds, valences, and magnetic states). The spatial resolutions of the conventional techniques used to analyze chemical structures, such as X-ray photoelectron spectroscopy (XPS) and X-ray absorption near-edge structure (XANES) spectroscopy (Dongxing *et al.*, 2009; Boudou *et al.*, 2006), are ordered from μm to mm. This makes it difficult to obtain detailed information on the inner microstructure of CFs. The spatial resolution of transmission electron microscopy combined with electron energy loss spectroscopy (TEM-EELS) is significantly higher (less than 1 nm) than that of conventional spectroscopic techniques. However, TEM-EELS may not be appropriate for organic and carbon compounds because the strong electron beams may damage these materials (Ponsonnet *et al.*, 1998). In contrast, X-ray beams cause smaller damage than electron beams. X-ray microscopy has advanced over the past few decades owing to improvements in lithographic fabrication techniques, allowing for the use of optical devices such as Fresnel zone plates (FZP), wherein the spatial resolution is approximately 50 nm.

Therefore, this study mapped the carbon chemical structure of CFs by scanning transmission X-ray microscopy (STXM), which has the capacity to explore chemical structure with a spatial resolution at the nanometer scale (Hitchcock, 2012). Owing to its high spatial resolution and relatively less damage to samples, this technique can be particularly useful for the elucidation of the structural details of carbon materials and

various other materials at the nanometer scale, including biomaterials, photonic materials, thermoelectrics, and three-dimensional printed materials (Fernandez *et al.*, 2020; Minxiang *et al.*, 2017; Jood *et al.*, 2011; Minxiang *et al.*, 2019).

In general, CFs can be broadly classified as polyacrylonitrile (PAN)- and pitch-based types. In this study, the author mapped the chemical structure of carbon in the two types of commercial CFs using STXM to evaluate the differences in the distribution of the π-orbital-oriented domains. Moreover, the author used two types of orthogonal linearly polarized X-rays. Herein, the π-orbital-oriented domain and stacked structure of graphene sheets are defined as follows. In general, CFs are composed of microcrystals of graphite. The π-orbital-oriented domains are defined as regions where the π-orbitals in each crystallite of graphite are aligned in the same direction thus failing to satisfy Bragg's law (Rouzaud *et al.*, 1990). In contrast, the stacked structures of graphene sheets are the stacks of graphene sheets in a single crystallite of graphite.

3.2 Experimental

The manufacturer and physical properties of commercial PAN- and pitch-based CFs used in this study are presented in Table 3.1. These CFs were embedded in epoxy resins and sliced into thin films through focused ion-beam processing. The sample thicknesses were adjusted to 100 nm via argon milling. The author fabricated two thin films from the cross and longitudinal sections of the PAN- and pitch-based CFs. STXM measurements were performed using a compact STXM (Takeichi *et al.*, 2016) at BL-13A of the Photon Factory in the High Energy Accelerator Research Organization (KEK). STXM enabled us to obtain XANES mapping at a spatial resolution of approximately 50 nm. The APPLE-II type undulator of BL-13 can generate synchrotron X-rays with both linear horizontal (LH) and linear vertical (LV) polarization modes (Sasaki *et al.*, 1993). An image stack measurement, where a XANES spectrum around the C *K*-edge was obtained for each sample position, was performed using both polarized X-rays (Hitchcock, 2012). Generally, the intensity of the peak in XANES, corresponding to the excitation of the $1s \rightarrow \pi^*$ transitions (due to C = C), is proportional to the square of the inner product between the directions of the orbital and the polarization vector of the X-ray (Stöhr, 1992; Ohigashi *et al.*, 2015; Watts *et al.*, 2011; Watts *et al.*, 2012; Harano *et al.*, 2017). To analyze the distribution of the oriented π-orbitals, the author performed XANES mapping across the entire cross and longitudinal sections using two types of polarized X-rays: LH and LV, respectively. The aXis2000 software was used to analyze the image stacks (a set of X-ray absorption images for a sequence of synchrotron radiation X-ray energies near the C *K*-edge) (Hitchcock, 2019).

X-ray diffraction (XRD) measurements were also performed on pulverized specimens to evaluate the crystallinity of graphite in each CF. Powders of the model samples were packed into an aluminum sample holder (sample part: φ 20 mm × 0.5 mm depth), and XRD measurements were performed using a diffractometer (Smartlab, Rigaku Corporation). The tube current and tube voltage were set at 36 mA and 40 kV, respectively. The radius of the goniometer was 285 mm. A high-speed, one-dimensional detector was used as the X-ray detector, and measurements were performed using the Bragg–Brentano focusing geometry (i.e., the $K\beta$ filter method with Co $K\alpha$ using Fe filters). The measurement conditions were as follows: measurement angle range $2\theta = 15$–$40°$, and step angle width $\Delta 2\theta = 0.02°$. The Halder–Wagner method was used to calculate the crystallite size of graphite (Halder *et al*., 1966).

Table 3.1 The manufacturer and physical properties of commercial polyacrylonitrile (PAN-) and pitch-based carbon fibers (CFs) used in this study.

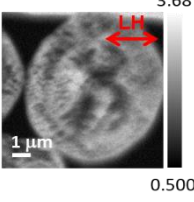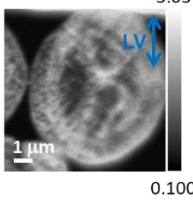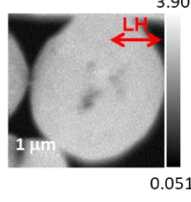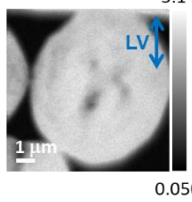|	**PAN-Based CF**	**Pitch-Based CF**
Manufacturer	Toray Industries, Inc.	Nippon Graphite Fiber Corporation
Product name	M46J	YSH50A
Density (g/cm^3)	1.84	2.10
Tensile strength (MPa)	4210	3830
Tensile modulus (GPa)	436	520

3.3 Results and discussion
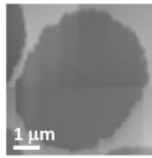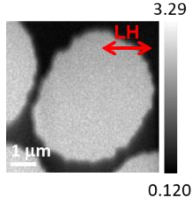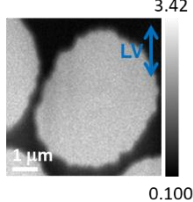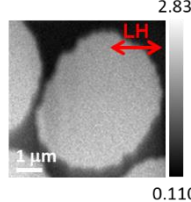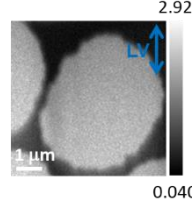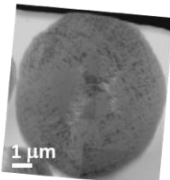
Table 3.2 shows the TEM and X-ray absorption images obtained using STXM at energies of 285.4 eV ($1s{\rightarrow}\pi^*$) and 292.0 eV ($1s{\rightarrow}\sigma^*$) of the cross sections of the PAN- and pitch-based CFs. The red and blue arrows in Table 3.2 indicate the X-ray polarization directions of LH and LV, respectively. Each STXM image consists of 150×150 pixels (1 pixel = 40 nm) and 200×200 pixels (1 pixel = 40 nm) of the PAN- and pitch-based CFs, respectively. With respect to the PAN-based CFs, the contrast (optical density, OD) in X-ray absorption images at 285.4 eV (Table 3.2 (b) and (c)) and 292.0 eV (Table 3.2 (d) and (e)) was independent of the direction of the X-ray polarization.

Here, OD is expressed as

$$\mathrm{OD} \equiv \mu(E)t = \ln \frac{I_0(E)}{I(E)} \qquad (3.1)$$

where μ (E) is the absorption coefficient, t is the sample thickness, and $I_0(E)$ and I (E) are the incoming and transmitted X-ray intensities, respectively. Note that $I_0(E)$ is the intensity of the X-ray that directly enters the detector without passing through the sample during measurement.

Table 3.2 (**a**), (**f**) TEM (bright field) images of the cross sections of the PAN- and pitch-based CFs, respectively; (**b**)–(**e**), (**g**)–(**j**) optical density (OD) images obtained using STXM at energies of 285.4 eV ($1s{\rightarrow}\pi^*$) and 292 eV ($1s{\rightarrow}\sigma^*$) with linear horizontal (LH) and linear vertical (LV) polarized beams. (**f**) is rotated to align with other X-ray absorption images (**g**)–(**j**).
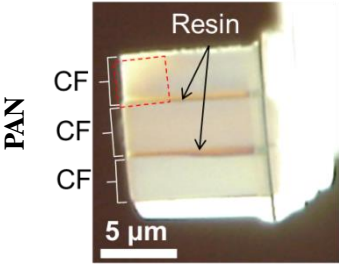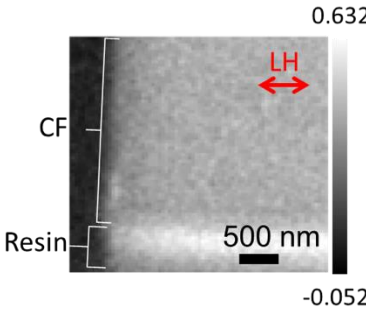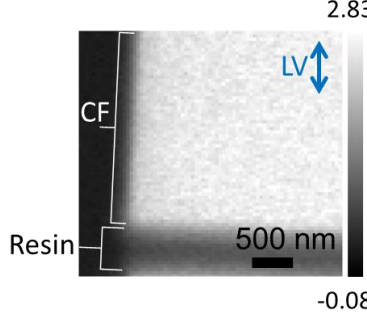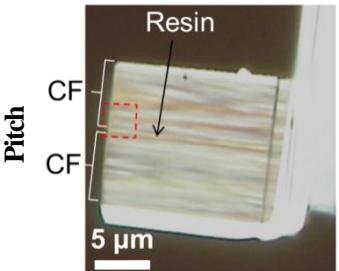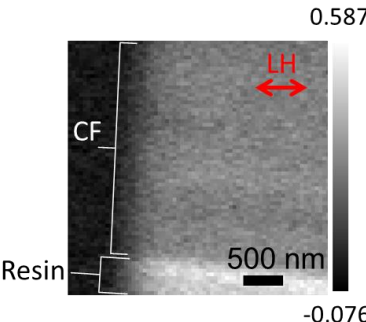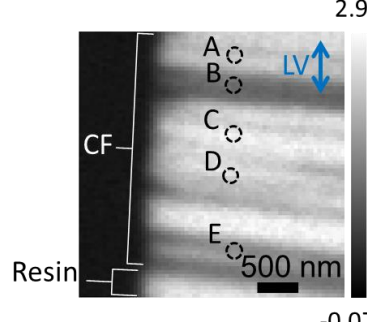
	STXM (OD)			
TEM	$E = 285.4$ eV ($1s{\rightarrow}\pi^*$ (C = C))		$E = 292.0$ eV ($1s{\rightarrow}\sigma^*$ (C-C))	
	LH	**LV**	**LH**	**LV**
(a)	(b)	(c)	(d)	(e)
PAN	3.29 / 0.120	3.42 / 0.100	2.83 / 0.110	2.92 / 0.0400
(f)	(g)	(h)	(i)	(j)
Pitch	3.68 / 0.500	3.03 / 0.100	3.90 / 0.051	3.14 / 0.050

In the PAN-based CFs, the OD images at $E = 285.4$ eV in Table 3.2 (b) and (c) were independent of the direction of X-ray polarization. Similarly, the OD images at $E = 292.0$ eV in Table 3.2 (d) and (e) were independent of the direction of the X-ray polarization. This is because the σ-orbital is not spatially anisotropic, while the π-orbital forms a uniaxial orbit. Therefore, even in X-ray absorption at the C K-edge, the absorption peak intensity derived from the π-orbital is anisotropy not observed in that of the σ-orbital (Stöhr, 1992). In general, OD is proportional to $\cos^2\theta$ when the angle between the vector of the polarized electric field of the X-rays and the direction of the orbit is θ (Stöhr, 1992; Ohigashi *et al*., 2015; Watts *et al*., 2011; Watts *et al*., 2012). These results, depicted in Table 3.2 (b) and (c), are similar to those reported in earlier papers (Watts *et al*., 2012). Thus, the domain sizes within the cross section of the PAN-based CFs are considered smaller than the spatial resolution of STXM (i.e., 50 nm). In contrast, in the pitch-based CFs, the OD images at $E = 285.4$ eV shown in Table 3.2 (g) and (h) were dependent on the polarization direction and showed that the LH and LV polarizations were antonymous. However, the OD images at $E = 292.0$ eV, shown in Table 3.2 (i) and (j), were independent of the direction of the X-ray polarization. Owing to the symmetry of the σ-orbital, there was no

36

polarization dependence. The pitch-based CFs consisted of π-orbital-oriented domains whose estimated sizes ranged from 100 nm to 1 μm, which was greater than the spatial resolution of STXM (i.e., 50 nm). A detailed observation of a single fiber section can be discussed representatively because no significant difference among fibers within the range 1–10 mm^2 is observable via scanning electron microscopy (SEM) or optical microscopy. In addition, the author performed STXM measurements on some types of PAN- and pitch-based CFs in other research studies. With respect to PAN-based CFs, there was no polarization dependence of the OD contrast in the cross sections in at least five fibers of two different types. With respect to the cross section of pitch-based CFs, the polarization dependence of OD contrast as reported herein was observed in at least five fibers for three different types.

Areas in Table 3.3 (a) and (d) present the visible light microscopy images of the longitudinal sections of the PAN- and pitch-based CFs, respectively. The STXM measurements were performed in the areas enclosed by the red dotted lines in Table 3.3 (a) and (d). Each X-ray absorption image measured 73×73 pixels (1 pixel = 41 nm). The author also used polarized X-rays, as indicated by the red and blue arrows in Table 3.3. As shown in Table 3.3 (b) and (c), homogenous OD contrast images were obtained from PAN-based CFs at both X-ray polarizations. In addition, OD was higher under LV (OD = 2.4, in Table 3.3 (c)) than under LH (OD = 0.3, in Table 3.3 (b)), indicating that the orientations of the π-orbitals on the plane radial to the CF axis were nearly perpendicular to the fiber axis. Figure 3.1 shows the averaged C K-edge spectra of the CF areas in Table 3.3 (b) and (c). The spectra were normalized using the OD at 292.0 eV. The difference between the spectra in Figure 3.1 also indicates that the π-orbitals in the PAN-based CFs were oriented perpendicularly to the fiber axis. In addition, the results shown in Table 3.2 (b)–(e) and Table 3.3 (b) and (c) suggest that the graphene sheets in the PAN-based CFs have a fiber texture, and are aligned along the direction of the fiber and randomly oriented within the cross section.

Table 3.3 (**a**), (**d**) Visible light microscopy images of the longitudinal sections of PAN- and pitch-based CFs, respectively, which contain the field of view of STXM (OD) images (red dotted line areas); (**b**)–(**c**), (**e**)–(**f**) the STXM images of PAN- and pitch-based CFs, respectively, are the OD contrast of the X-ray absorption with linear horizontal (LH) and linear vertical (LV) polarized beams.
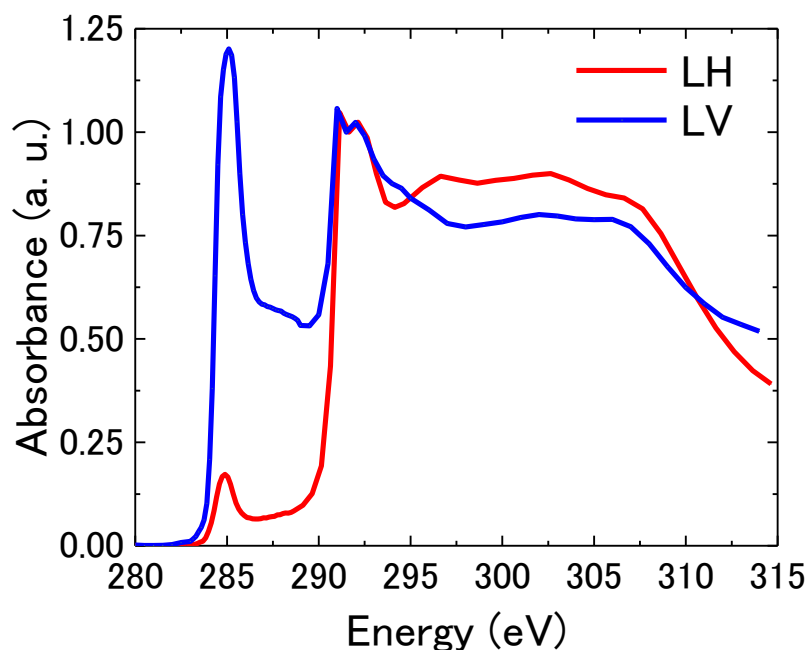
Figure 3.1 Average C *K*-edge spectra of the CF areas in Table 3.3 (b) and (c).

In contrast, for the pitch-based CFs, as shown in Table 3.3 (f), stripe-like contrasts with a width of 200–300 nm were observed in the STXM image with vertical polarization. The OD of the CF ranged from 1.1 to 2.4, but was homogeneous in Table 3.3 (e). This suggests that the domains with widths ranging from 200 to 300 nm were aligned along the direction of the fiber, and the π-orbitals of each domain were randomly oriented in the cross-sectional plane. Figure 3.2 shows the C *K*-edge spectra averaged over areas A to E in Table 3.3 (f). Each spectrum was normalized using the OD at $E = 292.0$ eV. The OD intensity of the peak corresponding to the $1s \rightarrow \pi^*$ excitation differed in each area, indicating that the OD contrast observed in Table 3.3 (f) was attributable to the domains consisting of oriented π-orbitals.
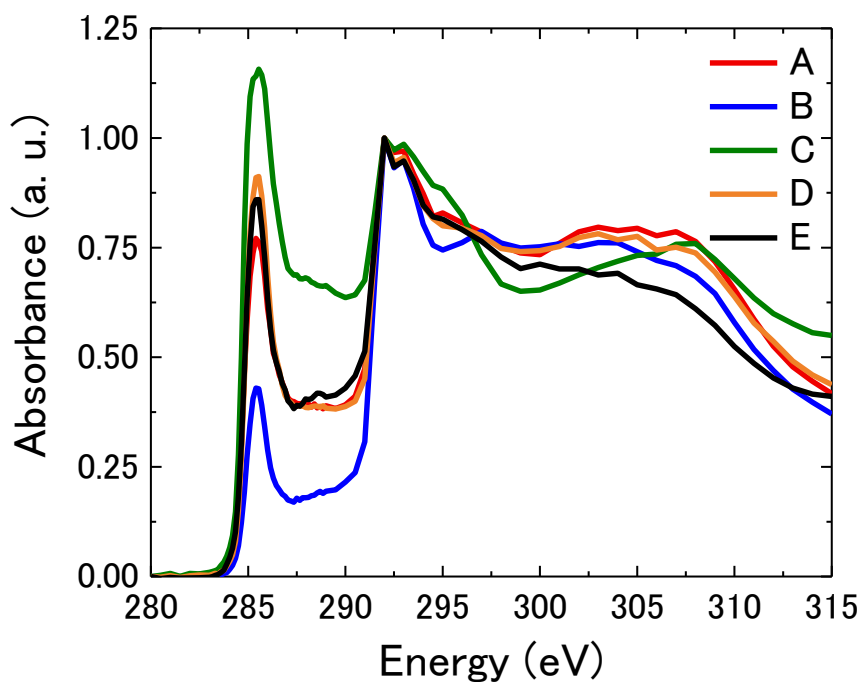
Figure 3.2 Average C *K*-edge spectra of the areas A to E shown in Table 3.3 (f).

Measurement results revealed that the size and distribution of the π-orbital-oriented domains of the PAN- and pitch-based CFs were different, as schematically illustrated in Figure 3.3. The graphene sheets in the PAN-based CFs were parallel to the axis of the fibers that are randomly oriented within the cross section. The size of the π-orbital-oriented domains, if they are present, is less than approximately 50 nm. By contrast, the pitch-based CFs consist of π-orbital-oriented domains whose approximate sizes range from 100 nm–1 μm. The graphene sheets in the pitch-based CFs are also parallel to the axis of the fibers.
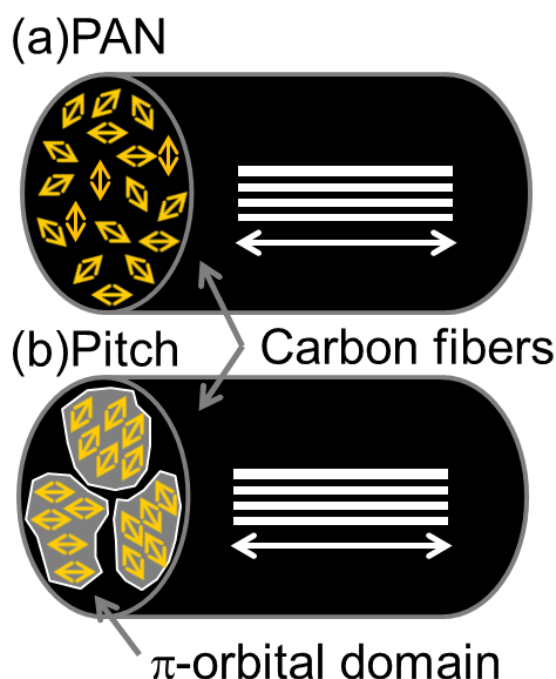
Figure 3.3 Schematic figures of the distribution of the π-orbital-oriented domains and the stacks of graphene sheets in a single (**a**) PAN- and (**b**) pitch-based CF, respectively. The white and yellow two-way arrows represent the directions of the graphene sheets along the fiber and within the fiber cross section, respectively.

Figure 3.4 shows the XRD patterns of the PAN- and pitch-based CFs. The bar in Figure 3.4 denotes the XRD peak position of the (002) plane of the graphite in a previous study (Howe *et al.*, 2003). The satellite peak around 26 ° of XRD pattern of pitch-based CFs is due to $K\beta$ X-ray. The lattice spacing of the (002) plane of graphite (d(002)), and the size of the crystallites were calculated from the position of the peak originating from the diffraction of the (002) planes and the full width at half maximum, respectively (Table 3.4). The d(002) value of the pitch-based CFs is closer to those of graphite (Howe *et al.*, 2003) than that of the PAN-based CFs. This is because the raw material of the pitch-based CFs contains aromatic moieties, while that of the PAN-based CFs is composed of a linear carbon foundation (Soo-Jin, 2018).
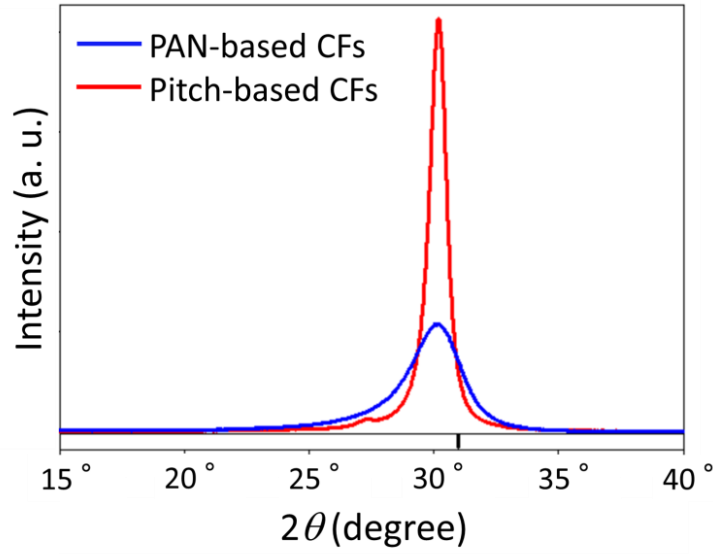
Figure 3.4 XRD patterns of PAN- and pitch-based CFs. The bar denotes the XRD peak position of the (002) plane of the graphite in a previous study (Howe *et al.*, 2003).

Table 3.4 Values of the lattice spacing of the (002) plane of the graphite (d(002)) and crystallite size of PAN- and pitch-based CFs, and graphite from the literature.

	PAN-Based CFs	Pitch-Based CFs	Graphite
The lattice spacing of the (002) plane of the graphite (d(002)) (nm)	0.346	0.344	0.335 (Howe *et al.*, 2003)
Crystallite size (nm)	4.1	12	-

According to the above results, the scale of the stack size of graphene sheets along the c axis of graphite (crystallite size, PAN: 4.06 nm, pitch: 12.3 nm) is considerably different from those of the π-orbital-oriented domains (PAN: < 40 nm, pitch: 100 nm–1 μm). Pitch-based CFs with larger domains are considered to cause relatively greater stress at the domain boundary because contraction in the *c*-axis direction during graphitization results in high tensile modulus. On the other hand, the amount and distribution of defects and voids, which are more likely to generate at such boundaries, are considered to influence the tensile strength of PAN- and pitch based CFs. In addition, the size and distribution of π-orbital-oriented domains could be investigated via STXM. Despite few other techniques of investigating the π-orbital-oriented domains in CFs on a submicron scale, the author recommends STXM for the concurrent elucidation of the crystallite size and the characteristics (size and distribution) of the π-orbital-oriented domains, which are important when considering the mechanical properties

of CFs.

3.4 Conclusion

Using STXM and two orthogonal linearly polarized X-rays, we performed carbon chemical structure mapping of the cross and longitudinal sections of PAN- and pitch-based CFs, both of which exhibited similar elastic modulus. The results showed that the distribution of the π-orbital-oriented domains in the CFs varied considerably, depending on the raw material. In contrast, no difference was observed between the distributions of the σ-orbital orientations of the PAN- and pitch-based CFs. With respect to the PAN-based CFs, the graphene sheet structure was distributed along the direction of the fiber axis, and the cross section consisted of randomly distributed domains measuring below approximately 50 nm, as reported in Chapters 4 and 6. Conversely, the pitch-based CFs were composed of aggregates of graphite domains with π-orbital-oriented domains in the cross sections ranging from ~100 nm to 1 μm. These domains exhibited a striped pattern with a width of 200–300 nm along the CF axis (longitudinal section). The size and distribution of the π-orbital-oriented domains determined by STXM, in addition to the crystallite sizes by XRD, may be the determining factors of the mechanical properties of the CFs. From the difference of domains between PAN- and pitch- based CFs investigated by STXM, the author conjectured that that pitch-based CFs having larger domains contain regions with a larger stress around the domain boundaries due to contraction in the *c*-axis direction during graphitization. Defects and voids are more likely to generate at such boundaries. It was suggested that the amount and distribution of such defects influence the tensile strength of PAN- and pitch based CFs. This information about the π-orbital-oriented domains as well as defects and crystallinity of micro graphite should be essential for mechanical properties of CF.

The use of STXM can provide information on the chemical structure of various molecules. In particular, STXM will be indispensable in the clarification and proposal of design guidelines for additional highly functional materials, when chemical structures, such as π-orbital-oriented domains, are closely related to macroscopic properties.

References

Boudou, J. P., Parent, P., Suarez-Garcia, F., Villar-Rodil, S., Martinez-Alonso, A., Tascon, J.M.D., Nitrogen in aramid-based activated carbon fibers by TPD, XPS and XANES, *Carbon*, 2006, **44**, 2452.

Fernandez, M. P., Black, C., Dawson, J., Gibbs, D., Kanczler, J., Oreffo, R. O. C., Tozzi, G., Exploratory full-field strain analysis of regenerated bone tissue from osteoinductive biomaterials, *Materials,* 2020, 13.

Halder, N. C., Wagner, C. N. J., Separation of particle size and lattice strain in integral breadth measurements, *Acta Crystallogr.*, 1966, **20**, 312.

Hitchcock A.P., aXis 2000 (http://unicorn.mcmaster.ca/aXis2000.html).

Howe, J., Rawn, C. J., Jones, L. E., Ow, H., Improved crystallographic data for graphite, *Powder Diffr.*, 2003, **18**, 150.

Hitchcock A.P., *Handbook of Nanoscopy*, 2012, **2**, 745–791.

Jood, P., Mehta, R.J., Yanliang, Z., Peleckis, G., Xiaolin, W., Siegel, R.W., Al-doped zinc oxide nanocomposites with enhanced thermoelectric properties, *Nano Lett.*, 2011, **11**, 4337.

Miller, B., Muri, P., Rebenfeld, L., A microbond method for determination of the shear strength of a fiber/resin interface, *Compos. Sci. Technol.*, 1987, **28**, 17.

Otani, S., Oya, A., Progress of Pitch-Based Carbon Fiber in Japan, *ACS Symp. Ser.*, 1986, **303**, 323–334.

Minxiang, Z., Shah, S. A., Dali, H., Parviz, D., Yi-Hsien, Y., Xuezhen, W., Green, M. J., Zhengdong, C., Aqueous exfoliation of graphite into graphene assisted by sulfonyl graphene quantum dots for photonic crystal applications, *ACS Appl. Mater. Interfaces*, 2017, **9**, 30797.

Minxiang, Z., Yanliang, Z., Colloidal nanoparticle inks for printing functional devices: emerging trends and future prospects, *J. Mater. Chem. A*, 2019, **7**, 23301.

Ohigashi, T., Nagasaka, M., Horigome, T., Kosugi, N., Rosendahl, S. M., Hitchcock, A.P., Development of in-situ sample cells for scanning transmission X-ray microscopy, I*n Proceedings of the 12th International Conference on Synchrotron Radiation Instrumentation (SRI)*, New York, NY, 6-10 July 2015, 050002-1.

Rouzaud, J.-N., Contribution of transmission electron microscopy to the study of the coal carbonization processes, *Fuel Process. Technol.*, 1990, **24**, 55.

Sasaki, S., Kakuno, K., Takada, T., Shimada, T., Yanagida, K., Miyahara, Y., Design of a new type of planar undulator for generating variably polarized radiation, *Nucl. Instrum. Methods Phys. Res. Sect. A*, 1993, **331**, 763.

Soo-Jin, P., *Carbon Fibers*, 2018, 101–133.

Ponsonnet, L., Donnet, C., Varlot, K., Martin, J. M., Grill, A., Patel, V., EELS analysis of hydrogenated diamond-like carbon films, *Thin Solid Films*, 1998, **319**, 97.

Takeichi, Y., Inami, N., Suga, H., Miyamoto, C., Ueno, T., Mase, K., Takahashi, Y., Ono, K., Design and performance of a compact scanning transmission X-ray microscope at the Photon Factory, *Rev. Sci. Instrum.,* 2016, **87,** 013704-1.

Stöhr, J., *NEXAFS Spectroscopy*, 1992; 169–172, 96-126.

Watts, B., McNeill C.R., Raabe J., Imaging nanostructures in organic semiconductor films with scanning transmission X-ray spectro-microscopy, *Synth. Met.*, 2012, **161**, 2516.

Watts, B., Schuettfor, T., McNeill, C. R., Mapping of domain orientation and molecular order in polycrystalline semiconducting polymer films with soft X-ray microscopy, *Adv. Funct. Mater.*, 2011, **21**, 1122.

Yang, D.,Velamakanni, A., Bozoklu, G., Park, S., Stoller, M., Piner, R. D., Stankovich, S., Jung, I., Field, D. A., Ventrice, C. A., Ruoff, R. S., *Carbon*, 2009, **47**, 145.

Chapter 4

Mapping of π-orbital Oriented Domains in a Pitch-based Carbon Fiber

4.1 Introduction

Pitch-based carbon fibers (CFs) use coal tar pitch or petroleum pitch as raw materials (Otani *et al*., 1966; Otani *et al*., 1972; Matsumoto *et al*., 1985; Soo-Jin *et al*., 2018). Their manufacturing process includes spinning refined pitch, modifying, heat treating, infusibilizing, carbonizing, and graphitizing (Bradley 2016). Pitch-based CFs is characterized by high elasticity and thermal conductivity compared with polyacrylonitrile (PAN) which is a representative CF (Bradley, 2016). Hence, pitch-based CFs are often used in the aerospace industry, sports, etc. To control the mechanical properties (tensile modulus and strength) of pitch-based CFs, it is important to consider the size, shape, and distribution of the π-orbital-oriented domains originating from the C=C bonds of crystalline graphite in structures stacked with graphene sheets in CFs because they are essential factors to determine the mechanical properties of CFs as well as defects on the surface and in the inner microstructure (Yoon *et al*., 1977(Part1); Yoon *et al*., 1977(Part 2); Mochida *et al*., 1966; Naito *et al*., 2012; Naito *et al*., 2008).

In general, the distribution of the π-orbital-oriented domains is observed using polarizing microscopy, Raman spectroscopy, scanning electron microscopy (SEM), and transmission electron microscopy (TEM) (Watanabe *et al*., 2000; Mochida *et al*., 2002; Zheng *et al*., 1999; Wagner *et al*., 2000; Kobayashi *et al*., 2011; Lee *et al*., 2003; Li *et al*., 2011; Gather *et al*., 2007). However, it is difficult to analyze the distribution of the domains of the present commercial products whose diameters are approximately 5-10 μm, using the polarizing microscopy and Raman spectroscopy because their spatial resolution is approximately 1 μm. On the other hand, the spatial resolution of SEM and TEM is high enough to observe the microstructure of CFs. However, it is also difficult to distinguish information on the distribution of defects, surfaces, and microstructures from their image contrast. Electron microscopic techniques might not be appropriate for organic and carbon compounds because the strong electron beams may damage these materials.

This study employed scanning transmission X-ray microscopy (STXM), which can be used to map the chemical structure (e.g., functional groups, orbital orientation of chemical bonds, valences, and magnetic state) with a spatial resolution at the sub-micrometer order (Warwick *et al.*, 1998). STXM can provide information on the π-orbital-oriented domains which is one of the most essential factors for mechanical properties of commercial pitch-based CFs. In this study, the author visualized the distribution of the π-orbital-oriented domains in pitch-based CFs with a spatial resolution of approximately 30 nm. The author measured X-ray absorption images obtained at six rotation angles by STXM measurements and developed the calculation method for the average orientation angle of each sample position in the images using the theoretical relationship between the direction of the orbital and that of the X-ray polarization vector. The author also obtained information on the crystal orientation of some sample positions by electron diffraction. The results were consistent with the results of STXM. This method can provide the orientation relationship among domains in CFs with a spatial resolution of 50 nm, which is better than that of polarizing microscopy, and can enables us to evaluate strain mapping in the CFs using the orientation relationship among domains in CFs.

To characterize two-dimensional continuous π-orbital orientation distributions in CFs, it is necessary to evaluate the orientation image with the specific criteria. By recognizing the pixels as in the same domain when the orientation angle difference between adjacent pixels is below a certain threshold, the domain distributions were visualized based on the criteria at various thresholds. This visualization method suggested that boundaries with large strain were distributed in the outer peripheral portion as compared with the inside of the CF. This method will enable the evaluation of the relationship among domains in the CFs, which might be useful for strain mapping in the CFs. Such knowledge can be one of the important analysis methods for designing the distribution of π-orbital orientation domains to control mechanical properties of CFs.

4.2 Experimental

The pitch-based CF (XN50, Nippon Graphite Fiber Corporation) was used as a sample. Its density, tensile strength and modulus are 2.1 g/cm^3, 3580 MPa, and 500 GPa, respectively. The CF was embedded in epoxy resin and its thin section was fabricated by focused ion beam processing to obtain thin films of the cross-section of CF. The film thickness was adjusted to 80 nm by argon milling.

The STXM measurements were performed at BL4U, UVSOR Synchrotron in Institute for Molecular Science (Okazaki, Japan) (Ohigashi *et al.*, 2013). BL4U is equipped with an in-vacuum undulator as an insertion device and a variable inclined angle monochromator. This combination produces a monochromatic

X-ray with horizontal polarization. Figure 4.1 (a) shows the optical system of the STXM. The incoming monochromatic X-ray is focused on a sample by a Fresnel zone plate through an order select aperture. The X-rays are detected by a photomultiplier tube with a scintillator. By performing 2-dimensional scan of a sample, an X-ray transmission image is acquired.

Intensity of transmitted X-ray through the sample, $I(E)$, is expressed as Eq. (4.1), where $I_0(E)$, $\mu(E)$ and t are the original intensities of the X-ray, the absorption coefficient and thickness of the sample, respectively. As shown in Eq. (4.2), the energy dependence of optical density (OD) was obtained.

$$I(E) = I_0(E)e^{-\mu(E)t} \qquad (4.1)$$

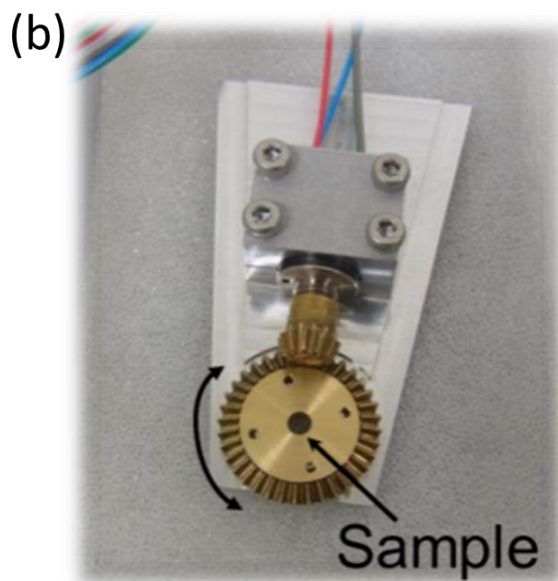$$\mathrm{OD} \equiv \mu(E)t = \ln\frac{I_0(E)}{I(E)} \qquad (4.2)$$
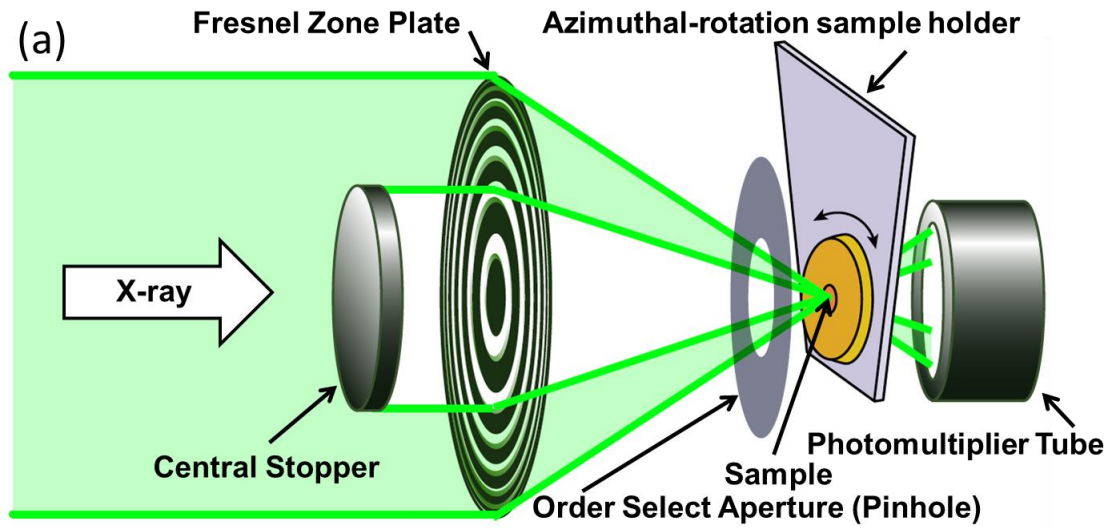
Figure 4.1 (a) Schematic figure of STXM optics and (b) a photo of the azimuthal-rotation sample holder.

Figure 4.1 (b) shows the azimuthal-rotation sample holder (Hernández-Cruz *et al.*, 2007, Ohigashi *et al.*, 2016). Therefore, two-dimensional map of X-ray absorption spectra can be measured by acquiring the X-ray absorption images with changing the energy of the incoming X-rays continuously. Then, detailed analysis of near edge X-ray absorption fine structure (NEXAFS) brings information of chemical structure of a specific element.

Figure 4.1 (b) shows the azimuthal-rotation sample holder (Hernández-Cruz *et al.*, 2007) used in this measurement. Details regarding the cell have been described previously (Ohigashi *et al.*, 2016). The rotation angle can be rotated clockwise or counterclockwise in 6° increments. The sample is measured in the STXM chamber filled with 0.01 atm of helium gas.

To determine the orientation angle of the π-orbital domain from the change of OD intensity (E=285.4 eV) at each sample position whose area is approximately 30×30 nm^2, the sample was rotated at multiple azimuthal rotation angles ($\phi = 0, 30°, 42°, 60°, 72°$, and $90°$) around the axis of the incident X-ray with horizontal linear polarization. As shown in Fig. 4.1(a), it is noted that the normal direction of the thin film sample is parallel to the axis and the azimuthal rotation direction was clockwise when see from the downstream side.

Powder X-ray diffraction (XRD) measurements were also performed to evaluate crystallinity of graphite in each CF using pulverized specimens. Powders of the sample were packed into an aluminum sample holder (sample part: φ 20 mm $\times$ 0.5 mm depth), and XRD measurements were performed with a diffractometer

(Smartlab, Rigaku Corporation). The tube current and tube voltage were set at 36 mA and 40 kV, respectively. The goniometer radius was 285 mm. A high-speed, one-dimensional detector was used as the X-ray detector, and measurements were performed using the Bragg-Brentano focusing geometry (i.e., the $K\beta$ filter method with Co $K\alpha$ using Fe filters). The measurement conditions were as follows: measurement angle range $2\theta = 15–40°$, step angle width $\Delta 2\theta = 0.02°$. The Halder–Wagner method was used to calculate the crystallite size of graphite (Halder *et al.*, 1966).

To evaluate the accuracy of these results by STXM, the author performed electron diffraction measurements using TEM. Electron diffraction measurements were performed with JEM-2100F (JEOL Ltd.). The acceleration voltage was 200 kV. The size of electron beam was 10 nm in the diffraction measurements. OneView-CMOS (Gatan, Inc.) was used as the detector. The orientation of the *c*-axis of the graphite crystals in the CFs was qualitatively evaluated from the position of the diffraction spots (rings).

In general, for the absorption of 285.4 eV, which is the energy derived from the excitation of $1s\rightarrow\pi*$ as shown in Fig. 4.2 (a) and (b), when the angle between the vector of the polarized electric field of X-ray and the vector of the direction of the π-orbit is θ, X-ray absorption intensity at E=285.4 eV is proportional to $\cos^2\theta$ (which is (a) maximum in case of $\theta = 0°$ and (b) minimum in case of $\theta = 0°$ (theoretically zero)) (Stöhr *et al.*, 1992; Watts *et al.*, 2011; Watts *et al.*, 2012). Because of this relationship, we observe a C *K*-edge spectra, especially at an intensity around $E = 285.4$ eV, depending on θ, as shown in Fig. 4.2 (c).
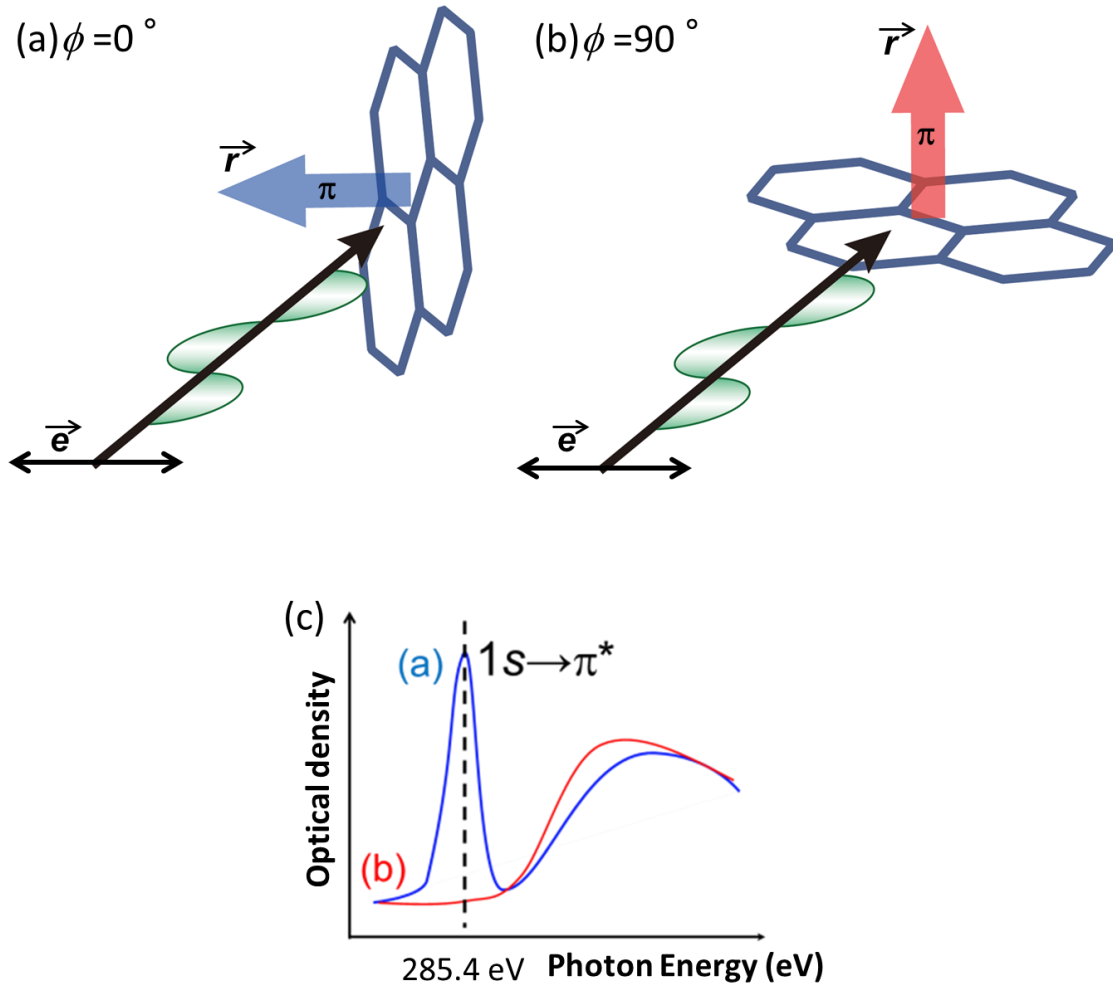
Figure 4.2 Positional relationship between polarization vector e and the direction of π-orbital (a) $\phi = 0\,°$, (b) $\phi = 90\,°$, (c) Schematic figure of C K-edge absorption spectra for (a) and (b).

4.3 Results and discussion

The author performed C K-edge mapping of the gray-dotted line area shown in Fig. 4.3 (a). Figure 4.3 (b) shows X-ray absorption image at $E=285.4$ eV, whose field of view is identical to the gray-dotted line area shown in Fig. 4.3(a). The STXM image of Fig. 4.3 (b) consists of 50×50 pixels (100 nm/pixel step).The similar contrast areas of several 100 nm to 1 μm were observed in the STXM image. These areas represent the π-orbital oriented domains. On the other hand, the crystalline size of graphite is 10.7 nm obtained from XRD pattern as explained in experimental section. This result revealed that the size difference between π-orbital oriented domains and the graphite crystallite is more than 100 times.

Figure 4.3 (c) represents the C K-edge spectra of each area in Fig. 4.3 (b). The colors of these spectra in Fig.

4.3 (c) correspond to that of the areas in Fig. 4.3 (b). The photon energy for π-orbital orientation analysis was selected to be 285.4 eV which corresponded to the excitation energy from 1s to π* of carbon, which originates from the C=C bond and whose OD intensities change depended on the relationship between the π-orbital orientation and X-ray polarization as shown in Fig. 4.3 (c).

As reported in Chapter 3 and shown in Fig. 4.4, the direction of laminated graphene planes inside the pitch-based CFs is almost parallel to the fiber axis. Therefore, analyzing the cross-section of CFs is sufficient for the evaluation of the distribution of π-orbital-oriented domains in CFs.
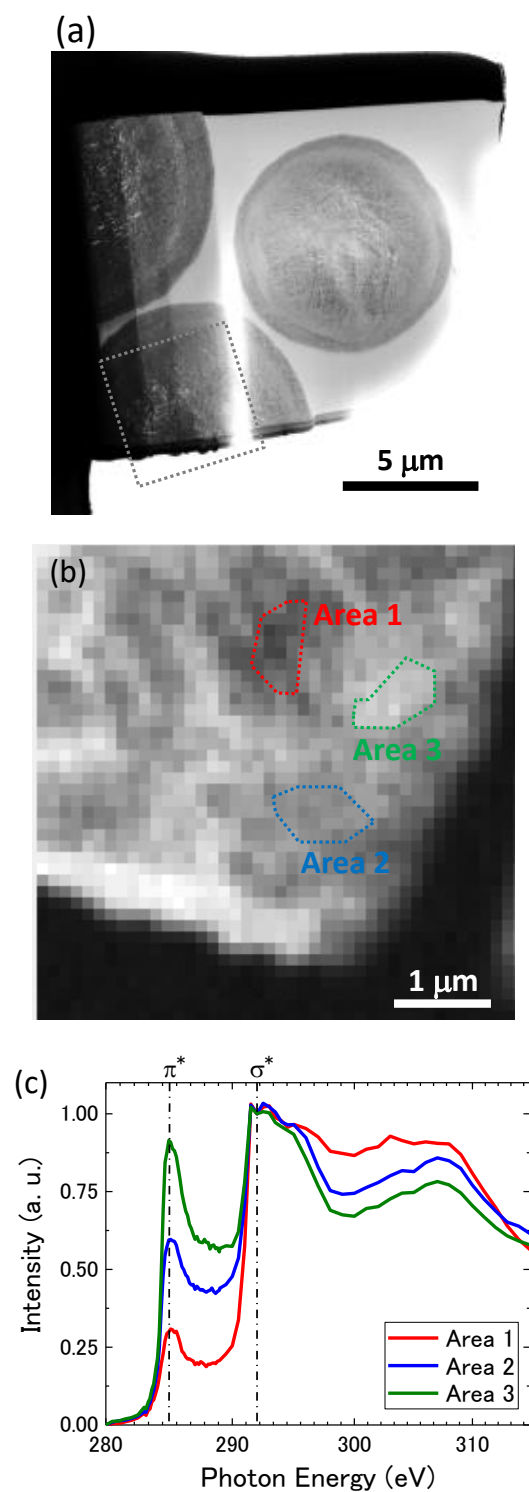
Figure 4.3 (a) TEM (bright field) images of the cross sections of CFs, (b) X-ray absorption image of a part of the cross-section of CF at E = 285.4 eV. (c) C K-edge spectra of areas shown in (b). The colors of the spectra in (c) correspond to that of areas in (b). (b) is displayed by rotating (a) so that (b) is horizontal.
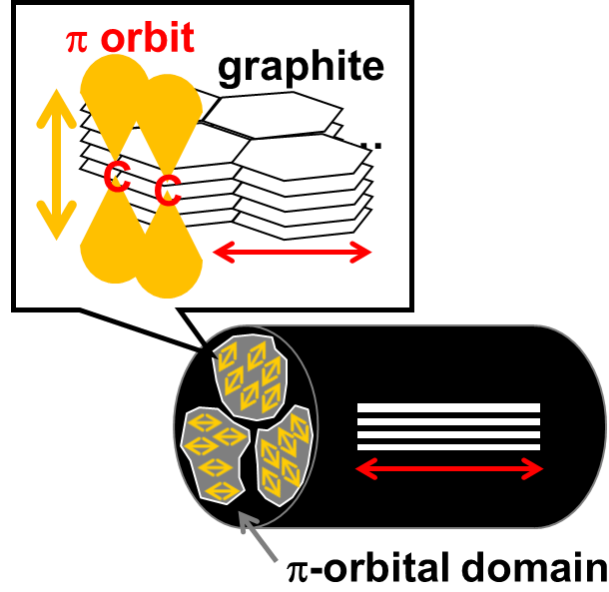
Figure 4.4 Microstructure of π-orbital-oriented domains and graphene stacked structure of a pitch-based CF. The red and yellow two-way arrows represent the directions of the graphene sheets along the fiber and within the fiber cross section, respectively.

Figure 4.5 shows cross-sectional images of the CF at each rotation angle $\phi = 0, 30, 42, 60, 72, 90°$. The images are tilted as the sample rotation at $\phi = 0°$. Red double arrows show the polarization of the incident beam. The STXM images consist of 333×333 pixels (30 nm/pixel) with $E = 285.4$ eV and dwell time = 3 ms. As the orientation of the π-orbital becomes near to the polarization of the incident beam, the ODs in the STXM image increases. This can also be confirmed from the results that the contrast of the X-ray absorption image is almost reversed at $\phi = 0$ and $90°$. It is note that the π^*/σ^* ratio (the OD of $1s \rightarrow \pi^*$ (285.4 eV) divided by that of $1s \rightarrow \sigma^*$ excitation (292.0 eV)) was used for the fitting of I in Eq. (4.3). By fitting the OD intensity I of sample position with Eq. (4.3), the average orientation angle θ_{ori} of the π-orbit at each sample position (30 nm diameter area) in the image can be obtained.
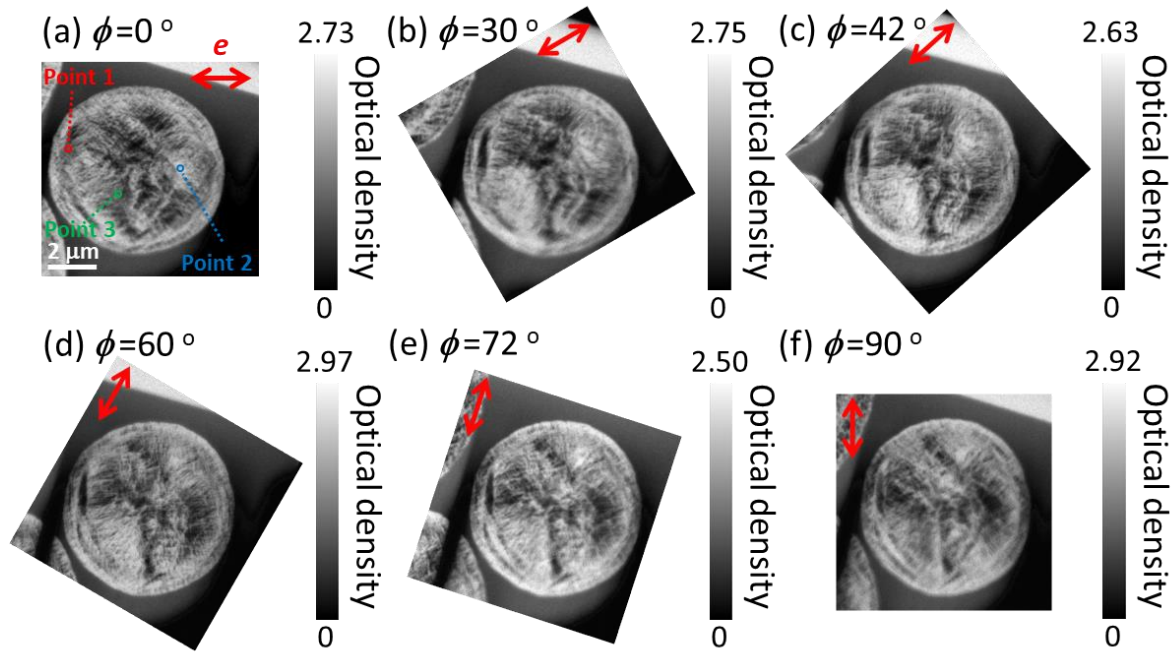
$$I = A\cos^2(\theta - \theta_{ori}) + B \quad (4.3)$$

Figure 4.5 OD images at $E = 285.4$ eV at rotation angles ϕ at 0°, 30°, 42°, 60°, 72°, and 90°. The red arrows in the figures indicate the X-ray polarization direction.

Here, A, B, and θ_{ori} are fitting parameters. Figure 4.6 shows the rotation angle ϕ dependence of OD intensity I and their fitting curve for three sample position as shown in Fig. 4.5. The average orientation angles θ_{ori} of the points 1, 2, and 3 in Fig. 4.5 (a) were obtained as 137°, 0.0°, and 42.4°, respectively. For nonlinear fitting of Eq. (4.3), the standard deviation/the corrected R^2 of the average orientation angles of each sample position were 0.23°/0.99, 2.6°/0.98, and 2.8°/0.87, respectively.

Figures 4.7 (a), (b), and (c) show an image of the cross-section of CF, colored with the value of θ_{ori}, A, and B at each sample position, respectively. In this way, we successfully visualized the distribution of the π-orbital with a spatial resolution of 30 nm, which is the same as that of STXM. Figure 4.7 (a) shows the color scale corresponding to the average π-orbital orientation angle at each sample position, originating from the stacked graphene sheet from $\theta_{ori} = 0-360°$. It is noted that $\theta_{ori} = 0-180°$ and $\theta_{ori} = 180-360°$ are equivalent angular ranges.

Figure 4.7 (a) is similar to the inverse pole figure (IPF) map of Electron back scatter diffraction (EBSD). EBSD complements X-ray diffraction (XRD) and is capable of analyzing crystal structure at a few tens of nanometer scale and has been widely used for characterizing the crystallographic features of inorganic materials

(Wilkinson *et al.*, 2012). The IPF map represents the distribution of the crystal orientation, whereas Fig. 4.7 (a) represents the distribution of average π-orbital orientation at each sample position in the image. This study is the first application of IPF maps for evaluation of the orientation distribution of carbon material and its related materials.
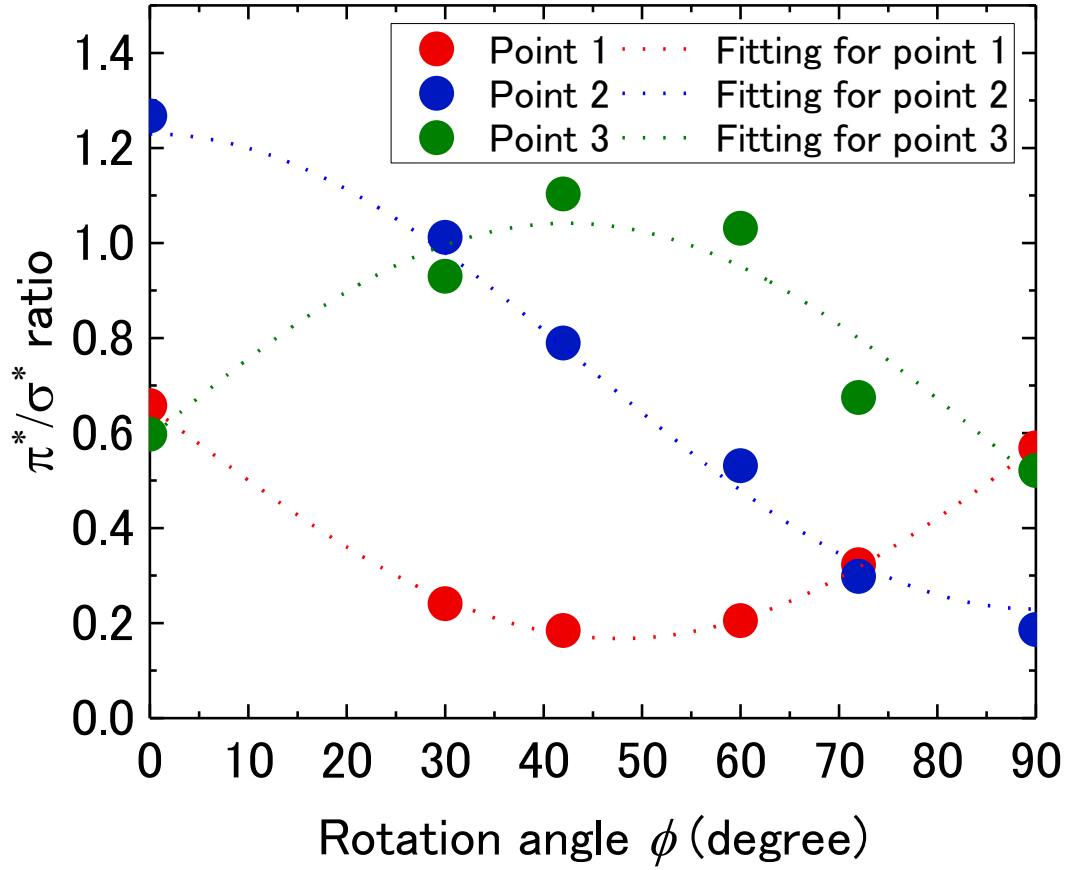

Figure 4.6 Relationship between rotation angle ϕ and OD intensity ratio (π^*/σ^*) and fitting curves by Eq. 4.3 for some sample points (1, 2, and 3) shown in Fig. 4.5. The average orientation angles θ_{ori} of the points 1, 2, and 3 were 137°, 0.00°, and 42.4°, respectively. For this nonlinear fitting, The standard deviation/the corrected R^2 of the average orientation angles of each sample position were 0.23°/0.99, 2.6°/0.98, and 2.8°/0.87, respectively.
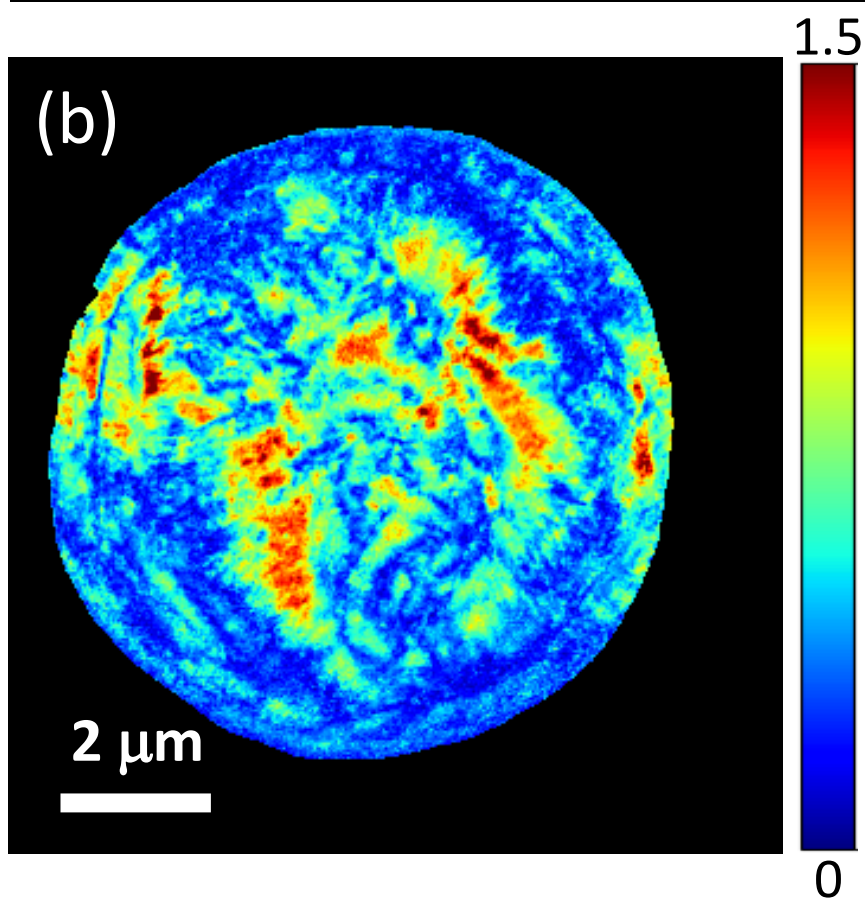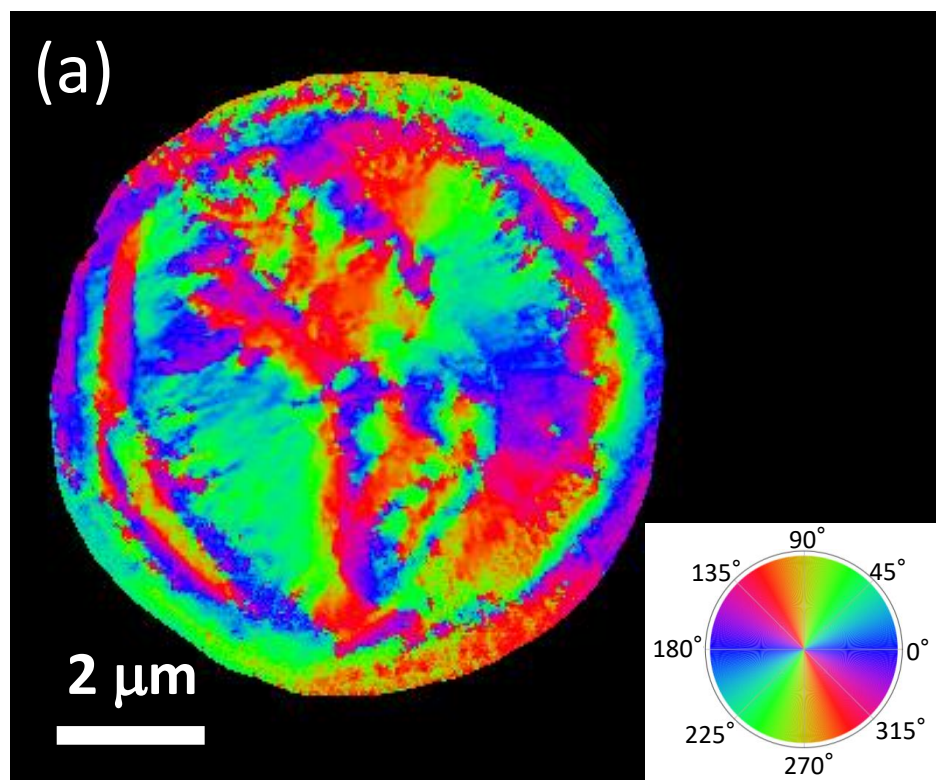
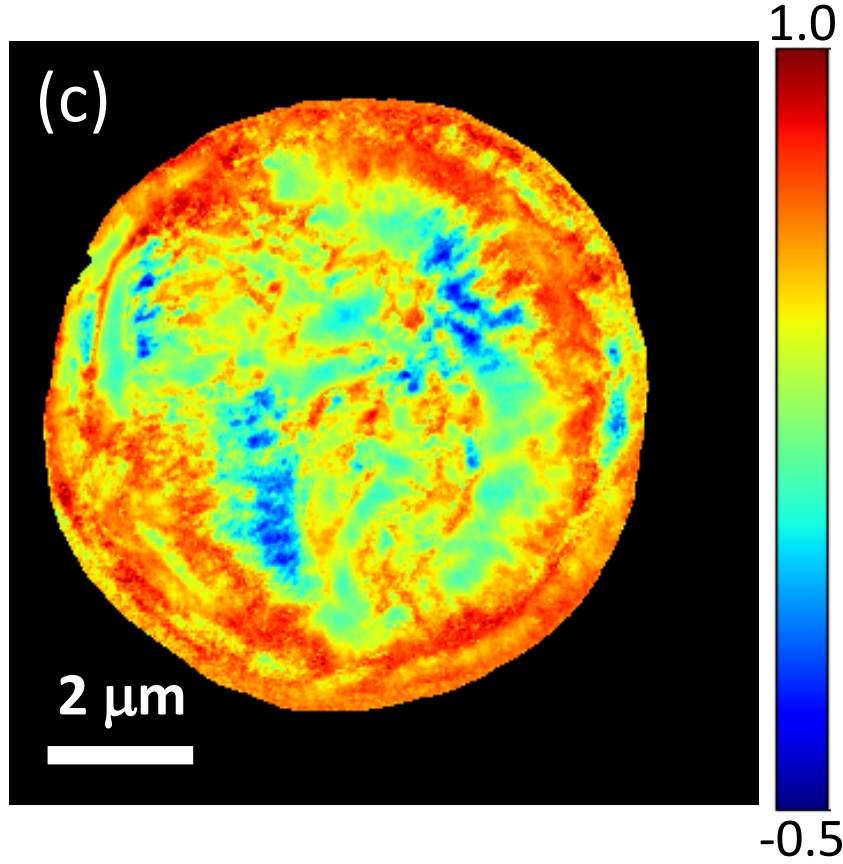**Figure 4.7** (a) π-orbital orientation θ_{ori} map, (b) Color map of A, (c) Color map of B in Eq. (4.3).

Figure 4.8 represents the positions of electron diffraction measurements in the cross-section of CF. The diffraction patterns are shown in Fig. 4.9. The white rings in Fig. 4.9 represent the 002 diffraction spots (rings) of graphite. STXM observes π-orbital orientations, while electron diffraction as shown in Fig. 4.9 observes the direction of crystal planes. These results are consistent with each other. This is because and the electron beam size (10 nm) in diffraction measurements is similar to X-ray beam size in STXM measurements and the crystallinity of graphite in CFs is high enough: crystallite size of graphite in XN50 was 10.6 nm. The crystallite size was calculated from XRD peak position and integral breadth of graphite (002). The Halder-Wagner method was used to calculate the crystallite size of graphite (Halder *et. al.*, 1966).

As we showed in Fig. 4.7, π-orbital oriented domains exist in various directions in CFs. The orientation angles of adjacent domains, domain size, and their heterogeneity can influence the mechanical properties of CFs

because graphite has structural anisotropy. To visualize there information in one map, we consider an image processing as follows. Figure 4.10 shows schematic figure of the idea for the image processing. The coordinate of any pixel in the image is defined as (x_i, y_j). When the orientation angle difference between (x_i, y_j) ($\theta_{ori}(x_i, y_j)$) and the average orientation angle ($\bar{\theta}_{ori}(x_i, y_j)$) among (x_{i-1}, y_{j-1}), (x_i, y_{j-1}), (x_{i+1}, y_{j-1}), and (x_{i-1}, y_j) is larger than the threshold orientation angle $\Delta\theta_{ori, thresh}$, we define (x_i, y_j) to be a pixel in a domain which is different from a domain where (x_{i-1}, y_{j-1}), (x_i, y_{j-1}), (x_{i+1}, y_{j-1}), and (x_{i-1}, y_j) are. In other words, as far as $\Delta\theta_{ori}\equiv|\theta_{ori}(x_i, y_j)- \bar{\theta}_{ori}(x_i, y_j)|$ is smaller than $\Delta\theta_{ori, thresh}$, adjacent pixels are considered to belong to one domain.

Figure 4.11 is illustrated by analyzing θ_{ori} map (Fig. 4.7 (a)) with various $\Delta\theta_{ori, thresh}$ using the condition as explained above. By comparing clustering maps with various $\Delta\theta_{ori, thresh}$, the orientation angle difference between domains and its spatial distribution can be visualized. However, the absolute value of $\Delta\theta_{ori, thresh}$ greatly depends on the material types and their manufacturing conditions. Therefore, to find optimal $\Delta\theta_{ori, thresh}$ that is useful to characterize the mechanical properties of CFs, it should be essential to continuously change the value of $\Delta\theta_{ori, thresh}$ and draw clustering maps for comparison among them. It is noted that the gray color and boundaries in the figure indicate that they were identified as different domains by their respective $\Delta\theta_{ori, thresh}$.

Distributions of θ_{ori} in Fig. 4.7 (a) are clustered in Fig. 4.11. This result shows domain boundaries with various threshold values of the difference of the orientation angle $\Delta\theta_{ori, thresh}$ (0.70－11.3°) between adjacent sample positions as explained above. This essentially corresponds to the grain map obtained by EBSD. The colors in Fig. 4.11 indicate that they were identified as different regions by their respective thresholds of $\Delta\theta_{ori}$.

Generally, the diameter of CFs after infusibilization, carbonization, and graphitization is approximately 30%-50% smaller than that of the CFs after spinning of the raw material pitch. Accordingly, if the difference of the orientation angle between adjacent domains during graphitization is large, the strain is concentrated on the boundary between the domains when CFs shrinks along to radial direction. The boundary might be considered as the starting point of the microstruc destruction.

For example, the number of domains colored by gray for the case of $\Delta\theta_{ori} = 3.52°$, as shown as Fig. 4.11 (f), is larger than that of the domains in the case of $\Delta\theta_{ori} = 7.03°$, as shown as Fig. 4.11 (k). It was suggested that the boundaries identified by $\Delta\theta_{ori} = 3.52°$ and $7.03°$ had a larger strain than those identified by only $\Delta\theta_{ori} = 3.52°$. In particular, it was suggested that boundaries with large strain were distributed in the outer peripheral portion (Fig. 4.11 (j)-(o)) as compared with the inside of the CF (Fig. 4.11 (d)-(i)). As a qualitative hypothesis, it was thought that large strains and defects (voids) would occur due to the shrinkage of the CF diameter during graphitization in the boundaries where the difference in orientation angle was large before graphitization. This study made it

possible to visualize the boundaries of strain concentration. Such knowledge can be one of the important analysis methods for designing the π-orbital orientation control of not only CFs but also other carbon materials.
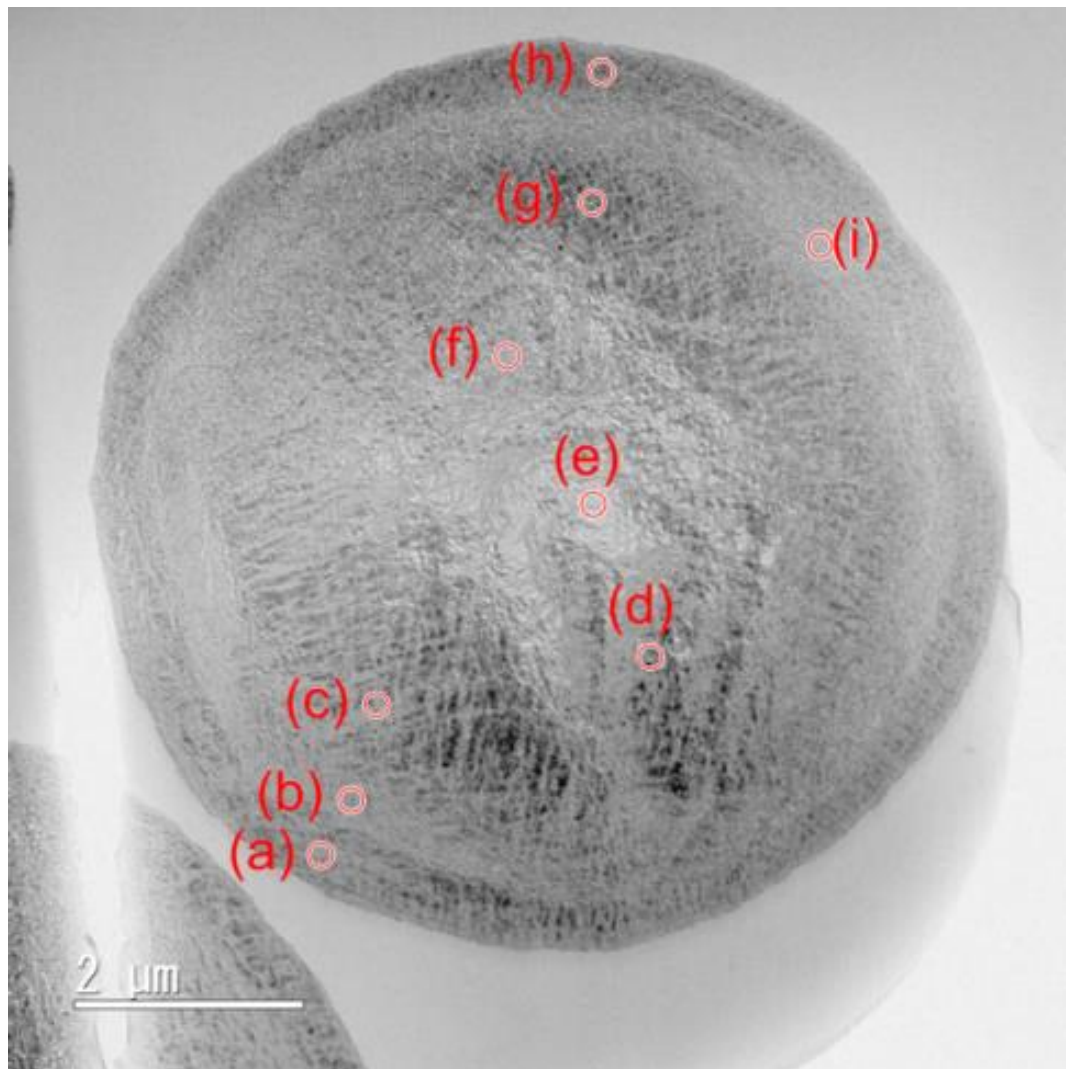

Figure 4.8 TEM image (bright field) of a cross-section of the CF, whose field of view is similar to that of the orientation map visualized by STXM (Fig. 4.7 (a)).
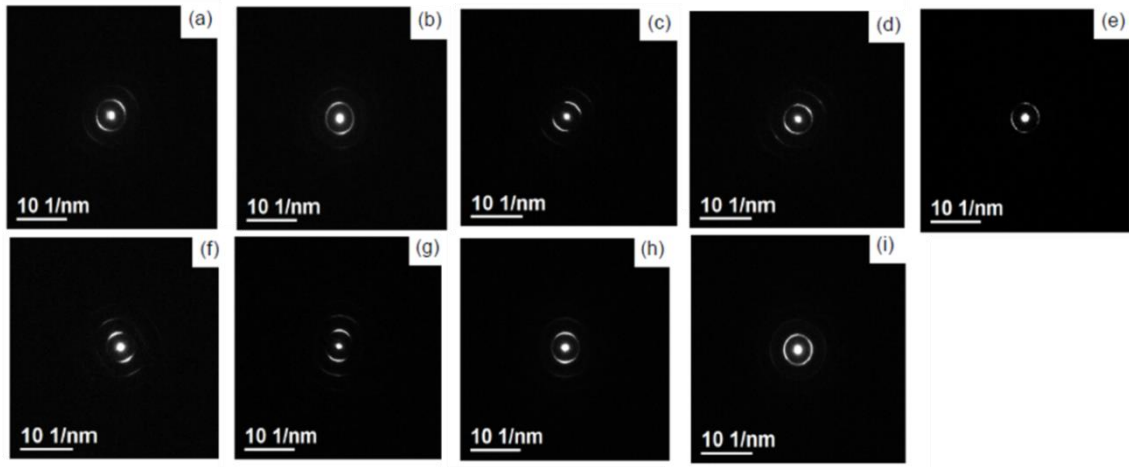
Figure 4.9 Electron diffraction patterns of points (a) to (i) in Fig. 4.8.

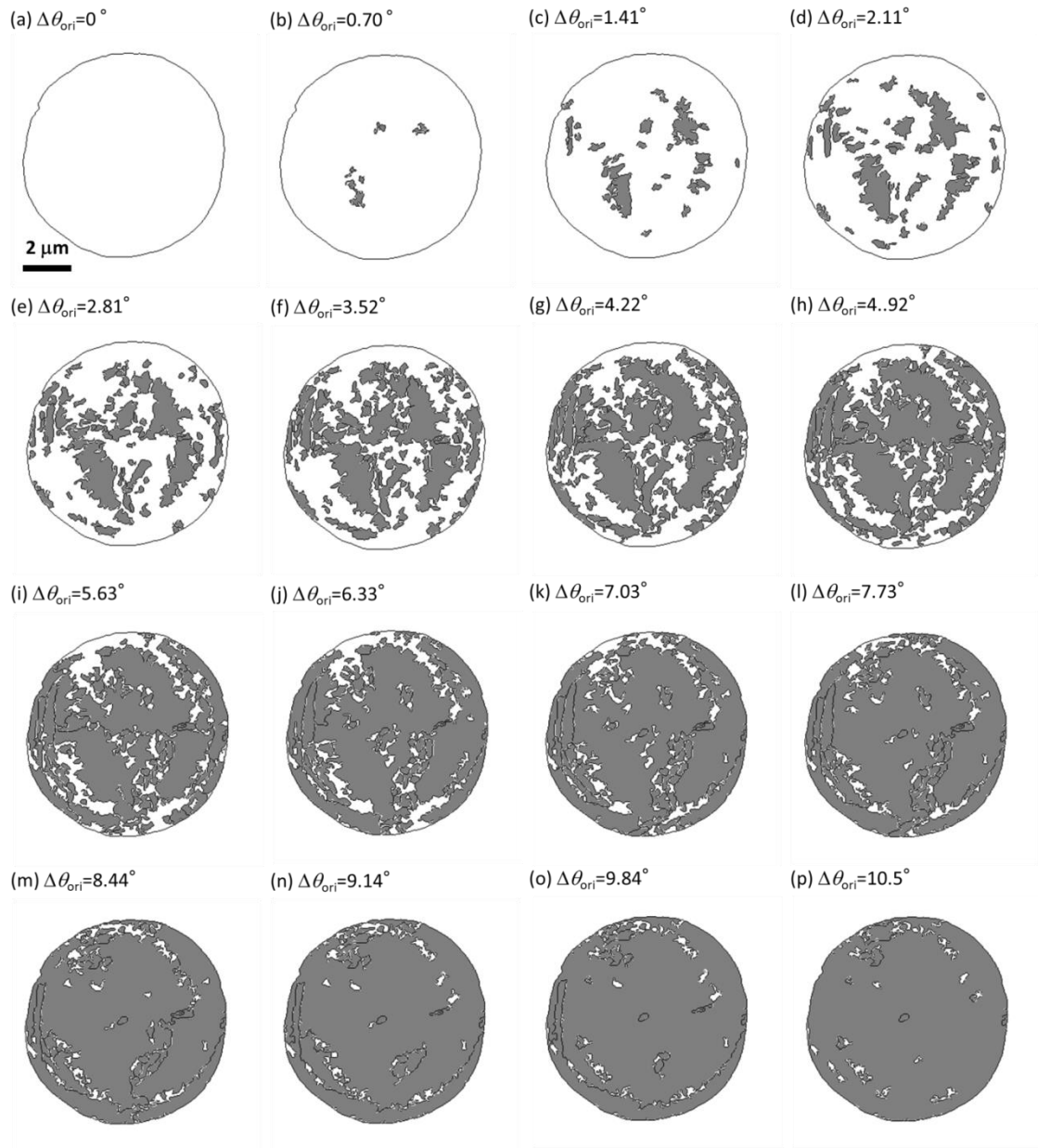**Figure 4.10** Schematic figure of the idea for the image processing.

Figure 4.11 Distribution of domain boundaries with various threshold values of the difference of the orientation angle $\Delta\theta_{ori}$ (0.70－11.3°). Different regions with $\Delta\theta_{ori}$ are indicated by the boundaries between white and gray areas.

4. Conclusion

The distribution of π-orbital oriented domains is one the most important factors to determine unique microstructures of CFs that is deeply related with macroscopic mechanical properties. In this study, the author visualized the distribution of π-orbital oriented domains of commercial pitch-based CFs with a spatial resolution

of nanometer scale using STXM.

The author combined X-ray absorption images whose contrast is π^*/σ^*, obtained at six rotation angles via STXM measurements. The author calculated the average orientation angle θ_{ori} of each sample position in the images using the theoretical relationship between the direction of the orbital and that of the X-ray polarization vector.

The π-orbital domains are visualized quantitatively, which is 100 times larger than the size of crystalline of graphite, suggesting that each domain consist of graphite crystallites. It was suggested that boundaries with large strain were distributed in the outer peripheral portion as compared with the inside of the CF.

This method will enable the evaluation of the relationship among domains in the CFs, which might be useful for strain mapping in the CFs. Such knowledge can be one of the important analysis methods for designing the distribution of π-orbital orientation domains to control mechanical properties of CFs. This method also can be applied to the other carbon materials for molecular orientation analysis.

References

Bradley, A. N., *Composites: Part A*, 2016, **91** 262.

Hernández-Cruz, D., Hitchcock A. P., Tyliszczak T., Rousseau M.-E., Pézolet M., In situ azimuthal rotation device for linear dichroism measurements in scanning transmission x-ray microscopy, *Rev. Sci. Inst.*, 2007, **78** 033703.

Gather, M. C., Bradley, D. D. C., An improved optical method for determining the order parameter in thin oriented molecular films and demonstration of a highly axial dipole moment for the lowest energy π-π* optical transition in poly (9,9 - dioctylfluorene - co - bithiophene), *Adv. Funct. Mater.*, 2007, **17**, 479.

Halder, N. C., Wagner, C. N. J., Separation of particle size and lattice strain in integral breadth measurements, *Acta Crystallogr.*, 1966, **20**, 312.

Hitchcock, A. P., *Handbook of Nanospectroscopy*, 2012, 745–791.

Kobayashi, T., Sumiya, K., Fukubaa, Y., Fujie, M., Takahagi, T., Tashiro, K., *Carbon*, 2011, **49(5)** 1646.

Lee, K. J., Chen, Z. Y., Structural heterogeneity and stress distribution in carbon fiber monofilament as revealed by synchrotron micro-beam X-ray scattering and micro-Raman spectral measurements, *Materials Chemistry and Physics*, 2003, **82(2)**, 428.

Li, H., Li, H., Lu, J., Sun, C., Wang, Y., Yao, D., Li, K., Wang, H., Improvement in toughness of carbon/carbon composites using multiple matrixes, *Materials Science and Engineering: A*, 2011, **530**, 57.

Matsumoto, T., Mesophase pitch and its carbon fibers, *Pure & Appl. Chem.*, 1985, **57(11)**, 1553.

Mochida, I., Yoon, S.-H., Korai, Y., Mesoscopic structure and properties of liquid crystalline mesophase pitch and its transformation into carbon fiber, *The Chemical Record*, 2002, **2**, 81.

Mochida, I., Yoon, S.-H., Takano, N., Fortin, F., Korai, Y., Yokogawa, K., Microstructure of mesophase pitch-based carbon fiber and its control, *Carbon*, 1996, **34(8)**, 941.

Naito, K., Yang, J.-M., Tanaka, Y., Kagawa, Y., The effect of gauge length on tensile strength and Weibull modulus of polyacrylonitrile (PAN)- and pitch-based carbon fibers, *J. Mater. Sci.*, 2012, **47**, 632.

Naito, K., Tanaka, Y., Yangb, J.-M, Kagawa, Y., Tensile properties of ultrahigh strength PAN-based, ultrahigh modulus pitch-based and high ductility pitch-based carbon fibers, *Carbon*, 2008, **46**, 189.

Ohigashi, T., Arai, H., Araki, T., Kondo, N., Shigemasa, E., Ito, A., Kosugi, N., Katoh, M., Construction of the scanning transmission X-ray microscope beamline at UVSOR, *J. Phys.: Conf. Ser.*, 2013, **463**, 012006-1.

Ohigashi, T., Nagasaka, M., Horigome, T., Kosugi, N., Rosendahl, S. M., Hitchcock, A. P., Development of in-situ sample cells for scanning transmission X-ray microscopy, *AIP Conf. Ser.*, 2016, **1741**, 050002.

Otani, S., On the carbon fiber from the molten pyrolysis products, *Carbon*, 1965, **3**, 31.

Otani, S., Yamada, K., Koitabashi, T., Yokoyama, A., On the raw materials of MP carbon fiber, *Carbon*, 1966, **4**, 425.

Soo-Jin, P., *Carbon Fibers* 2018, 101–133.

Stöhr, J, *NEXAFS Spectroscopy*, 2012, 169–172.

Yoon, S.-H., Takano, N., Korai, Y., Mochida, I., Crack formation in mesophase pitch-based carbon fibres: Part I Some influential factors for crack formation, *Journal of Materials Science*, 1997, **32**, 2753.

Yoon, S.-H., Korai, Y., Mochida, I., Crack formation in mesophase pitch-based carbon fibres: Part II Detailed structure of pitch-based carbon fibres with some types of open cracks, *Journal of Materials Science*, 1997, **32**, 2759.

Wagner, H. D., Amer, M. S., Schadler, L. S., Residual compression stress profile in high-modulus carbon fiber embedded in isotactic polypropylene by micro-raman spectroscopy, *Applied Composite Materials*, 2000, **7**, 209.

Watanabe, F., Korai, Y., Mochida, I., Nishimura, Y., Structure of melt-blown mesophase pitch-based carbon fiber, *Carbon*, 2000, 38(5), 741.

Watts, B., Ade, H., A simple method for determining linear polarization and energy calibration of focused soft X-ray beams, *J. Electr. Spectr. Rel. Phne.*, 2008, **162**, 49.

Watts, B., Schuettfor, T., McNeill, C. R., Mapping of domain orientation and molecular order in polycrystalline semiconducting polymer films with soft X-ray microscopy, *Adv. Funct. Mater.*, 2011, **21**, 1122.

Warwick, T., Franck, K., Kortright, J. B., Meigs, G., Moronne, M., Myneni, S., Rotenberg, E., Seal, S., Steele, W. F., Ade, H., Garcia, A., Cerasari, S., Denlinger, J., Hayakawa, S., Hitchcock, A. P., Tyliszczak, T., Kikuma, J., Rightor, E. G., Shin, H. J., Tonner B. P.., A scanning transmission x-ray microscope for materials science spectromicroscopy at the advanced light source, *Rev. Sci. Inst.*, 1998, **69(8)**, 2964.

Wilkinson, A. J., Britton, T. B., Strains, planes, and EBSD in materials science, *materialstoday*, 2012, **15**, 366.

Zheng, G., Sano, H., Suzuki, K., Kobayashi, K., Uchiyama, Y., Cheng, H.-M., Preparation and fracture behavior of carbon fiber/SiC composites by multiple impregnation and pyrolysis of polycarbosilane, *Carbon*,

1999, **37(12)** 2057.

Chapter 5

Development of Azimuthal-rotation Sample Holder for Molecular Orientation Analysis

5.1 Introduction

The physical properties of carbon materials, such as rubber, polymer-blend resins, carbon fibers, and carbon-fiber-reinforced plastics are based on the domain shape and size, as well as the spatial distribution and orientation of their chemical structures (functional groups and chemical bonding) of each phase (Miller *et al.*, 1987; Otani *et al.*, 1986; Soo-Jin, 2018). Scanning transmission X -ray microscopy (STXM) is used to observe the distribution of chemical structures with a spatial resolution that exceeded approximately 50 nm (Hitchcock, 2012). The X-ray absorption (XA) intensity (optical density (OD) is generally used for STXM measurements) reflects the interaction between the polarization of X-rays and the orientation of molecular or chemical bonding orbitals (Hernández-Cruz D. *et al.*, 2007, Watts *et al.*, 2011, Watts *et al.*, 2008). Through STXM, the distribution of orbital orientation can be determined by observing the variations in the OD contrast within the field-of-view (FOV) when the sample is rotated at multiple angles in the azimuthal direction of the incident X-ray (Ohigashi *et al.*, 2016, Watts *et al.*, 2011, Watts *et al.*, 2008). In previous holders, the focus depth of the Fresnel zone plate (FZP) and the FOV of the observations were around the micrometer order, and maintaining the error motion within that range was difficult. In this study, an azimuthal-rotation sample holder, which exhibited improvements in rotation accuracy and reduction in the displacement of the rotation axis during azimuthal rotation, was developed. Thus, the dependence of OD on the rotational angle was measured to investigate the domain derived from π-orbitals (carbon double bonds) in natural spherical graphite. Furthermore, the performance of the developed azimuthal-rotation sample holder was evaluated.

5.2 Experimental

Figure 5.1 (a) shows the developed azimuthal-rotation sample holder, with a weight of 90 g and thickness of 19.6 mm. The part of the holder attached to the STXM chamber and that supporting the motor were fabricated using aluminum alloy (A6061) and aromatic polyamide resin, respectively. The worm shaft was made of SUS416. The sample mounted on the center of the disk plate was fabricated using aromatic polyamide resin and could be rotated 360° with a minimum rotation angle of 0.002° using a small two-phase stepping motor (AM1020RC018008+10/1, Faulhaber Co., Ltd.) that was vacuum compatible. The aforementioned holders also use the same motor. The pulse signal from the controller (Tsuji Electronics Co., Ltd.) is converted into the drive signal by the motor driver (Faulhaber Co., Ltd.), as explained in previous papers (Hernández-Cruz D. *et al*., 2007, Ohigashi *et al*., 2016). It is critical to maintain the position of the sample in such a manner that it stays in focus during the sample rotation. Thus, the rotation was supported by a crossed roller bearing (REV2008CC0P5S, THK Co., Ltd.), which reduced backlash or errors when rotating the sample holder. The developed system could solve the problems that are often caused by brass bevel gear and conventional ball bearing, which has been used in previous research studies (Hernández-Cruz D. *et al*., 2007, Ohigashi *et al*., 2016), i.e., the slip in rotating axis during sample rotation, particularly when the sample position is displaced. The radial and axial runout tolerances were less than 5 µm/360° and less than 7 µm, respectively. Thus, the developed holder can be used to rotate the specimens at high angle accuracy.

Furthermore, STXM measurements were conducted using the BL-19A at the Photon Factory (Institute of Materials Structure Science, High Energy Accelerator Research Organization (KEK)). Figure 5.1 (a) shows the image of the developed azimuthal-rotation sample holder for the compact STXM (cSTXM) (Takeichi *et al*., 2016). Figure 5.1 (b) shows the image of the holder loaded in the cSTXM. The measurement mode corresponded to the transmission mode. The spatial resolution of this technique was improved by more than 50 nm following the application of an FZP. The order-sorting aperture is located between the FZP and sample. In this study, a photodiode was used as the detector. In addition, the APPLE-II type undulator of the BL-19 can generate synchrotron radiation X-rays with linear horizontal (LH) and liner vertical (LV) polarization modes (Sasaki *et. al.*, 1993). To investigate the molecular orientation, measurements must be performed using X-ray absorption near edge spectroscopy (XANES) at other polarization directions via sample rotation in addition to the two polarizations of the X-ray. Hence, by switching the polarization (LH or LV) and rotating the sample (θ_r = 0°–90°), the polarization angles (θ) of the electric field of the synchrotron radiation X-rays with respect to the sample can be changed from 0° to 180° (Fig. 5.1 (c)) as follows: $\theta = \theta_r + 0°$ (LH) or $\theta_r + 90°$ (LV). These

polarizations allow for the investigation of two types of relationships between the sample and electric field of the X-ray at the same rotation angle. This can reduce the total measurement by half or more. The aXis2000 software was used to analyze the image stack data (a set of XA images of a sequence of synchrotron radiation X-ray energies) (Hitchcock, 2009). Figure 5.1 (c) shows the direction of the electric field in the LH and LV polarization modes when viewed from downstream.

A natural spherical graphite sample was used for the STXM measurements. The sample was sliced into thin films through focused ion-beam (FIB) processing. Before slicing, the sample surface was coated with Pt to prevent damage by the ion beam. The thickness of the sample was adjusted to approximately 50 nm through Argon milling.
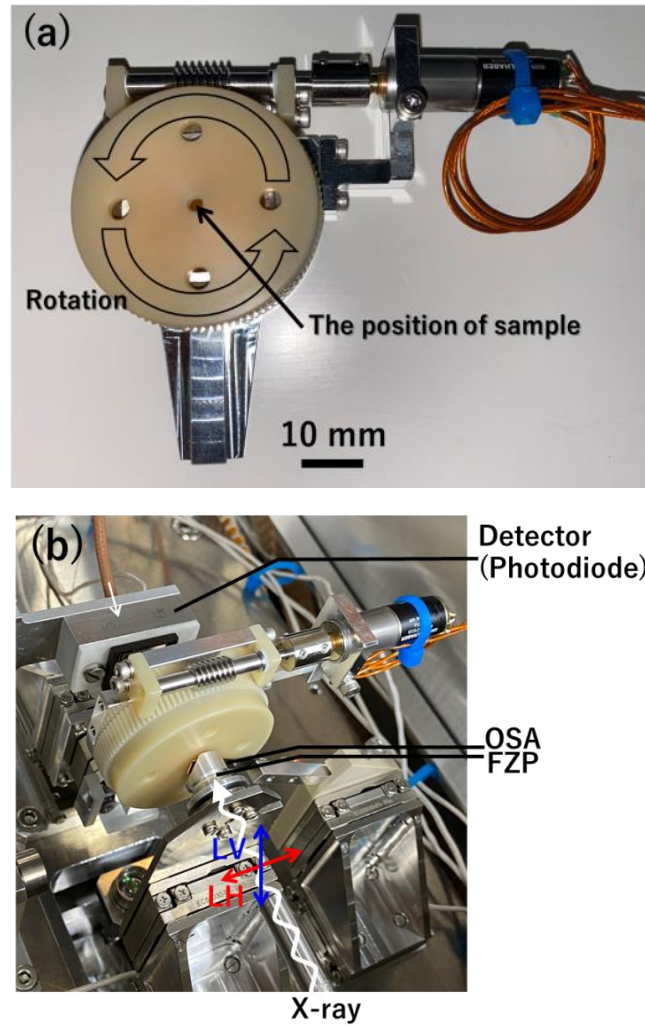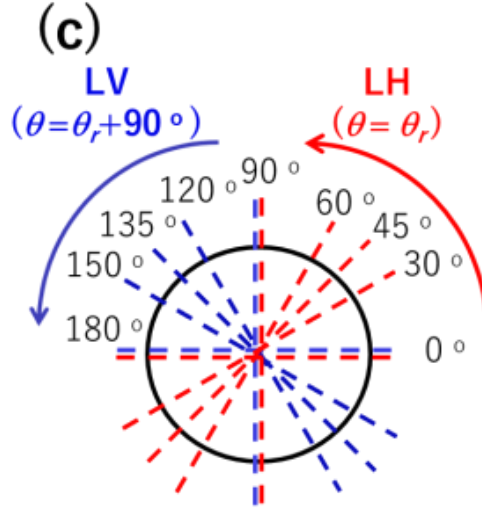
Figure 5.1 (a) Azimuthal-rotation sample holder developed for cSTXM. (b) Image of the holder used in cSTXM. (c) Direction of the electric field in the LH and LV polarization modes applied to the sample during the measurements (viewed from the detector side).

5.3 Results and discussion

Figure 5.2 shows the transmission electron microscopy (TEM) and XA images of the natural spherical graphite sample. In the TEM image (Fig. 5.2 (a)), the red dotted line shows the FOV of the XA image obtained by setting the cSTXM at $\theta = 0°$ ($\theta_r = 0°$, LH). Figures 5.2 (b), (c), and (d) shows the XA images at $\theta = 0°$ ($\theta_r = 0°$, LH) with different energies corresponding to 280.0 eV (pre-edge), 285.7 eV (1s→π*), and 292.0 eV (1s→σ*), respectively. The contrast in the XA images represents OD, which is dependent on the difference in energy among locations. Thus, the chemical structure and orientation of the π-orbitals varies with respect to locations. The OD yields the maximum value when the direction of the π-orbital is parallel to that of polarization (Brandes, 2008).

Figure 5.3 shows the XA images of the natural spheroidal graphite at 285.7 eV, measured at a wide range of angles from $\theta = 0°$ to $\theta = 180°$ with two linearly polarized X-rays (LH and LV). Furthermore, the FOV was 9 μm × 9 μm with a pixel size of 90 nm. The dwell time of X-ray detection at each pixel was 40 ms.
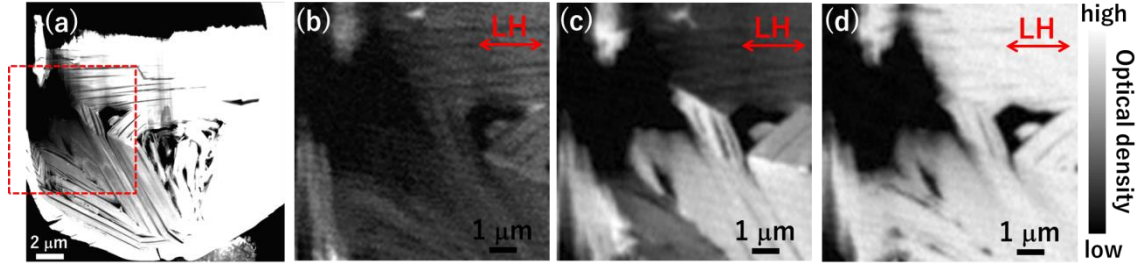
Figure 5.2 (a) TEM (dark field) image of natural spherical graphite. The red dotted line shows the FOV of an XA image obtained via cSTXM with a rotation angle of $\theta = 0°$ in the LH mode. XA images at $\theta = 0°$ (LH) with energies of (b) 280.0, (c) 285.7, and (d) 292.0 eV.
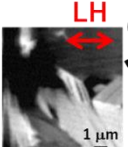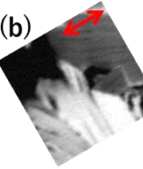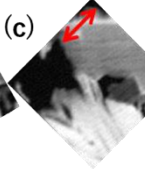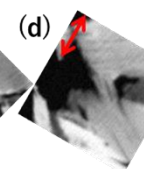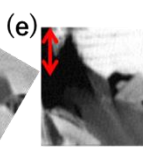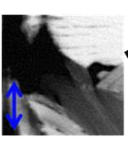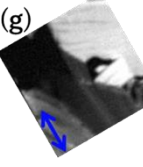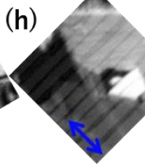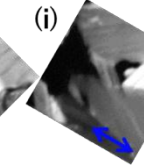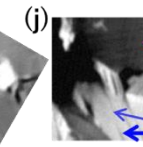

Figure 5.3 XA images of natural spheroidal graphite at 285.7 eV, measured at a wide range of polarization angles, $\theta = 0°$–$180°$ for the LH and LV polarization modes; the FOV is 9 μm × 9 μm with a pixel size of 90 nm.
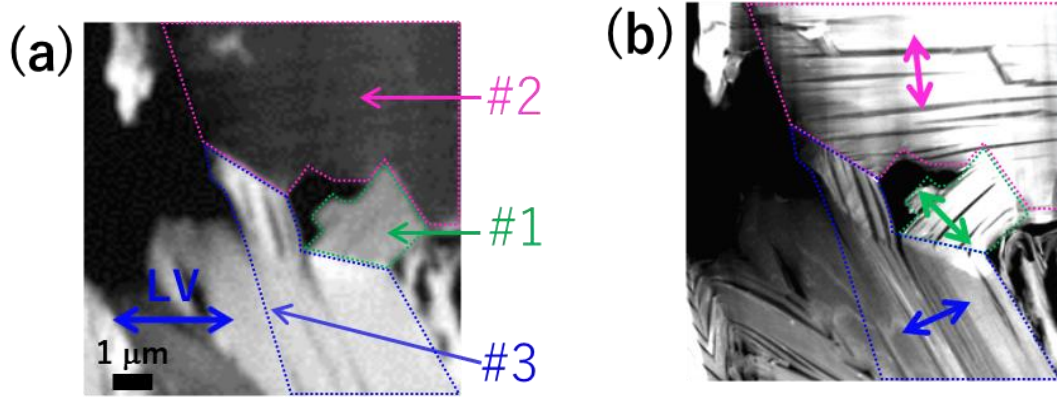
Figure 5.4 (a) XA images (OD contrast) of natural spheroidal graphite at 285.7 eV [Fig. 3(j)]. (b) TEM image of the FOV in (a). Areas enclosed within dotted lines (#1, #2, and #3) show π-orbital-oriented domains determined via cSTXM. The average orientation angles of domains #1, #2, and #3 are 134.3°, 96.5°, and 24.2°, respectively.

Figure 5.4 (a) shows the XA images of natural spheroidal graphite at 285.7 eV, which is similar to that in Fig. 5.3 (j), and Fig. 5.4 (b) shows the TEM image of the FOV in Fig. 5.4 (a). The areas enclosed within the dotted lines (#1, #2, and #3) of the π-orbital orientation were determined via cSTXM through the following procedure. Cleavage cracking in natural spheroidal graphite, as shown in Fig. 5.4 (b), was examined in each area. These cracks face a certain direction in each OD region, indicating traces of separation between the graphene sheets and suggesting that these domains exhibit different orientations in the π-orbital domains. A quantitative relationship between the orientations was investigated using cSTXM. Figure 5.5 shows the C *K*-edge XANES spectra in three areas (#1, #2, and #3) shown in Fig. 5.4 (a) at $\theta = 180°$. The intensity at $E = 285.7$ among the domains varied significantly, indicating the difference in the relationship between the polarization angle and direction of π-orbital. These spectra were weaker and broader than those of highly oriented pyrolytic graphite (HOPG) (Watts *et al*., 2008) because natural spherical graphite may be more sensitive to FIB and Argon milling, and the crystallinity of graphite in natural spherical graphite is lower than that of HOPG. In addition, these spectra may be affected by the sample oxidization. Figure 5.6 shows the rotational dependence of the π*/σ* ratio [the ratio between OD at 285.7 eV ($I(1s\rightarrow\pi *)$) and at 292 eV ($I(1s\rightarrow\sigma *)$)] on the polarization angles, θ, in areas #1, #2, and #3 shown in Fig. 5.4(a). Hence, the OD contrast clearly changes with respect to the polarization angle, θ. Furthermore, the contrasts of (a) and (j) as well as (e) and (f) in Fig. 5.3 show the same relationship in terms of the sample position and direction of the electric field. Thus, the change in XA intensity

is proportional to $\cos^2\theta$, as theoretically stated by Stöhr (Stöhr, 1992). In this case, π*/σ* is the ratio between I(1s→π *) and I(1s→σ *) and is expressed as follows:

$$\frac{\pi^*}{\sigma^*} \text{ ratio} = \frac{I(1s \to \pi^*: 285.7 \text{ eV})}{I(1s \to \sigma^*: 292.0 \text{ eV})} = A \times cos^2(\theta - \theta_{ori}) + B \quad (5.1)$$

where A, θ_{ori}, and B denote the amplitude of OD vibration, orientation angle of π orbital, and background constant, respectively. A dichroic response of 30% at 292.0 eV was reported for HOPG (Watts *et al.*, 2008). However, with respect to the natural spherical graphite in this study, the optical densities at 292.0 eV were found to be identical in three different areas (#1- #3) as shown in Fig. 5.5. The dichroic response at this energy, if present, can slightly deform the sinusoidal rotational response but has little effect on the spatial distribution of A, θ_{ori}, and B in equation (1). Therefore, we inferred that the intensity at 292.0 eV can be used to normalize the $1s$→π* intensity.

Based on the nonlinear fitting of equation (5.1), the three curves of solid lines are shown in Fig. 5.6. The average orientation angles of domains #1, #2, and #3 in Fig. 5.4 (a) were calculated to be 134.3°, 96.5°, and 24.2°, respectively (Fig. 5.4 (b)). The standard deviation/the corrected R^2 of the average orientation angles of domains #1, #2, and #3 were 0.95°/0.99, 3.1°/0.90, and 2.3°/0.95, respectively. The π*/σ* ratio at each position of the sample can be calculated using the aforementioned procedure.

Figures 5.7 (a), (b), and (c) show the maps of A, θ_{ori}, and B of equation (5.1), respectively. Note that this experiment cannot determine the three-dimensional direction of the π-orbital orientation because the experiment was aimed at detecting the projection component of the orientation vector on the sample surface. In this study, a sample portion with a relative in-plane facing π-orbital was fabricated as a thin film. The direction of separation or cracking observed in each sample area was perpendicular to the π-orbital direction. This is said to be reasonable when considering the bonding feature and because the direction of π-orbitals is perpendicular to that of graphene sheets. This shows that chemical-structure mapping (especially, in the direction of the π-orbital-oriented domain or graphene sheets) can be performed by combining cSTXM with the developed sample holder, and is not possible solely through microstructural observations using TEM.
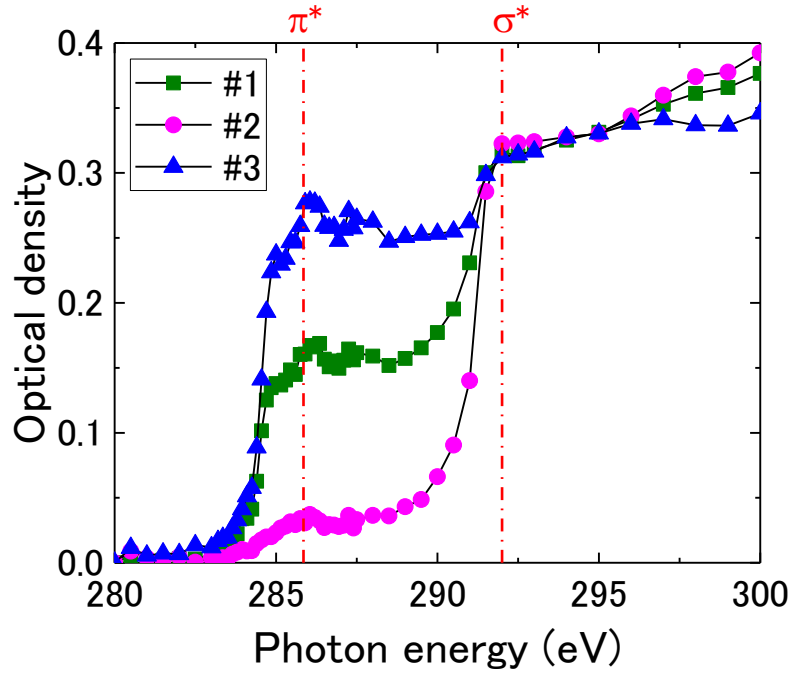
Figure 5.5 C *K*-edge spectra in domains #1, #2, and #3 for condition (j) in Fig. 5.3.
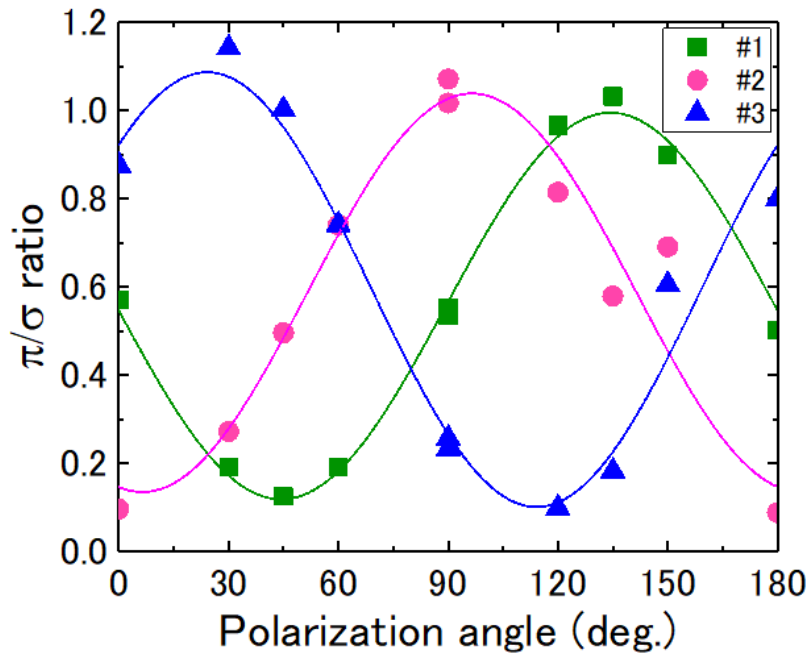
Figure 5.6 Rotational dependence of π*/σ* ratio (OD ratios at 285.7 and 292.0 eV) in areas #1, #2, and #3 shown in Fig. 5.3 (j). The three solid-line curves are the results of the nonlinear fitting based on Eq. (5.1).

2 µm

90°
135°   45°
180°   0°
225°   315°
270°

(b)

2 µm
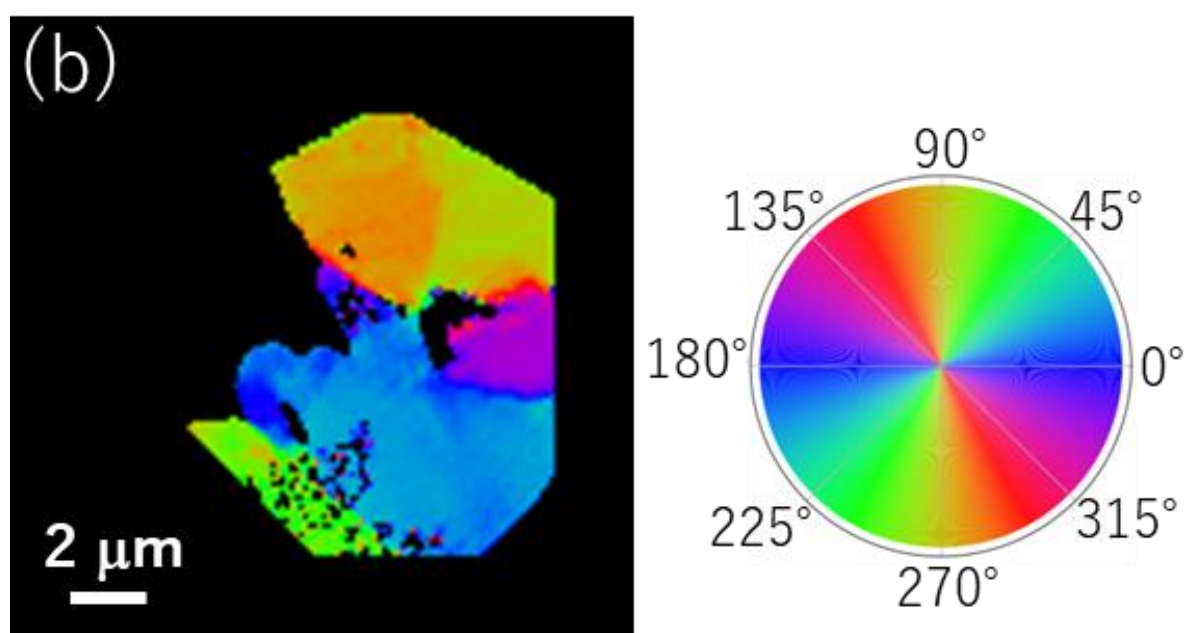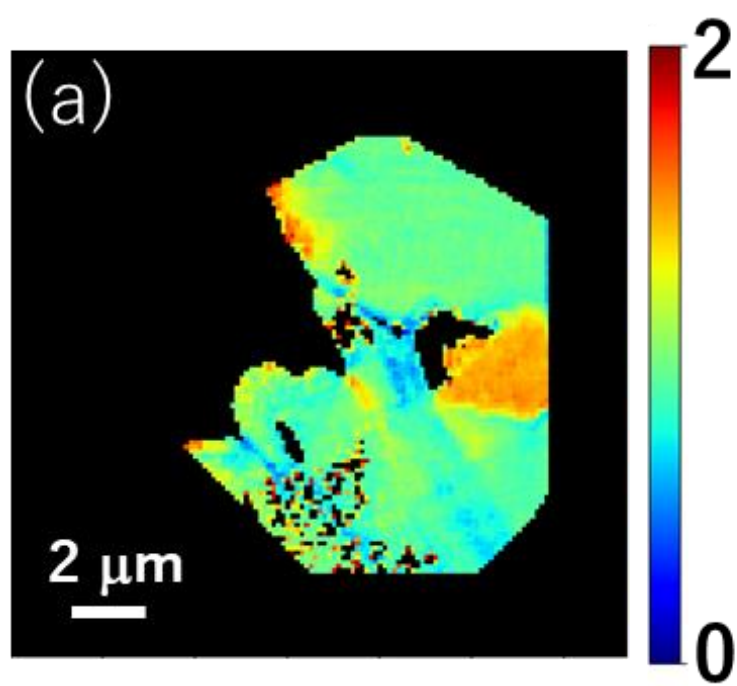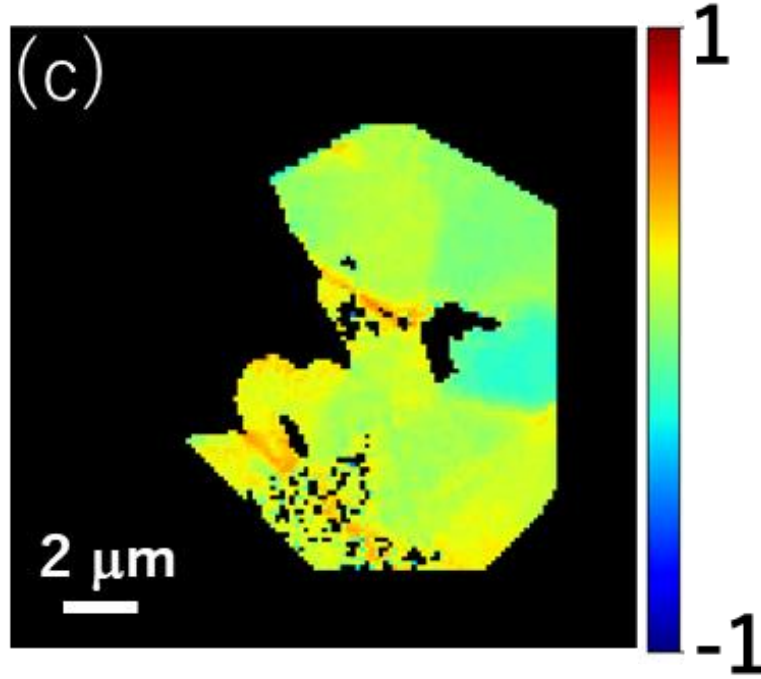
Figure 5.7 Maps of (a) amplitude (*A*), (b) orientation angle (θ_{ori}), and (c) background (*B*) of each sample position in equation (5.1).

5.4 Conclusion

In the study, an azimuthal-rotation sample holder was developed for an STXM. The holder exhibited improved accuracy of the rotation angle and deflection of the surface of the disk plate. To evaluate the performance of the holder, the π-orbital orientation domains in carbon materials were investigated. The average orientation angle in each of the sub-micrometer domains in natural spheroidal graphite was determined based on the dependence of π*/σ* ratio on the rotation angle.

References

Brandes, J. A., Cody, G. D., Rumble, D., Haberstroh, P., Wirick, S., Gelinas, Y., Carbon *K*-edge XANES spectromicroscopy of natural graphite, *Carbon*, 2008, **46(11)** 1424.

Hernández-Cruz D., Hitchcock A. P., Tyliszczak T., Rousseau M.-E., Pézolet M., In situ azimuthal rotation device for linear dichroism measurements in scanning transmission x-ray microscopy, *Rev. Sci. Inst.*, 2007, **78**, 033703.

Hitchcock, A. P., 2009, http://unicorn.mcmaster.ca/aXis2000.html.

Hitchcock, A. P., 2012, *Handbook of Nanoscopy*, 745–791.

Miller, B., Muri, P., Rebenfeld, L., A microbond method for determination of the shear strength of a fiber/resin interface, *Comp. Sci. Technol.*, 1987, **28** 17.

Ohigashi, T., Nagasaka, M., Horigome, T., Kosugi, N., Rosendahl, S. M., Hitchcock, A. P., Development of in-situ sample cells for scanning transmission X-ray microscopy, *AIP Conf. Ser.*, 2016, **1741**, 050002.

Otani, S., Oya, A., Progress of Pitch-Based Carbon Fiber in Japan, *ACS Symp. Ser.*, 1986, **303**, 323–334.

Sasaki, S., Kakuno, K., Takada, T., Shimada, T., Yanagida, K., Miyahara, Y., Nuclear instruments and methods in physics research section A: accelerators, spectrometers, detectors and associated equipment, *Nucl. Instrum. Methods. Phys. Res. A*, 1993, **331**, 763.

Soo-Jin, P., *Carbon Fibers*, 2018.

Stöhr, J., *NEXAFS Spectroscopy*, 1992.

Takeichi, Y., Inami, N., Suga, H., Miyamoto, C., Ueno, T., Mase, K., Takahashi, Y., Ono, K., Design and performance of a compact scanning transmission X-ray microscope at the Photon Factory, *Rev. Sci. Instrum.*, 2016, **87,** 013704-1.

Watts, B., Ade, H., A simple method for determining linear polarization and energy calibration of focused soft X-ray beams, *J. Electr. Spectr. Rel. Phne.*, 2008, **162**, 49.

Watts, B., Schuettfor, T., McNeill, C. R., Mapping of domain orientation and molecular order in polycrystalline semiconducting polymer films with soft X-ray microscopy, *Adv. Funct. Mater.*, 2011, **21**, 1122.

Chapter 6

Observation of Interface between Resin and Carbon Fiber in Carbon-Fiber-Reinforced Plastics

6.1 Introduction

Investigation of the microstructures, and interface between materials to reveal the origins of the physical properties of composite materials is essential. For example, chemical states (valence, functional groups etc.) around the interface between carbon fiber (CF) and resin in carbon-fiber-reinforced plastic (CFRP) is extremely helpful in the clarification of enhancement mechanisms of tensile strength and elastic modulus. Conventional techniques for these investigations include infrared absorption spectroscopy (IR), X-ray photoelectron spectroscopy (XPS), and XANES (X-ray absorption near edge structure). However, the spatial resolutions of these techniques are ordered from mm to μm, making it difficult to observe the interface structures in detail. On the other hand, the spatial resolution of electron microscopes (e.g. electron energy loss spectrometry (EELS)) is significantly higher (but less than 1 nm) than those of conventional spectroscopy techniques. However, the energy resolution of EELS is relatively lower (~0.5 eV) and the beam damage of samples is more severe than those of X-ray and IR probes, especially in organic compounds. Over the past ten years, lithographic fabrication techniques have enabled us to use optical devices such as Fresnel zone plates (FZP) whose spatial resolution is 20-100 nm. Scanning transmission X-ray microscopy (STXM) based on the sub-micron XANES imaging technique is a very powerful method of chemical imaging around the interface of composite materials (Ade *et al.*, 1992; Ade *et al.*, 1993). In this study, we performed C *K*-edge absorption imaging to analyze the distributions of chemical states in CFRP.

6.2 Experimental

CFRP thin film was fabricated via focused ion beam processing and its surface polished through argon ion beam milling. The thickness of the film was adjusted to approximately 80 nm to obtain C *K*-edge absorption

81

spectra of CF and resin in CFRP. The CFRP analyzed in this study is a commercial product consisting of CF made from polyacrylonitrile (PAN) and epoxy resin. The estimated tensile strength and elastic modulus of this CFRP are 1760 MPa and 125 GPa, respectively. Fig. 6.1 (a) shows a schematic of the cross section (CS) and longitudinal section (LS) of the CF. Figure 6.1 (b) presents a backscattered electron image of the CFRP thin film. Notably, the angle between the incident direction of the electron beam and normal vector of the thin film is 35°. I collected image stacks of C K-edge XANES in the red-dotted square regions ((I) the interface region between CF and resin, and (II) CS of CF) in Fig. 6.1 (b). Figure 6.1 (c) shows a transmission electron microscope (TEM) image of CF (CS) and resin. An inner ring microstructure was observed in CF (CS), and details are discussed in the next section.

STXM measurements were performed at BL-13A of Photon Factory, IMSS, KEK. The compact STXM instrument (cSTXM) (Takeichi et al, 2016) obtains XANES imaging at a spatial resolution of 40 nm using FZP, and is especially suited to the measurement of XANES spectra around C K-edges, providing information on chemical states around carbon. Moreover, the undulator of BL-13 can generate radiation light source switched to horizontal and vertical linear, left and right-handed circular and elliptical polarization states by APPLE-II type undulators (Tsuchiya et al., 2013; Sasaki et al., 1993). Details of the cSTXM instrument have been discussed elsewhere (Takeichi et al, 2016). In this study, only horizontal linear polarized X-ray beams were used. The aXis2000 software was used to analyze the image stacks (Hitchcock, 2009).
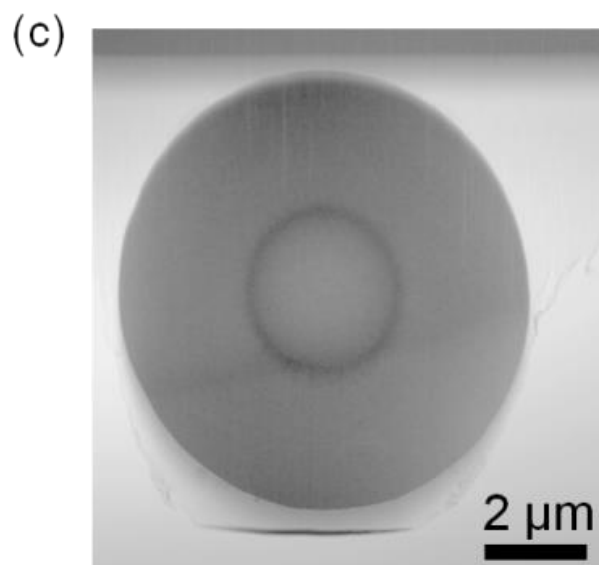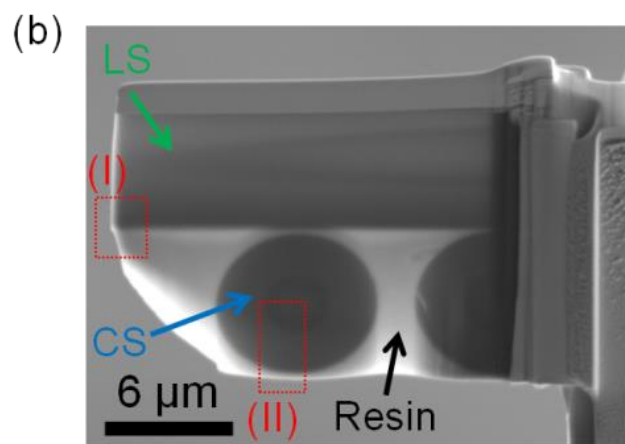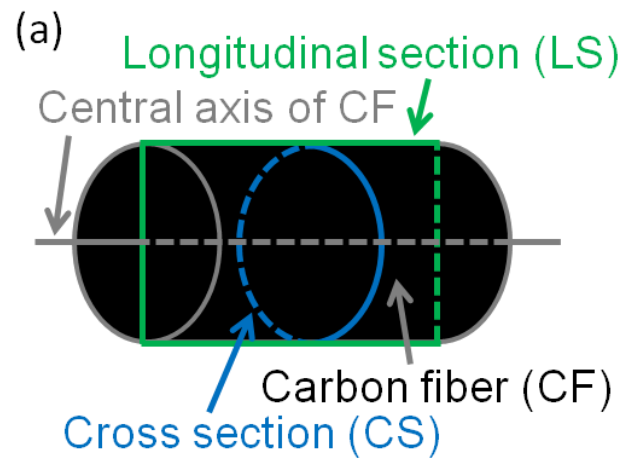
Figure 6.1 (a) Schematic of the cross section (CS) and longitudinal section (LS) of CF. (b) Backscattered electron image of CFRP thin film. (c) Transmission electron microscope image of CS of CF and resin.

6.3 Results and discussion

Figure 6.2 (a) shows an X-ray absorption contrast image around the interface between CF and resin labeled as (I) region in Fig. 6.1 (b) and obtained at E=286.5 eV, corresponding to the transitions from $1s$ to π^* (phenolic (C*-OH)). This image consists of 70×70 pixels (pixel size is 40×40 nm). Around the interface between CF and resin, another absorption contrast that was neither accounted for by CF nor resin was observed. This suggests the presence of another phase around the interface. Image stack measurements around the C K-edge absorption were carried out as shown in Fig. 6.2 (a). Figure 6.2 (b) shows C K-edge XANES spectra of resin (red), CF (LS) (green), and interface (blue). These are averaged spectra of the square regions enclosed in black dashes (i), (ii), and (iii) in Fig. 6.2 (a), respectively. These spectra are normalized by the intensity of the peak top of the transitions from $1s$ to π^* of C=C around 285.0 eV. The split peaks in the XANES spectrum of the region of (i) resin at approximately 284.8 eV correspond to the transition from $1s$ to π^* of C=C, while the other peaks at 286.5 and 288.3 eV correspond to the transitions from $1s$ to π^* (phenolic (C*-OH)) and those from $1s$ to Rydberg/σ^* ((O(C*-H)R)), respectively (Moffet, 2011). Moreover, the broader peak at approximately 292 eV corresponds to the transitions from $1s$ to σ^* of C-C. These are consistent with the typical chemical structure of the epoxy resin (Hedrick, 1992). In the case of the spectrum of (ii) CF (LS), only two peaks were observed at 285.1 eV and at approximately 292.0 eV, corresponding to the transitions ranging from $1s$ to π^* of C=C and those ranging from $1s$ to σ^* of C-C, respectively. This means that CF consists of stacks of graphene sheets. On the other hand, the interfaces of the peak positions of the spectrum of (iii) are the same as those of (i). However, the intensity ratio among the peaks of (iii) is different from those of (i). These observations suggest that the organic material around the interface consists of the same functional groups as those of resin but with different a compositional ratio. This result is consistent with the general manufacturing process of CFRP, whereby the CF is coated with organic material before being embedded in resin to improve the affinity between CF and resin.
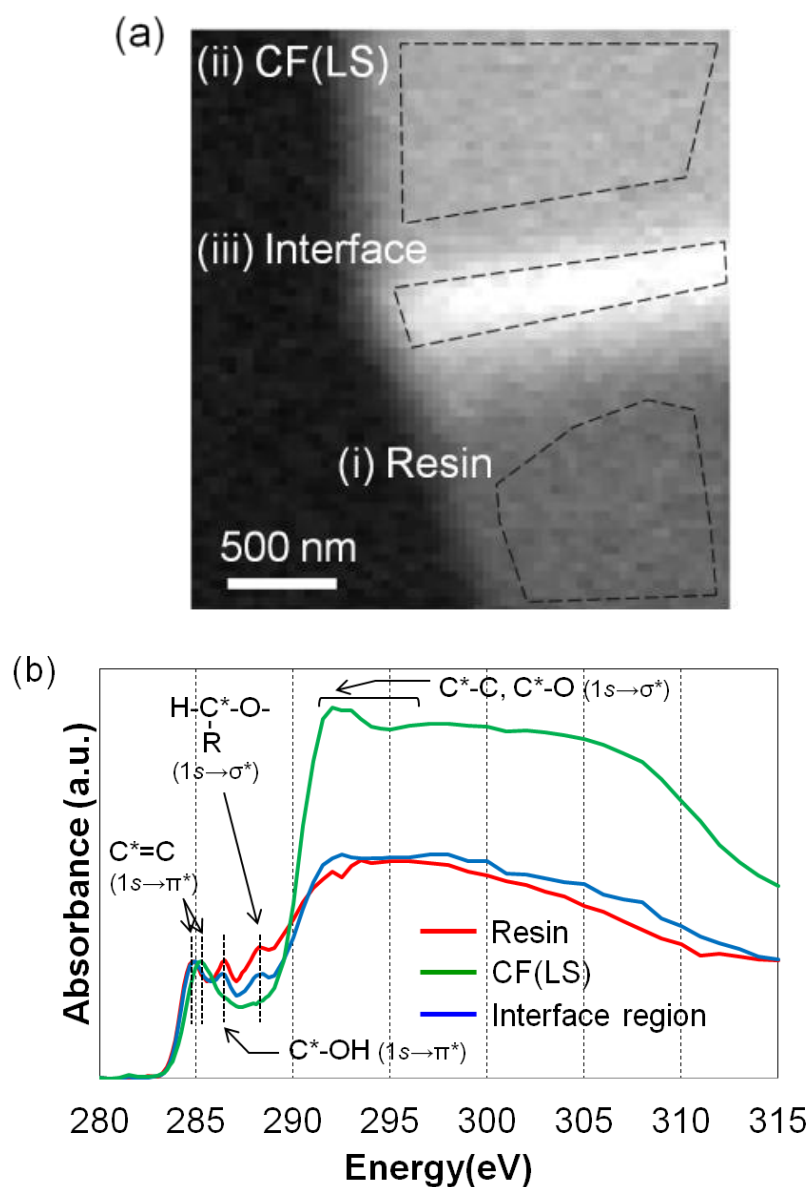
Figure 6.2 (a) Sections enclosed by black dashes show regions for averaged XANES spectra of (i) resin, (ii) CF (LS), and (iii) interface used for RGB deconvolution. (b) Averaged XANES spectra of resin (red), CF (LS) (green), and interface (blue) in each region shown in Fig. 6.2 (a).

First, to determine the presence of the third phase between CF and resin, two types (A and B) of singular value decomposition (SVD) analyses were carried out; (A) by using (i) and (ii) excluding (iii) shown in Fig. 6.2 (a), and (B) by using averaged spectra of (i) resin, (ii) CF (LS) and (iii) the interface, respectively. These averaged spectra are shown in Fig. 6.2 (b). Residual curves of the three regions after SVD analyses of (A) and (B) are shown in Fig. 6.3 (a) and (b), respectively. Both regions of (i) and (ii) fit in excellently in both cases. By contrast,

the region of (iii) could fit in only in the case of (B). Based on spectra analysis, the third phase was inferred to be present in the interface, which is neither CF nor resin. An RGB color deconvoluted image of SVD of (B) using three spectra is shown in Fig. 6.3 (c). The thickness of the third phase was approximately 100 nm. In addition, a transition region of approximately 300 nm in thickness was observed at the boundary of the resin and third phase.
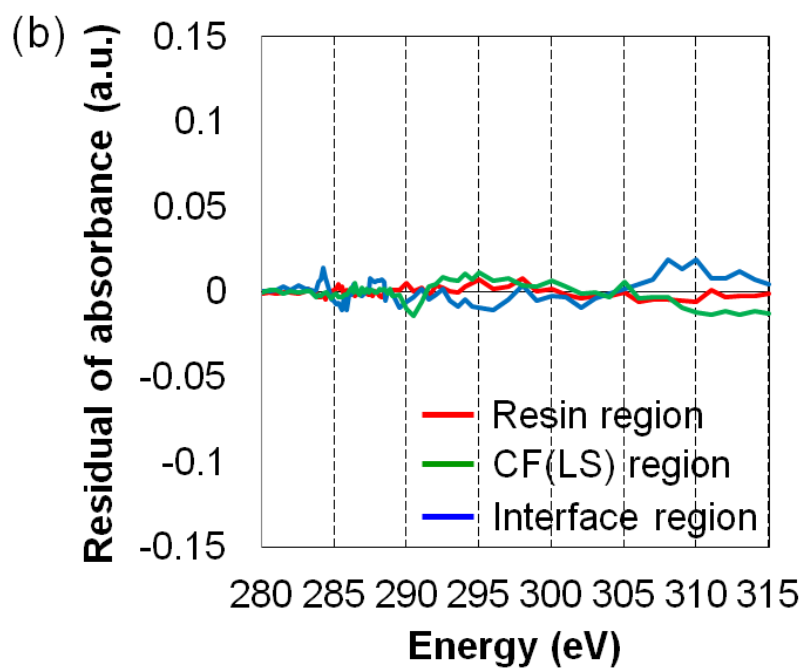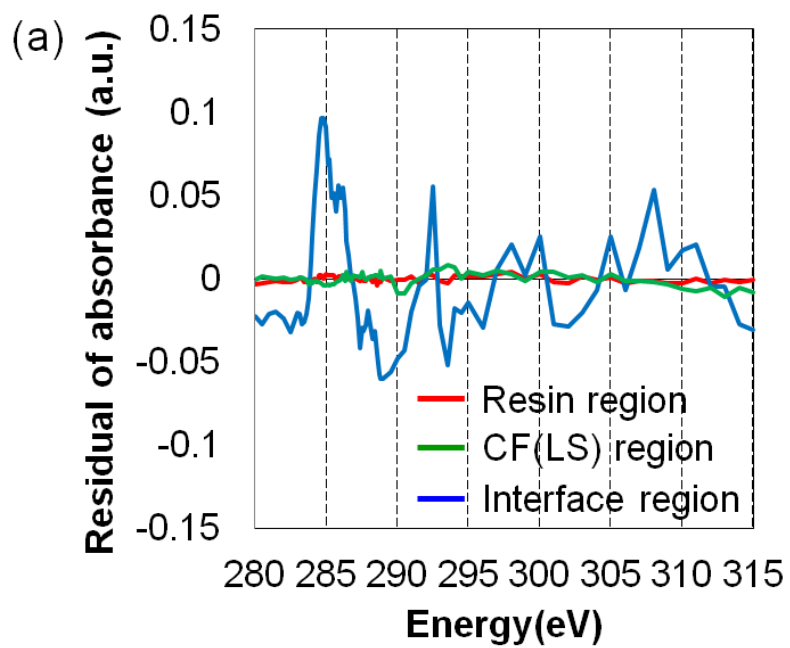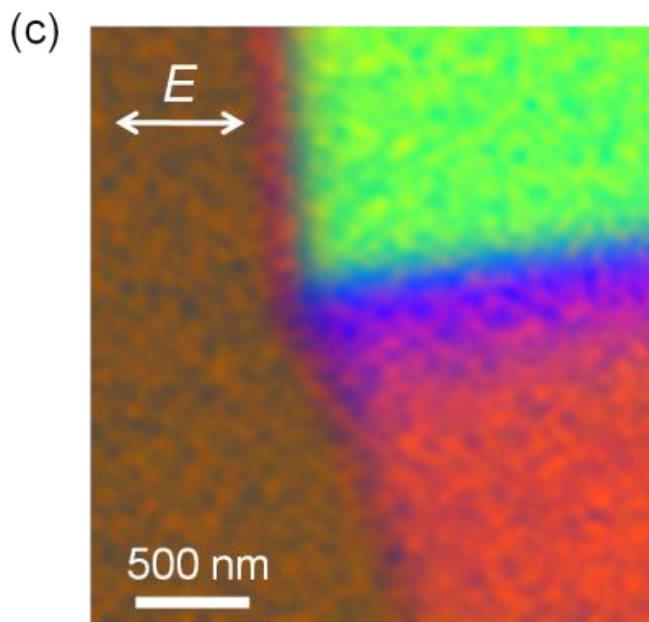
Figure 6.3 Residual curves of each region after SVD analyses of (A) resin/CF(LS) and (B) resin/CF(LS)/interface were shown in (a) and (b), respectively. (c) RGB (red: resin, green: CF (LS), blue: the third phase) color deconvoluted image of the interface between resin and CF (LS). The two-way arrow represents the polarization of X-ray beams.

Subsequently, I performed image stack measurements of region (II) in Fig. 6.1 (b) to investigate the chemical state of the inner ring observed in CF (CS). C K-edge spectra of resin (red), CF (CS) (green), and inner ring in CF (CS) (blue) are shown in Fig. 6.4 (a). These spectra are the averages of each region and are normalized by the intensity of the peak top of the transitions from $1s$ to π^* of C=C as well as Fig. 6.2 (b). The configuration of the inner ring is almost the same as that of CF (CS). This means that the chemical state of the inner ring was not different from that of CF. The contrast of the inner ring in CF (CS) observed in the TEM and X-ray absorption contrast images may be attributable to the difference between their densities.

Finally, the intensity ratio of the transitions from $1s$ to π^* to those from $1s$ to σ^* varied in the cases of LS (green spectrum in Fig. 6.2 (b)) and CS (green spectrum in Fig. 6.4 (a)) of CF. This means that the π orbital in CF is perpendicular to the central axis of CF. The XANES peak of a particular electron orbital is sensitive to the relationship between the orientation of its electron orbital and the polarization of incident X-ray beams (Watts, 2011). The XANES intensity originated from a particular orbital is enhanced when the orientation of its orbital is parallel to the polarization of the X-ray. From these results, it was concluded that the graphene sheets oriented

to the fiber axis direction as schematically illustrated in Fig. 6.4 (c).
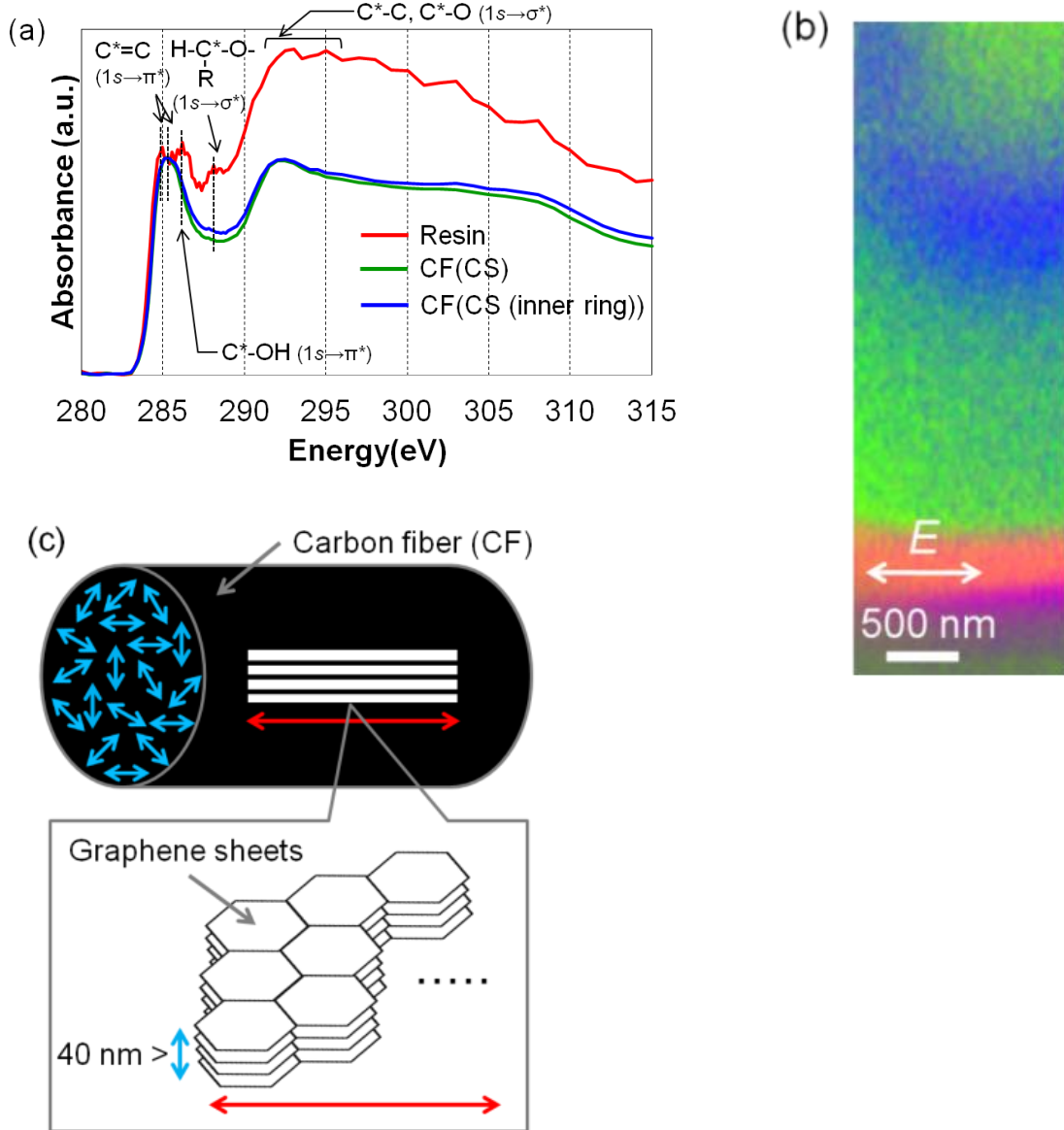
Figure 6.4 (a) Averaged XANES spectra of resin (red), CF (LS) (green), and inner ring in CF (CS) (blue) in each region shown in (II) of Fig. 6.1 (b). (b) RGB (red: resin, green: CF (CS), blue: inner ring in CF (CS)) color deconvoluted image. The two-way arrow is the polarization of X-ray beams. (c) Schematic illustration of the distribution of graphene sheets in CF. The blue and red two-way arrows are the thickness and plane directions of graphene sheets, respectively.

6.4 Conclusion

STXM studies of CFRP were performed to reveal the distributions of the chemical states in CFRP and evaluate STXM as a characterization technique for chemical imaging of CFRP. From the image stacks of C K-edge absorption, the presence of a coating layer between CF and resin was suggested on the basis of the spectral deconvolution analysis of the spectra. The inner and outer regions of CF (CS) exhibited the same chemical structure. Orientation of the π orbital of C=C in CF could be observed by horizontal linear polarized X-ray. STXM is a useful technique for the analysis of chemical state imaging of carbon-bearing multi composite materials, providing additional and crucial information regarding the enhancement mechanisms of tensile strength and elastic modulus of CFRP.

References

Ade, H., Zhang, X., Cameron, S., Costello, C., Kirz, J., Williams, S., Chemical contrast in X-ray microscopy and spatially resolved XANES spectroscopy of organic specimens, *Science*, 1992, **258**, 972.

Ade, H., Hsiao, B., X-ray Linear Dichroism Microscopy, *Science*, 1993, **262** 1427.

Hedrick, J. L., Yilgor, I., Jurek, M., Hedrick, J. C., Wilkes, G. L., McGrath, J. E., Chemical modification of matrix resin networks with engineering thermoplastics: 1. Synthesis, morphology, physical behaviour and toughening mechanisms of poly (arylene ether sulphone) modified epoxy networks, *Polymer*, 1991, **32**, 2020.

Hitchcock, A. P., 2009, http://unicorn.mcmaster.ca/aXis2000.html

Moffet, R. C., 2011, *LBNL Paper* LBNL-4245E

Sasaki, S., Nuclear instruments and methods in physics research section A: accelerators, spectrometers, detectors and associated equipment, *Nucl. Instrum. Methods Phys. Res., Sect. A* 1994, **331**, 763.

Takeichi, Y., Inami, N., Suga, H., Miyamoto, C., Ueno, T., Mase, K., Takahashi, Y., Ono, K., Design and performance of a compact scanning transmission X-ray microscope at the Photon Factory, *Rev. Sci. Instrum.*, 2016, **87,** 013704-1.

Tsuchiya, K., Shioya, T., Aoto, T., Harada, K., Obina, T., Sakamaki, M., Amemiya, K., Operation of a fast polarization-switching source at the Photon Factory, *J. Phys.: Conf. Ser.*, 2013, **425**, 132017.

Watts, B., Schuettfor, T., McNeill, C. R., Mapping of domain orientation and molecular order in polycrystalline semiconducting polymer films with soft X-ray microscopy, *Adv. Funct. Mater.*, 2011, **21**, 1122.

Chapter 7

Heterogeneous Chemical State of Carbon in Fe-C Binary Alloy

7.1 Introduction

With respect to the application type, the mechanical properties of steel products may vary. Depending on the various needs, types, and the number of additional elements, heat patterns during the heating and rolling processes are controlled accordingly (Bain *et al.*, 1961). Carbon is one of the most important elements to control the mechanical properties of steel; it exists in the steel microstructure as solid solution or segregation elements, carbides, and other types (Bain *et al.*, 1961). Although carbon in steel has been observed by the transmission electron microscopy-electron energy loss spectroscopy (TEM-EELS; Courtois *et al.*, 2006), the electron probe micro analyzer (Yamashita *et al.*, 2016), or the three-dimensional atom probe (Zhu *et al.*, 2009; Kobayashi *et al.*, 2015), there exist few studies focusing on the chemical state of carbon (e.g., chemical bond species and bond distance) in steel (Scott *et al.*, 2001; He *et al.*, 2006; Ninomiya *et al.*, 2017; Yoshimoto *et al.*, 2019). Furthermore, in electron microscopy, hydrocarbon molecules in the measurement chamber are adsorbed onto the sample surface as a result of electron beam irradiation, which causes contamination and makes it difficult to quantify and analyze the chemical structure of carbon in the samples. G. F. Bastin *et al.* (Bastin *et al.*, 1986) and W. Lengauer *et al.* (Lengauer *et al.*, 1997) reported that the distribution of oxygen gas can cleanse sample surfaces. In addition, it was difficult to evaluate the detailed chemical structure of carbide single phase by conventional X-ray absorption spectroscopy even if the excitation efficiency is better than that of electron beam. This is because it is difficult to synthesize carbide single phase and the spatial resolution of conventional X-ray absorption spectroscopy is not high enough to investigate carbide in steel microstructures.

Although the spatial resolution of X-ray absorption spectroscopy is approximately 10–50 times larger than that of electron microscopy, it enables the investigation of the chemical state more quantitatively than that of electrons, such as TEM-EELS (Seol *et al.*, 2010). In terms of the excitation efficiency from the ground level to the excited levels, X-rays are superior to electron beams for chemical state analysis (Smith, 1988). In addition,

the chemical structure mapping using X-ray absorption microscopy prefers diffraction measurements by electron microscopy to investigate the case of carbon partitioned from carbides and in a solid solution with no or low crystalline content. Another merit is that we can simultaneously obtain the information on the surface (a few to several nm) and bulk (probing depth is the thickness of the sample) of samples through different X-ray geometries: transmission and conversion electron yield (CEY) methods; this is especially important in metal specimens where the surface is easily oxidized and/or contaminated with carbon.

Therefore, in this study, we especially focused on scanning transmission X-ray microscopy (STXM). We obtained X-ray absorption images of the C K-edge by STXM to identify the lamellar microstructure of ferrite and θ-Fe$_3$C in perlite, with the intervals of approximately 100 nm. The sample in this study is one of the most suitable samples to evaluate the usefulness of chemical state mapping for carbon in steel by STXM because it consists of multi microstructure, such as grained carbides, lamellar microstructure of metal (low carbon solution), and carbide (including high carbon). We also performed two-dimensional chemical state mapping of carbon on the surface (a few to several nm) and in bulk (sample thickness of approximately 100 nm) in Fe‑C alloy using the transmission method and CEY method by STXM simultaneously, to clarify the effects of surface oxidation and/or contamination. It was revealed that the C K-edge spectra of the grained θ-Fe$_3$C are different from that of the lamellarθ-Fe$_3$C in the Fe‑C alloy. To consider the origin of this difference, the author performed first-principles calculations by assuming the distortion and anisotropy of the unit cell of the θ-Fe$_3$C structure, suggesting the anisotropy of the crystal structure of θ-Fe$_3$C and the lattice strain within lamellar θ-Fe$_3$C.

7.2 Experimental

The initial composition of our sample was Fe-1.48C-0.005Si-0.032Al-0.0008N (mass%); its final composition after heat treatment was similar to the initial composition. The sample was prepared by the vacuum melting method. As shown in Fig. 7.1, the sample was dissolved in N$_2$ atmosphere at atmospheric pressure, rolled to a size of 220 mm W $\times$ 100 mmL $\times$ 1.6 mm, heat-treated at 900 °C for 4 min, and water-cooled. Subsequently, the sample was further tempered at 400 °C for 10 min and cooled in the furnace; it has a pearlite microstructure, which is a lamellar microstructure composed of ferrite and θ-Fe$_3$C. Moreover, for TEM and STXM observations, a thin sample of approximately 10 μm $\times$ 10 μm $\times$ 100 nm was prepared by focused ion beam (FIB) processing, while the surface layer damaged by this processing was removed by argon milling. Finally, the sample thickness was adjusted to approximately 80 nm.
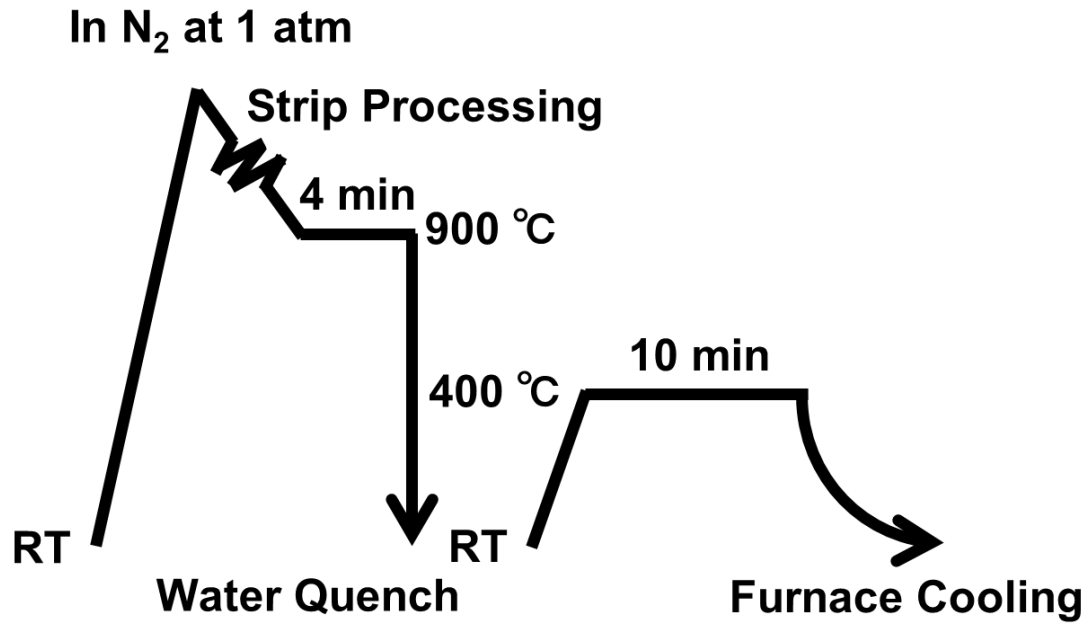
Figure 7.1 Heat pattern conditions of the sample.

To confirm the crystal structure of the generated crystal phases in the sample, we performed electron diffraction measurements using TEM at various sample positions, as shown in (a) to (d) in Fig. 7.2, in which, (a), (b), and (c) correspond to points at grained θ-Fe$_3$C, whereas (d) is a point at lamellar θ-Fe$_3$C. The electron beam diffraction patterns of the sample positions in Fig. 7.2 (a) to (d) are illustrated in Fig. 7.3 (a) to (d), respectively, which suggest that the crystal orientations along the normal direction of the surface of the thin film sample at points in Fig. 7.2 (a) to (d) are [513], [210], [$\bar{2}$12], and [011], respectively. The Euler angles (Φ, θ, Ψ) that reproduce each unit cell position at #1-4 in Fig. 7.2 are presented in Table 7.1, in which, Φ, θ, and Ψ indicate the rotation angles around the a, b, and c axes of the Cartesian coordinate in Fig. 7.3, respectively. It is noted that the θ/Φ directions were rotated by 5.0°/1.0°, 5.0°/1.0°, 5.0°/5.0°, and 8.0°/3.0° before measuring the diffraction pattern at each position (#1-#4) to obtain lower diffraction patterns of θ-Fe$_3$C, which is easier to determine the crystal orientation of θ-Fe$_3$C parallel to that of incident X-ray. The direction of lamination was not uniform, while the thickness of the thin film sample was approximately less than 100 nm. As described above, the grained particles in this sample consisted of θ-Fe$_3$C, and the constituents of the lamellar microstructure were confirmed to be ferrite and θ-Fe$_3$C.
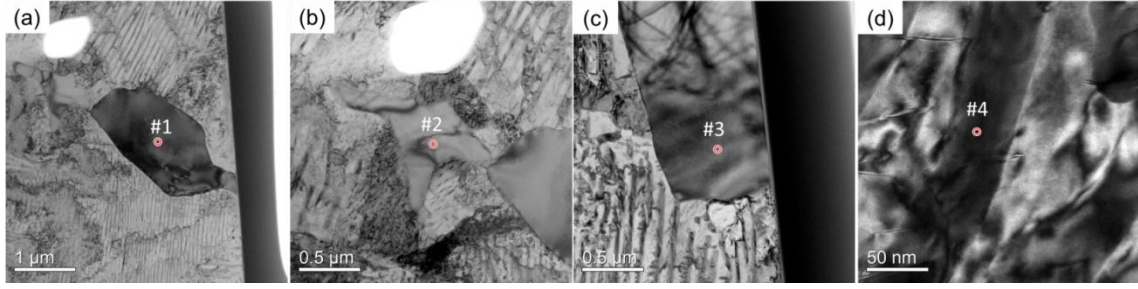
Figure 7.2 TEM images of (a), (b), and (c) grained θ-Fe$_3$C and (d) lamellar θ-Fe$_3$C in sample.
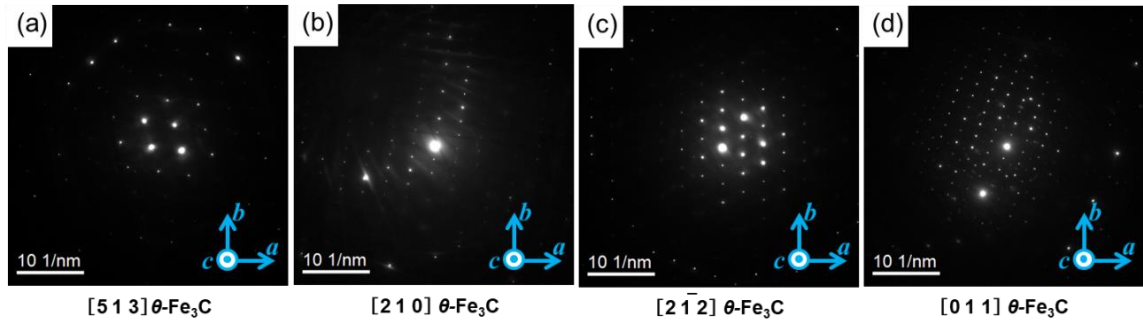
Figure 7.3 Electron diffraction images at points from #1-#4 in Fig. 7.2 (a) to (d). It is noted that the θ/Φ directions were rotated by 5°/1°, 5°/1°, 5°/5°, and 8°/3° before measuring the diffraction pattern at each position (#1-#4) to obtain lower diffraction patterns of θ-Fe$_3$C, which is easier to determine the crystal orientation of θ-Fe$_3$C parallel to that of incident X-ray.

Table 7.1. Euler angles (Φ, θ, Ψ) of θ-Fe$_3$C at each sample position (#1-4) in Fig. 7.2. The Cartesian coordinate system that serves as the reference for rotation is the coordinate system shown in Fig. 7.3.

	Φ (degree)	θ (degree)	Ψ (degree)
#1	-112	62.7	75.2
#2	-6.00	90.0	56.5
#3	-21.0	126	56.5
#4	-110	56.1	0.00

The STXM measurements were performed using a compact STXM (cSTXM (Takeichi *et al*., 2016)) at BL-13A, Photon Factory, KEK; it enabled us to obtain the X-ray absorption spectra by the transmission and CEY methods simultaneously with a spatial resolution of approximately 50 nm. A schematic of the optical system of the cSTXM is demonstrated in Fig. 2.4 in Chapter 2. The X-ray beam was focused at approximately

50 nm using the Fresnel zone plate (FZP). In the experiment, the inside of the measurement chamber had He atmosphere of 0.1 atm to maintain good thermal conductivity. The details of each measurement method (Stöhr, 1992) are described below. In the transmission method, the X-ray absorption ratios before and after the transmission of a thin sample were measured with a photomultiplier tube. The signal detected by the transmission method includes the information on the linear absorption coefficient and the thickness (X-ray transmission direction) of the sample. Assuming that the X-ray absorption intensities before and after the transmission are $I_0(E)$ and $I(E)$, respectively; their relationship is expressed as Eq. (7.1), where $\mu(E)$ is the linear absorption coefficient and t is the sample thickness. The energy dependence of the optical density (OD) was obtained as shown in Eq. (7.2), which is the product of the linear absorption coefficient and sample thickness. Note that $I_0(E)$ is the X-ray absorption intensity when they directly enter the detector without passing through the sample during measurement.

$$I(E) = I_0(E)e^{-\mu(E)t} \qquad (7.1)$$

$$OD \equiv \mu(E)t = \ln\frac{I_0(E)}{I(E)} \qquad (7.2)$$

On the other hand, the principle of the CEY method is based on the fact that the X-ray absorption intensity is proportional to the number of Auger electrons. When X-rays are irradiated on the sample, Auger electrons generated from the sample surface and secondary electrons that collide with Helium atoms in the cSTXM chamber were detected as the sample current from the order sorting aperture, which was installed upstream of the sample to pass only the first-order diffracted light by the FZP. The collision process of photoelectrons and Helium atoms, marked as * in Fig. 2.4, is a reaction expressed as in Eq. (7.3).

$$e^- + He \rightarrow He^+ + 2e^- \qquad (7.3)$$
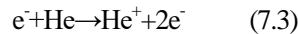
In addition to the transmission and CEY methods, the fluorescence yield (FY) approach measures characteristic X-ray intensities generated from the sample. In general, there exists a tradeoff between the fluorescence intensities and the number of Auger electrons. Light elements discharge more Auger electrons, whereas heavy elements effuse more fluorescence from a few hundred nanometers from the sample surface (Nielsen *et al.*, 2001). Therefore, the CEY method is more advantageous than the FY approach for carbon. During CEY-based measurements, electrons were detected by applying a voltage of 100 V. This method is sensitive to the surface state of the sample because the electrons that escape from the surface are within approximately 2–3 nm from the surface (Nielsen *et al.*, 2001). The signal intensity of CEY is proportional to the intensity ratio of X-ray $I_0(E)$ before irradiation and the detected current $i(E)$ after passing through the sample

and is expressed as Eq. (7.4).

$$\text{CEY int.} \equiv \frac{i(E)}{I_0(E)} \qquad (7.4)$$

The purpose of this study is to investigate the difference in the chemical structure of carbon depending on the morphology (bulk and lamellar) of the sample and compare the difference in chemical structure between the surface and bulk using the transmission and CEY methods. In this study, the spectra of the Fe L-edge and C K-edge transmission method, as well as the CEY approach were investigated. The dwell times for the Fe L-edge and C K-edge measurements were 10 ms and 50 ms, respectively.

To calculate the XAS spectrum, after structural optimization of θ-Fe$_3$C by density functional theory (DFT) calculations, the full-potential multiple scattering theory (FP-MST) computation was performed using the optimized structure. In the DFT calculation, in addition to the typical θ-Fe$_3$C (strain less), the XAS spectra of θ-Fe$_3$C with the b-axis extended by 1%, 5%, and 10% were also calculated to verify the effect of lattice strain, which were performed by the projector augmented wave (PAW) method using the Vienna Ab initio Simulation Package (VASP; Kresse *et al.*, 1996; Bloechl, 1994). The Generalized Gradient Approximation-Perdew, Burke & Ernzerh of (GGA-PBE; Perdew *et al.*, 1996) was used for the exchange-correlation potential, with the cutoff energy of the wave function being as 550 eV. For the reciprocal lattice points, the reciprocal lattice space was divided by the Monkhorst–Pack method (Monkhorst *et al.*, 1976) to obtain a $10 \times 10 \times 10$ mesh. The threshold for structural optimization was calculated when the force acting on each atom was below 0.01 eV / Å.

Based on the above structure, the XAS simulation spectrum is calculated by real space multiple scattering (RSMS). Because a substance is photo-excited in the spectroscopic process, information on the excited state F_f of the substance, as well as the ground state, is required. In the case of inner-shell excitation spectroscopy, during the X-ray absorption, the wavelength (energy) dependence of the X-ray absorption coefficient is observed by using the electric dipole approximation and the absorption coefficient μ (ω), which can be expressed by the following equation:

$$\mu(\omega) \propto \sum_f \left| \langle \Psi_f | \boldsymbol{\epsilon} \cdot \boldsymbol{r} | \Psi_i \rangle \right|^2 \delta\left(E_f - E_i - \hbar\omega\right) \qquad (7.5)$$

where, $|\Psi_i\rangle, E_i, |\Psi_f\rangle,$ and E_f are the ground state and its energy, as well as the excited state and its energy, respectively. ϵ is the X-ray polarization vector. $|\Psi_f\rangle$ includes a state function that covers the scattering process of photoelectrons in a solid, a screening effect of inner shell vacancies, and many-body effects such as

exchange-correlation potential. Therefore, using the optical potential Σ^{opt}, which depends on the energy of the photoelectrons, it can be described as follows:

$$[\nabla^2 + k^2 - V_{Hartree}]\Psi_f(r) = \int \Sigma^{opt}(r, r'; \hbar\omega)\Psi_f(r')dr' \qquad (7.6)$$

In this calculation, the optical potential of the atom was calculated using the one including the imaginary part of the Hedin–Lundqvist (HL) potential (Hedin *et al.*, 1965). Meanwhile, the ground state potential was generated from the superposition of the charge densities of each atom obtained from the HL potential. As for the excited state, the core Hall effect was introduced by transitioning the 1s inner shell electron to the unoccupied state and stabilizing only the Frozen-core approximation called valence state. The excited-state potential obtained by the Frozen-core approximation was self-consistently solved only in the atomic level category, and the overall potential was generated from the superposition of the charge densities of each atom obtained thereafter. Because the calculation method deals with distorted crystal systems, such as orthorhombic crystals, the FP-RSMS was especially employed, for which the FPMS package (Hatada *et al.*, 2007) was used. In this method, the potential can be defined in the entire region of the calculation system by dividing the region between the scattering sites by the Voronoi polyhedron. In addition, an empty cell (EC) was introduced to improve the calculation convergence. The radius of the scattering site was 1.4 Å for Fe, whereas 1.0 Å for both C and EC. The scattered waves at each scattering site were considered up to l = 4, and the cluster used for the calculation had a radius of 8 Å (approximately 300 atoms). These parameters were determined by confirming the convergence of the spectral shape. Moreover, the relative relationship of the energy axes of the calculated spectrum was calibrated by approximating the potential of the surface average to the vacuum level in all systems. As the lifetime of the C *K*-edge excitation process is 0.1 eV (FWHM; Krause *et al.*, 1979), all calculated spectra were also further broadened with the Lorentz function.

7.3 Results and discussion

The TEM image of one thin film sample is demonstrated in Fig. 7.4, in which, (a)‑(d) correspond to the areas of Fig. 7.2 (a)‑(d), respectively. On the other hand, the OD images at 280.0 eV (the energy before the absorption edge of the C *K*-edge) and 285.4 eV of the white dotted line area in Fig. 7.4 are illustrated in Fig. 7.5 (a) and (b), respectively. Meanwhile, the residual image obtained by subtracting Fig. 7.4 (a) from 7.5 (b) is shown in Fig. 7.5 (c). The images in Fig. 7.5 were measured at 30 nm / pixel. In Fig. 7.5 (a), a lamellar microstructure image was not observed, as confirmed in Fig. 7.4, whereas a clear pearlite lamellar structure can be detected in Fig. 7.5 (b), and the microstructure can be observed more clearly in Fig. 7.5 (c). Therefore, the

pearlite microstructure with an interval of approximately 100 nm could be identified by the OD contrast at the C

K-edge by STXM. This is the first observation of the Fe‑C alloy microstructure using X-ray microscopy within

nanometer scale. The contrast of the OD images was affected by the chemical structure of the element.

However, it is not sensitive to the crystal orientation and defects, which strongly affect the contrast of the TEM

images.

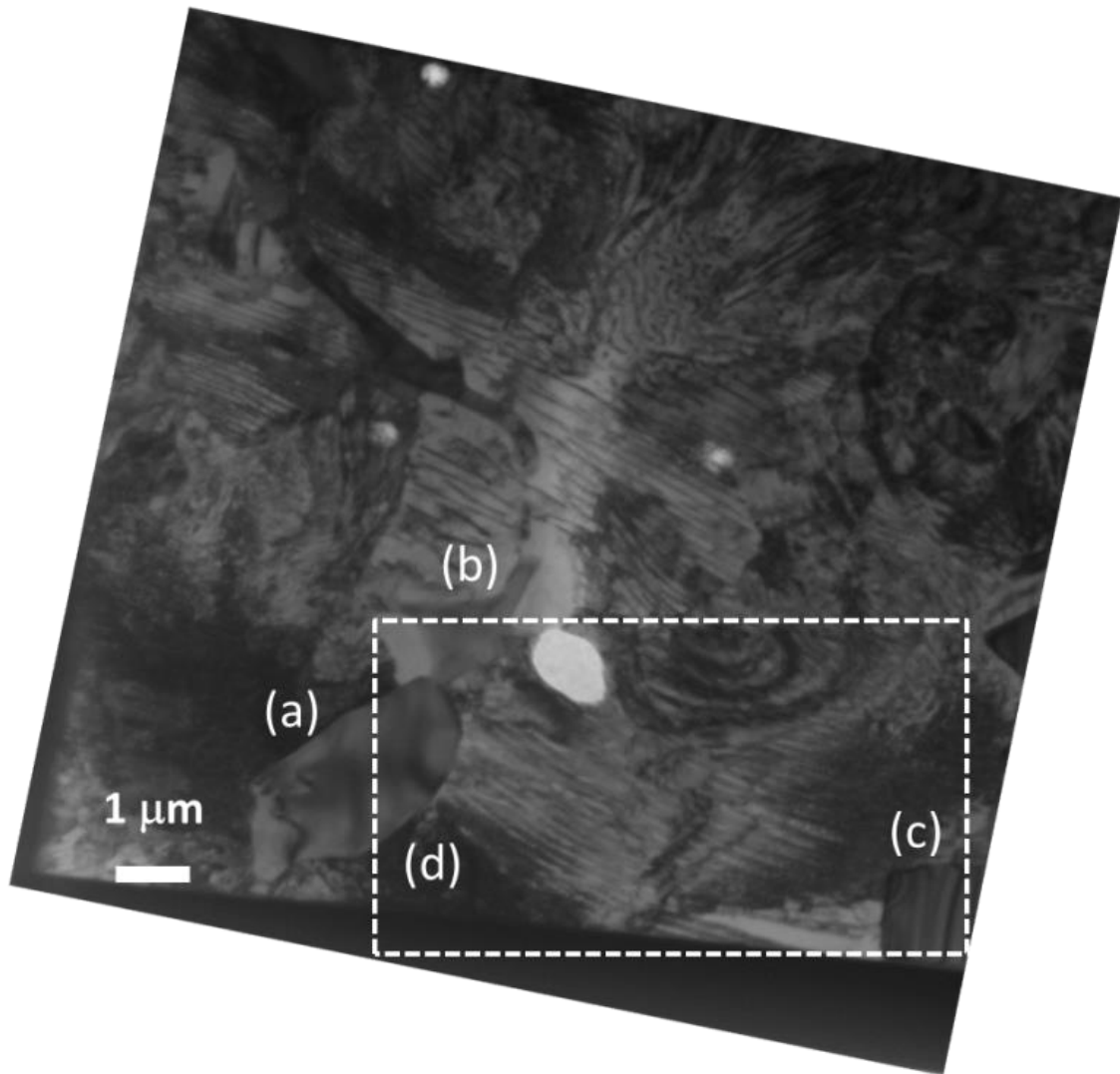**Figure 7.4** TEM image of the thin film sample. (a)-(d) correspond to areas of Fig. 7.2 (a)-(d), respectively. The
white dotted line is the observation area by STXM.
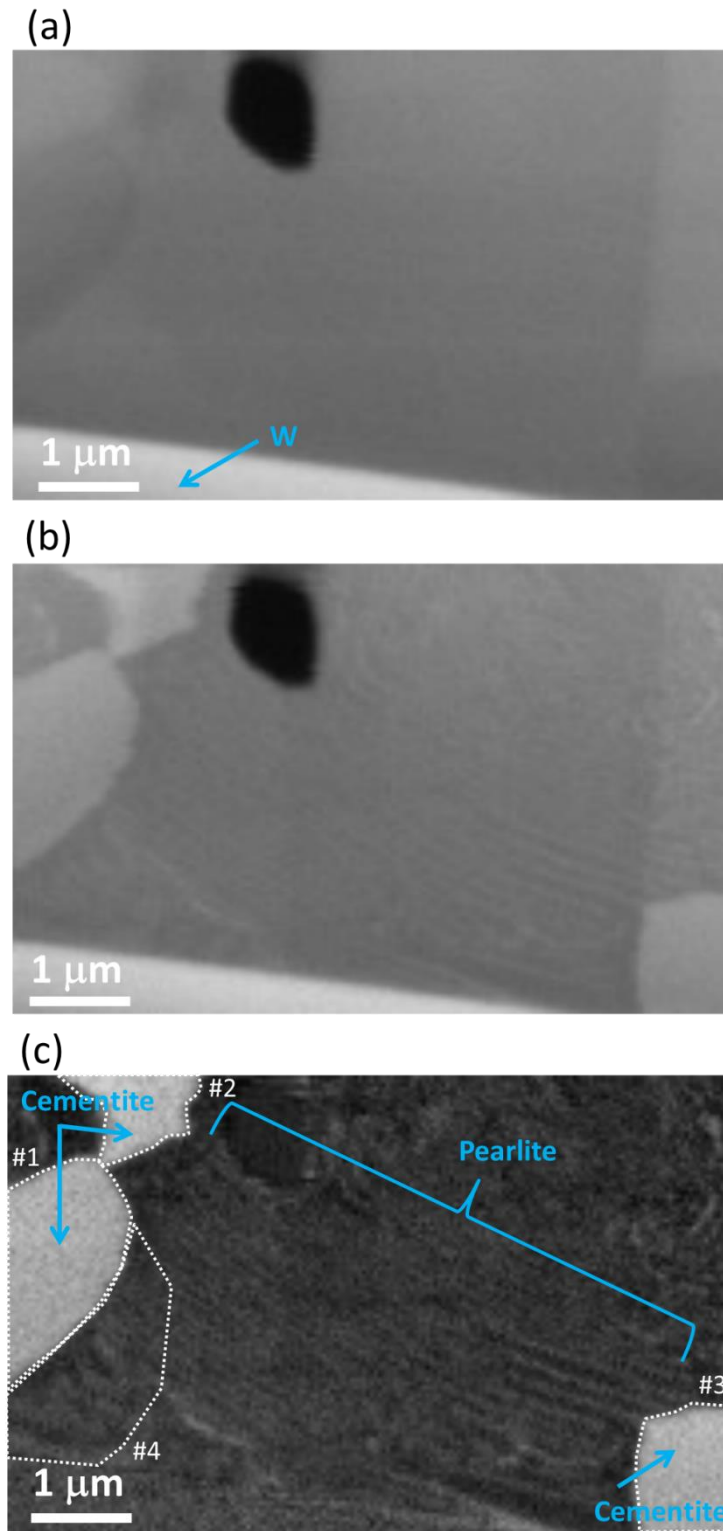
Figure 7.5 (a) X-ray absorption image at 280.0 eV (pre-edge), (b) X-ray absorption image at 285.4 eV, (c) the residual image between (a) and (b). (a) to (c) were measured at 30 nm/pixel. #1-#4 shows areas in Fig. 7.2 (a)-(d), respectively.

The X-ray absorption near edge spectroscopy (XANES) spectra of grained θ-Fe$_3$C and the pearlite microstructure measured by the transmission method, together with the surface measured by the CEY method are shown in Fig. 7.6. The C K-edge in areas around #1-4 in Fig. 7.5 (c) by the transmission mode and surface of the sample in the CEY mode are presented in Fig. 7.6 (a). These spectra were normalized at 288.2 eV. In the CEY spectrum, there are peaks (Moffet, 2011) originated from functional groups of hydrocarbons, such as alcohol (approximately 287.0 eV) and aldehyde (approximately 288.0 eV) groups. There exist no peaks originated from hydrocarbons and others; however, there were two broad peaks in the energy range of 283.0–290.0 eV. Similar spectral shape data of C K-edge absorption were also reported in EELS experiments (He *et al.*, 2006). Because the CEY spectrum of the pearlite area is almost the same as that of the grained θ-Fe$_3$C area, the C K-edge spectra of the surface demonstrate the average spectra of the entire surface of the thin film sample. The OD intensity ratios also varied between grained and lamellar θ-Fe$_3$C. In the following preliminary examination, in order to simplify the calculation, it was assumed that all contaminant layers were ethanol, and the density was the same as that of liquid (0.789 g/cm^3, 46.07 g/mol); the thickness of the contamination layer on the sample surface was assumed to be 1 nm. If the real thickness of the contamination layers is much thicker than 1 nm, the CEY spectra of Fe should not be detected, due to the probing depth of the CEY method, which is approximately a few nanometers (Nielsen *et al.*, 2001). The number of moles of the contamination layer per unit area (n_{con}) is $n_{con} = 0.789 \times 10^{-7}$ g/cm^2 = 0.171×10^{-8} mol/cm^2, whereas that of carbon atoms per unit area N_{con} contained in the contamination was $N_{con} = 0.514 \times 10^{15}$. In the same procedure for pearlite microstructure, the number of moles per unit area was $n_{sam} = 0.115 \times 0.430 \times 10^{-6}$ mol/cm^2 = 0.495×10^{-7} mol/cm^2, whereas that of carbon atoms in pearlite steel is $N_{sam} = 0.745 \times 10^{16}$ (the cementite fraction is 11.5%, which is the equilibrium state of the initial composition of the sample); the sample thickness was approximately 80 nm with density of 7.73 g/cm^3 and molar mass of 179.4 g/mol. The N_{sam}/N_{con} ratio > 14. We can consider that the carbon detected in perlite microstructure was almost originated from θ-Fe$_3$C, rather than ferrite, because the amount of carbon as solid solution element in ferrite in perlite was less than 0.01% of the mass in the equilibrium state of the initial sample composition. It can be concluded that the absorption spectrum of carbon obtained in the pearlite microstructure largely reflects carbon atoms not in the contamination layer but in the pearlite microstructure of the sample.

The Fe L-edge spectra in #1 and #4 in Fig. 7.5 (c) by the transmission mode and surface of the sample by the CEY mode are shown in Fig. 7.6 (b), which were normalized at 708.0 eV. Because the CEY spectrum of the pearlite area is almost the same as that of the grained θ-Fe$_3$C area, the Fe L-edge spectra of the surface also

demonstrate the average spectra of the entire surface of the thin film sample. As a preliminary examination for detailed discussion, the effects of surface oxidation and/or contamination were considered. Comparing the spectra of the pearlite area and the grained θ-Fe$_3$C area by the transmission method revealed that both ferrite and θ-Fe$_3$C exist in the spectrum of the pearlite area; hence, the spectrum of the perlite area has a shoulder on the higher energy side of the peaks approximately 708.0 eV and 723.0 eV, respectively. Despite some differences in how the tails are pulled, they are similar. There was almost no iron oxide in either spectrum. The peak intensity of 710.0 eV by the CEY method, which can obtain the information on the sample surface, is higher than that obtained by the transmission method. Therefore, it was found that the surface of the sample was oxidized; however, the influence of surface oxidation was negligible when we considered the spectra using the transmission method.
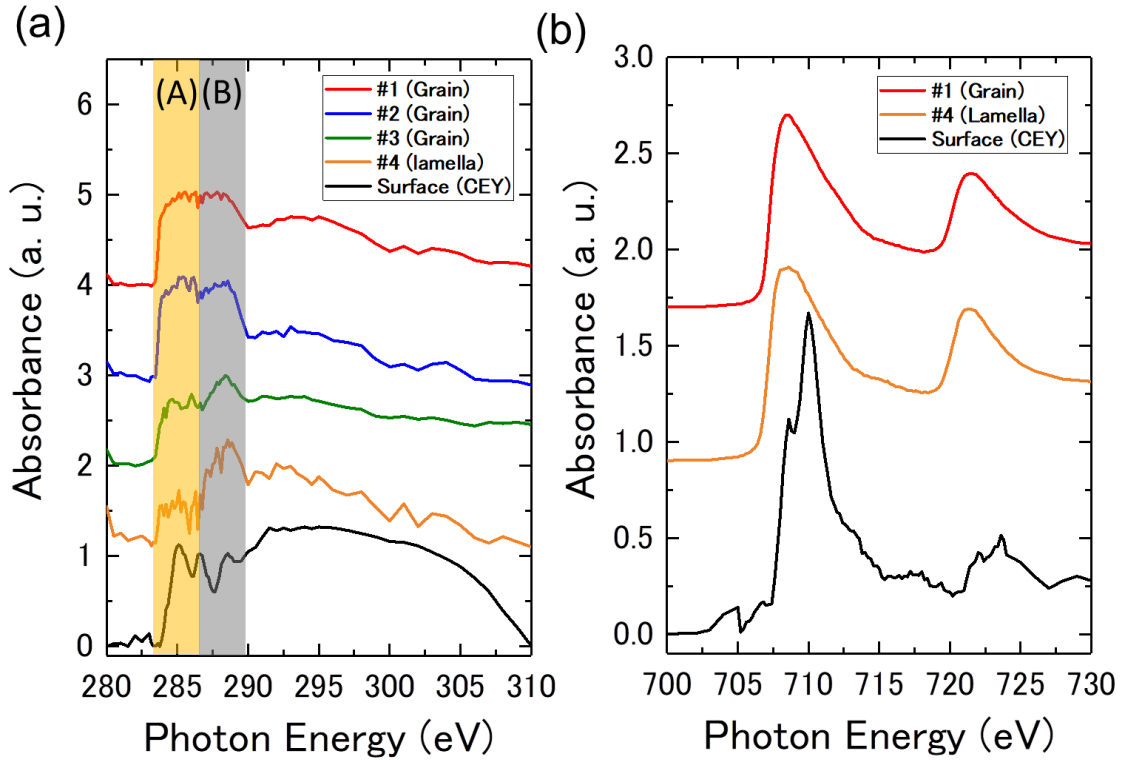
Figure 7.6 (a) C *K*-edge spectra in areas of #1-4 in Fig. 7.5 (c) by transmission mode and surface of sample by CEY mode, and (b) Fe *L*-edge in #1, #4 in Fig. 7.5 (c) by transmission mode and surface of thin film sample by CEY mode.

Moreover, the chemical structure of carbon in each microstructure (grain and lamellar θ-Fe$_3$C) in the Fe–C alloy was discussed. It can be observed easily that more than two types of chemical states exist in θ-Fe$_3$C: (A) *E*

= 283.0‑286.5 eV, and (b) E= 286.5‑289.0 eV, as shown in Fig. 7.6 (a). The ratios of these chemical states were found to be different between grained θ-Fe$_3$C and that of lamellar θ-Fe$_3$C in pearlite. In addition, a difference was observed between the C K-edge spectra of grained θ-Fe$_3$C and that of lamellar θ-Fe$_3$C in pearlite, which might have been originated from the microstructure and morphology of the θ-Fe$_3$C.

To confirm whether the C K-edge spectrum of the pearlite microstructure reflects the pearlite microstructure instead of the surface contamination, the amount of carbon on the surface contamination layer and the pearlite microstructure area were compared. Therefore, the difference between the spectra of the grained and lamellar θ-Fe$_3$C in Fig. 7.6 (a) could have been originated from the stress and defects generated during the formation of coarse grains of θ-Fe$_3$C and lamellar microstructure. Taniyama *et al.* (Taniyama *et al.*, 2017) and Kosaka *et al.* (Kosaka *et al.*, 2017) reported that θ-Fe$_3$C in pearlite was elastically distorted from a few to several percent in the b-axis direction.

Therefore, to determine the origins of the difference in the C K-edge spectrum of pearlite and bulk grained θ-Fe$_3$C, we performed first-principles calculations (projected augmented wave method, Vienna Ab initio Simulation Package, VASP) and multiple scattering calculations (full potential method, FPMS). The calculation conditions can be described as follows:

The author examined the cases where (1) the change ratio $\Delta b/b$ (Table 7.2) and (2) the assumption that each crystal plane shown in Fig. 7.7 was irradiated with X-rays. The former corresponds to the stress effect, whereas the latter corresponds to the evaluation of the crystal anisotropy of θ-Fe$_3$C. In these calculations, a and c of the lattice parameters were fixed.

Table 7.2 Lattice parameters and total energy for the first-principles calculation

$\Delta b/b$	0	0.01	0.05	0.1
a(Å)	5.036	5.036	5.036	5.036
b(Å)	6.725	6.791	7.060	7.396
c(Å)	4.480	4.480	4.480	4.480
Total energy (eV)	-135.344	-135.327	-134.977	-134.108
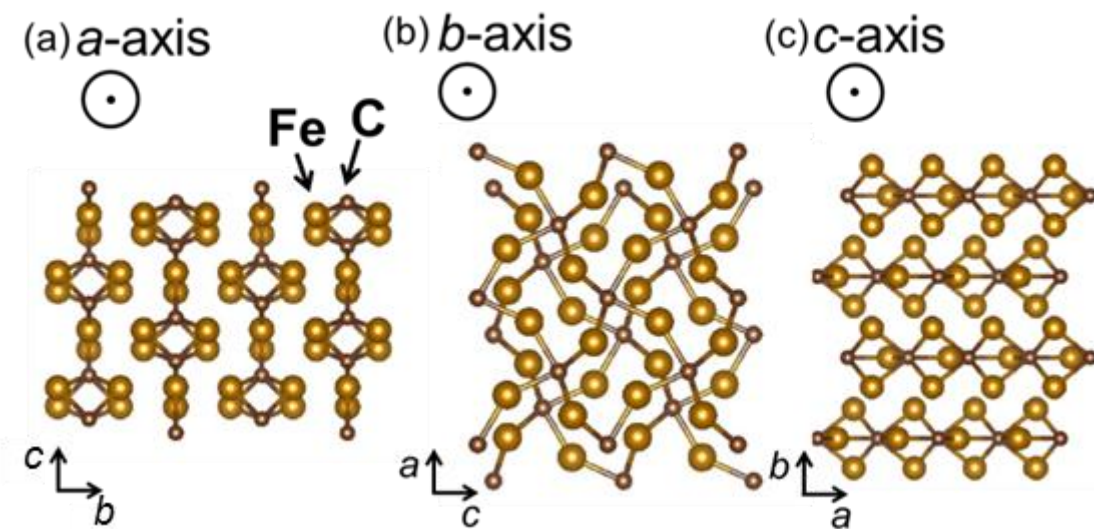
Figure 7.7 (a) Crystal structure of θ-Fe$_3$C as seen from *a*-axis, (b) *b*-axis, and (c) *c*-axis

First, the C *K*-edge spectra of θ-Fe$_3$C were calculated under the four stress conditions listed in Table 7.2. In these calculations, it was assumed that the calculated system was a single crystal and that unpolarized X-rays were irradiated. The results in Fig. 7.8 (a) demonstrate that the peak intensity of approximately 288.2 eV decreased with increasing $\Delta b/b$ change ratio. As shown in Fig. 7.6 (a), the crystal structure of θ-Fe$_3$C consists of stacking planes, including carbon atoms along the *b*-axis, which are located in a triangular prism composed of six iron atoms on each corner of the prism. The expansion of the *b*-axis was mainly attributed to the distance between the planes, rather than the increase in the triangular prism. Hence, it can be stated that the intensity of the sub peak of approximately 288.2 eV became smaller with the inter-surface distance increasing and that bonds related to carbons are located beyond the planes. In other words, it can be qualitatively understood that bonds between the planes are not only originated from the bonds of Fe‑Fe but also from those of C‑C or C‑Fe‑C. In addition, the intensity of XAS originated from C 1*s* is roughly proportional to the density of states in the unoccupied state of C 2*p*.

According to the calculated spectra, the sub-peak around 288.0 eV originated from C‑C and C‑Fe‑C bonds between planes perpendicular to *b*-axis are assumed to be weaker compared to the peak around 286.0 eV originated from Fe‑C bonds on the in-plane perpendicular to *b*-axis, representing the main peak. This is because the lattice parameters don't change without the lattice constant of *b*-axis (Fig. 7.7 (b)). Therefore, the bonds on the in-plane are not stronger than those on the planes and dominated by the metallic originated from Fe‑Fe. In addition, as a feature of Fe-C bond in this system, it is assumed that the bonds between Fe-C sheets

perpendicular *b*-axis are attributed to the peaks on the high energy side compared to the bonds in the sheet perpendicular *b*-axis and C 2*p* electrons might be more strongly bonded between the sheets than in the sheets. These features might cause the elastic anisotropy of θ-Fe$_3$C. However, the spectrum shape obtained in the experiment could not be reproduced by these calculations, because the peak intensity at 285.0 eV was no bigger than the peak intensity at 288.0 eV. As shown by Taniyama *et al.* (Taniyama *et al.*, 2017) and Kosaka *et al.* (Kosaka *et al.*, 2017), the $\Delta b/b$ ratio of θ-Fe$_3$C in pearlite increased. According to the calculation results, the peak at 288.0 eV of the grained perlite should be stronger. These calculation results are performed in the similar conditions in Y. Yoshimoto *et al.* (Yoshimoto *et al.*, 2019) and consistent with them.

Second, the C *K*-edge spectrum when assuming X-ray irradiation on each crystal plane is illustrated in Fig. 7.8 (b). In these calculations, it is assumed to be polarized X-rays along each axis, respectively. Regarding the influence of crystal anisotropy, it was found that the peak intensity of approximately 288.0 eV was sensitive, but the difference in the experimental results could not be reproduced. Thus, the observed difference in the chemical state (the shape of the C *K*-edge spectrum) of the pearlite microstructure and grained θ-Fe$_3$C cannot be explained by only stress or crystal anisotropy. In the future, the authoer will perform calculations that consider crystal defects and discuss the origins of the chemical state of θ-Fe$_3$C depending on the microstructure. From the Euler angles in Table 7.1, the coefficients to express each spectrum in each area in Fig. 7.2 (a)‑(d) can be considered as a linear combination of spectrum when irradiating X-rays parallel to each axial direction in Fig. 7.8 (b). These coefficients were calculated as follows: the basis vectors of the Cartesian coordinate system ((a 0 0), (0 b 0), (0 0 c)) in Fig. 7.3 (a) were rotated by Euler angles (Table 7.2) using Eq. (7.7), where a, b, c are lattice constants of θ-Fe$_3$C; the normalized coefficients for linear combination are normalized coefficients when (0 1 0) (the direction of linear polarization of X-ray) is expressed by the rotated vectors.

$$
\begin{pmatrix} \cos\Phi & -\sin\Phi & 0 \\ \sin\Phi & \cos\Phi & 0 \\ 0 & 0 & 1 \end{pmatrix} \begin{pmatrix} \cos\theta & 0 & \sin\theta \\ 0 & 1 & 0 \\ -\sin\theta & 0 & \cos\theta \end{pmatrix} \begin{pmatrix} 1 & 0 & 0 \\ 0 & \cos\Psi & -\sin\Psi \\ 0 & \sin\Psi & \cos\Psi \end{pmatrix}
$$

$$
= \begin{pmatrix} \cos\theta\cos\Psi & \sin\Phi\sin\theta\cos\Psi - \cos\Phi\sin\Psi & \cos\Phi\sin\theta\cos\Psi + \sin\Phi\sin\Psi \\ \cos\theta\sin\Psi & \sin\Phi\sin\theta\sin\Psi + \cos\Phi\cos\Psi & \cos\Phi\sin\theta\sin\Psi - \sin\Phi\cos\Psi \\ -\sin\theta & \sin\Phi\cos\theta & \cos\Phi\cos\theta \end{pmatrix} \quad (7.7)
$$

These normalized coefficients are presented in Table 7.3. The experimental spectra in Fig. 7.6 (a) and calculated spectra using these coefficients are illustrated in Fig. 7.9. Even considering the strain in the *b*-axis direction and the crystalline anisotropy of θ-Fe$_3$C, the C *K*-edge spectra of the experiment could not be reproduced by calculation. It is presumed that other factors, such as lattice defects cannot be considered in this calculation because the calculation results are consistent with the results of Y. Yoshimoto *et al.* (Yoshimoto *et al.*,

2019). Based on these experiments, it can be stated that the difference in the spectral shape indicates the chemical state of carbon variations due to the difference in the morphology of the same θ-Fe$_3$C; however, the origin of this difference still could not be clearly explained.

Based on these experiments, it can be stated that the difference in the spectral shape indicates the chemical state of carbon variations because of the difference in the morphology of the same θ-Fe$_3$C; however, the origin of this difference still could not be clearly explained. At least, the results of the experiments and calculations reported above might suggest as follows: there is a difference in the intensity ratio originated from Fe-C bonds of in-plane (at 286.0 eV) and out-of-plane (at 288.0 eV) parallel to the b-axis depended on the microstructures (grain and lamella). In other words, The Fe-C bonds of in-plane in lamellar microstructures are weaker than those in grains. In the process of microstructure formation, the distribution of the carbon local content varies depending on the morphology as known partitioning phenomena (Speer *et al.*, 2003), suggesting that the detailed crystal structure, such as site occupancies of carbon, might vary. In this study, only one field of view was observed for the lamellar microstructure, so in the future, the number of observed fields of view will be increased to verify the above.

Table 7.3 Normalized coefficients of unit cell vectors after Euler angles rotation to express the unit vector of b-axis (010) (parallel to the electric vector of X-ray).

	C_a (a-axis)	C_b (b-axis)	C_c (c-axis)
#1	0.87	0.31	0.38
#2	0.89	0.44	0.13
#3	0.91	0.26	0.33
#4	0.50	0.24	0.83

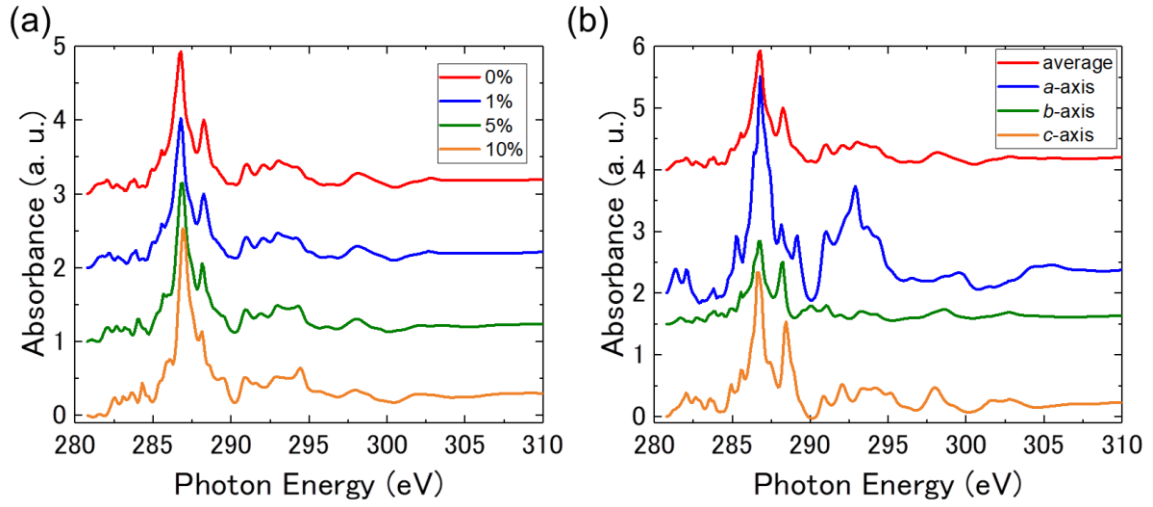**Figure 7.8** (a) C *K*-edge spectra of *θ*-Fe₃C when *Δb/b* ratio changes by +0, 1, 5, and 10%; (b) C *K*-edge spectra assuming that X-ray irradiates from each direction of (a) to (c) in Fig. 7.7. In the calculations (a) and (b), it is assumed to be unpolarized X-ray and polarized X-rays along each axis, respectively.
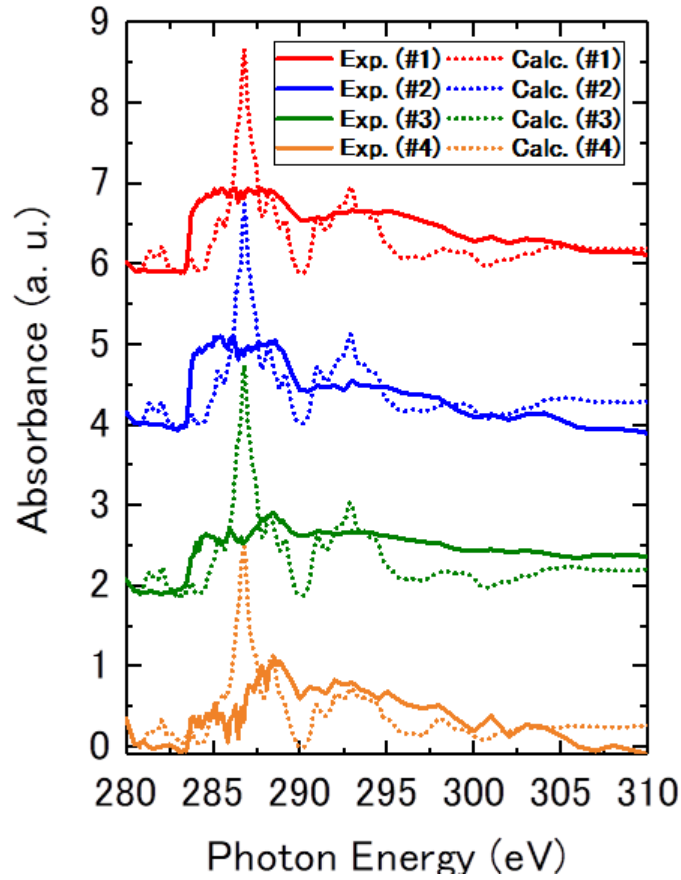

Figure 7.9 (a) C *K*-edge spectra of *θ*-Fe₃C when *Δb/b* ratio changes by +0, 1, 5, and 10%; (b) C *K*-edge spectra assuming that X-ray irradiates from each direction of (a) to (c) inm Fig. 7.7.

7.4 Conclusion

To investigate the chemical state of an additional element, that is, carbon in steel, we first verified whether the microstructure of steel could be identified using STXM. We successfully identified grained θ-Fe$_3$C and pearlite structures (lamellar spacing of approximately 100 nm) in Fe–C alloy using C K-edge absorption. In addition, the possibility of the extraction of the XANES spectrum of a specific element at a specific location with a spatial resolution of approximately 50 nm by STXM was confirmed.

Moreover, to compare (1) the difference in the average information on the surface and bulk, as well as (2) the difference in the chemical state of the carbon in θ-Fe$_3$C depending on morphology (grains and lamellar), the author applied the transmission and CEY methods simultaneously to perform two-dimensional chemical state mapping of the surface (thickness direction to a few nm) and bulk (thickness direction to approximately 80 nm) in Fe–C alloy. A clear difference was found between the chemical states of carbon of the grained θ-Fe$_3$C and pearlite microstructures of Fe-C alloy. It was found that the spectra obtained by the transmission method originated from carbon in the sample.

Finally, to examine the origin of this difference, we performed first-principles calculations by considering the stress in the b-axis direction and crystal anisotropy, which could not reproduce the experimental spectra based on crystal structure models that have been reported. In the future, the author will perform calculations that consider not only the strain and crystal anisotropy, but also other factors (e. g. the detailed crystal structure, such as site occupancies of carbon), and consider the origins of the difference in the chemical state of carbon in θ-Fe$_3$C depending on the microstructure.

In terms of the development of the STXM instrument, the air exposure system enables us to reduce the contamination of the sample to investigate a lower amount of carbon as a solid solution element in materials such as ferrite and martensite. Using this system, the author could be able to study the relationship between the distribution of composition and the chemical state of carbon, as well as that of the strain in the grain of θ-Fe$_3$C. This cannot be achieved by conventional techniques such as TEM. Generally, the spatial distributions of the elements and microstructures were mainly investigated by ATP and TEM. However, when it was essential to consider carbides, which do not possess a crystal structure that melted during the heat treatment or the chemical bond between Fe and carbon at the grain boundary the investigations of the conventional microstructure and crystal structure were not enough to identify the essential role of carbon in their mechanical properties. Therefore, it was important to analyze the chemical states of carbon in steel (one of the structural materials) on a

nanoscale, which was general for functional materials. Regarding the analysis of the chemical structure, the same discussion could be applied to other additive elements in steel.

References

Bain E. C., Paxton, H. W., *Alloying Elements in Steels, 2nd edition*, 1961.

Bastin, G. F., Heijlgers, H. J. M., *X-ray Spectrometry*, 1986, **15**, 135.

Bloechl, P., Projector augmented-wave method, *Phys. Rev. B*, 1994, **50**, 17953.

Courtois, E., Epicier, T., Scott, C., EELS study of niobium carbo-nitride nano-precipitates in ferrite, *Micron*, 2006, **37**, 492.

Hatada, K., Hayakawa, K., Benfatto, M., Natoli, C. R., Full-potential multiple scattering for x-ray spectroscopies, *Phys. Rev. B.*, 2007, **76**, 060102(R).

He, K., Brown, A., Brydson, R., Edmonds, D. V., Analytical electron microscope study of the dissolution of the Fe_3C iron carbide phase (cementite) during a graphitisation anneal of carbon steel, *J. Mater. Sci.*, 2006, **41**, 5235.

Hedin, L., New method for calculating the one-particle green's function with application to the electron-gas problem, *Phys. Rev.*, 1965, **139**, A796.

Kobayashi, Y., Takahashi, J., Kawakami, K., CAMP-ISIJ, 2015, **28**, 307.

Kosaka, M., 2017, the 175th ISIJ meeting.

Krause, M. O., Oliver, J. H., Natural widths of atomic K and L levels, *K*α X-ray lines and several *KLL* Auger lines, *J. Phys. Chem. Ref Data*, 1979, **8**, 329.

Kresse, G. and Furthmueller, J., Efficiency of ab-initio total energy calculations for metals and semiconductors using a plane-wave basis set, *Comput. Mater. Sci.*, 1996, **6**, 15.

Lengauer, W., Bauer, J., Bohn, M., Wiesenberger, H., Ettmayer, P., Electron-probe microanalysis of light elements in multiphase diffusion couples, *Microchim. Acta*, 1997, **126**, 279.

Monkhorst, H. J. and Pack, J. D., Special points for Brillouni-zone integrations, *Phys. Rev. B*,1976, **13**, 5188.

Nielsen, J. A., McMorrow, D., *Elements of Modern X-ray Physics, 2nd Edition*, 2001.

Perdew, J. P., Burke, K., Ernzerhof, M., Generalized gradient approximation made simple, *Phys. Rev. Lett.*, 1996, **77,** 3865.

Moffet, R. C., LBNL Paper LBNL-4245E, 2011.

Momma, K., Izumi, F., VESTA 3 for three-dimensional visualization of crystal, volumetric and morphology data, *J. Appl. Crystallogr.*, 2011, **44**, 1272.

Ninomiya, K., Kamitani, K., Tamenori, Y., Tsuruta, K., Okajima, T., Yoshimura, D., Sawada, H., Kinoshita, K., Nishibori, M., 軟 X 線吸収分光法によるフェライト鋼中微量固溶炭素の化学状態観察, *Tetsu-to-Hagané*, 2017, **104(11)**, 628.

Scott, A. J., Brydson, R., M. MacKenzie, Craven, A. J., Theoretical investigation of the ELNES of transition metal carbides for the extraction of structural and bonding information, *Phys. Rev. B*, 2001, **63**, 245105.

Seol, J. B., Gu, G. H., Lim, N. S., Das, S., Park, C. G., Atomic scale investigation on the distribution of boron in medium carbon steels by atom probe tomography and EELS, *Ultramicroscopy*, 2010, **110(7)**, 783.

Smith, N. V., Inverse photoemission, *Rep. Prog. Phys.*, 1988, **51**, 1227.

Speer, J., Matlock, D. K., De Cooman, B. C., Schroth, J. G., Carbon partitioning into austenite after martensite transformation, *Acta Materialia*, 2003, 51(9), 2611.

Stöhr, J., *NEXAFS Spectroscopy*, 1992.

Takeichi, Y., Inami, N., Suga, H., Miyamoto, C., Ueno, T., Mase, K., Takahashi, Y., Ono, K., Design and performance of a compact scanning transmission X-ray microscope at the Photon Factory, *Rev. Sci. Instrum.,* 2016, **87,** 013704-1.

Taniyama, A., Takayama, T., Arai, M., Hamada, T., Deformation behavior of cementite in deformed high carbon steel observed by X-ray diffraction with synchrotron radiation, *Metall and Mat Trans A*, 2017, **48**, 4821.

Yamashita, T., Tanaka, Y., Nagoshi, M., Ishida, K., Novel technique to suppress hydrocarbon contamination for high accuracy determination of carbon content in steel by FE-EPMA, *Sci. Rep.*, 2016, **6**, 29825.

Yoshimoto, Y., Yonemura, M., Takakura, S., Nakatake, M., The bonding characteristics and local structure of carbon in solution and iron carbides in iron using C *K*-edge X-ray absorption spectroscopy measurement and first-principle calculation, *Metallurgical and Materials Transactions*, 2019, **50(9)**, 4435.

Zhu, C., Cerezo, A., W.Smith, G. D., Carbide characterization in low-temperature tempered steels, *Ultramicroscopy*, 2009, **109**, 545.

Chapter 8

Summary and Future Prospects

In the preceding chapters, the chemical structures of carbon in carbon composite materials (PAN- and pitch-based CFs and CFRP) and a Fe–C alloy studied by STXM with linear polarized X-ray and azimuthal sample rotation were described. To reveal the relationship between the spatial distribution of the chemical structure in the microstructure and the macroscopic mechanical properties, STXM, which was suitable for the chemical structure analysis on the nanometer scale, was employed, and methodologies to evaluate the distribution of the π-orbital orientation and stress between the π-orbital–oriented domains in the materials were developed. Additionally, the chemical state analysis of carbon was investigated by complementarily employing STXM and the first-principles calculation. It was confirmed that the findings of this study will elucidate the relationship between the orientation distribution and mechanical properties of carbon materials described in 1.2 and the relationship between the chemical structure and mechanical properties of carbon in the steel.

In Chapter 2, the experimental methods, namely the principles of XAS and STXM were described. The details of the experimental method, including the characteristics of the beamline of the synchrotron radiation facility, will be explained. Additionally, the author will explain the analytical methods (XRD and TEM) and the principle of the first-principles calculations that are complementarily employed in STXM.

In Chapter 3, to reveal the difference in the π-orbital–oriented domain structure due to the raw materials of CFs, the author performed the carbon chemical-structure mapping on the cross and longitudinal sections of PAN- and pitch-based CFs using by STXM and two orthogonal linearly polarized X-rays. The results indicated that the distribution of the π-orbital–oriented domains in CFs varied considerably depending on the raw material. Contrarily, no difference in the distribution of the σ-orbital orientations between the PAN- and pitch-based CFs was observed. Regarding the PAN-based CFs, the graphene sheet structure was distributed along the fiber-axis direction, and the cross-section consisted of randomly distributed domains with sizes that were ≤ 50 nm as reported in a previous study (Chapter 6). Conversely, the pitch-based CFs were composed of aggregates of the

graphite domains with the π-orbital–oriented domains in the cross-sections ranging from 100 nm to 1 μm. It was confirmed that these domains were striped-shaped with a width of 200–300 nm along the CF axis (the longitudinal section). The size and distribution of the π-orbital–oriented domains with the crystallite sizes may be the determining factors of the mechanical properties of CFs. The utilization of STXM availed information on the chemical structures of the various molecules. Particularly, STXM would be indispensable in clarifying and proposing design guidelines for other highly functional materials where the chemical structures, such as the π-orbital–oriented domains, are closely related to the macroscopic properties.

In Chapter 4, to visualize the π-orbital–oriented domains whose distribution was one the most important factors in determining the unique microstructures of CFs that are deeply related with macroscopic mechanical properties, Two-dimensional orbital orientation mapping was developed by employing STXM and the azimuthal sample rotation and successfully visualized the distribution in commercial pitch-based CFs with a spatial resolution on the nm scale. The specific procedure the author developed is as follows: the X-ray absorption images whose contrast of π^*/σ^* were obtained at six rotation angles via STXM measurements and calculated the average orientation angle, θ_{ori}, of the position of each sample in the images was calculated through employing the theoretical relationship between the direction of the orbital and that of the X-ray polarization vector. The π-orbital domains, which are 100 times larger than the size of the crystals of graphite, were visualized quantitatively, and the results suggested that each domain consisted of a few crystallites. To characterize two-dimensional continuous π-orbital orientation distributions in CFs, it is necessary to evaluate the orientation image with the specific criteria. By recognizing the pixels as in the same domain when the orientation angle difference between adjacent pixels was below a certain threshold, the domain distributions were visualized based on the criteria at various thresholds. It was suggested that the boundaries with a large strain were distributed in the outer peripheral portion compared to the inside of CF.

In Chapter 5, to reduce the slip in the rotating axis during sample rotation in STXM measurements and to improve the backlash or errors in rotation, an azimuthal rotation sample holder was developed with a cross roller bearing for the STXM system. The holder improved the accuracy of the rotation angle and deflection of the surface of the disk plate compared to previous systems with the brass bevel gears and conventional ball bearings. To evaluate the performance of the holder, the π-orbital orientation domains in the carbon materials were investigated. The average orientation angle in each of the sub-μm π-orbital–oriented domains of natural spheroidal graphite was determined based on the dependence of the π^*/σ^* ratio on the polarization angles of X-ray employing the sample rotation and two orthogonal polarization angles.

In Chapter 6, to determine if it applied to the observation of the boundary of different materials in CFRP and reveal the distributions of the chemical states in CFRP, the author performed an X-ray absorption mapping near the C K-edge. From the images obtained, the presence of a coating layer between CF and the resin was suggested because of the spectral deconvolution analysis of the spectra. The inner region of CF (the cross-section) possessed the same chemical structure as its outer region. The orientation of the π orbital of C=C in CF could be observed by linear polarized X-rays. STXM is a beneficial technique for the analysis of the chemical-state imaging of carbon-bearing multicomposite materials that affords additional and essential information regarding the enhancement mechanisms of the tensile strength and elastic modulus of CFRP.

In Chapter 7, to investigate the chemical structure of carbon, which is one of the most essential additives in steel, the author performed X-ray absorption mapping near the C K-edge and Fe L-edge in two measurement modes (transmission (bulk) and CFY (surface-sensitive) modes). The author successfully identified grained θ–Fe_3C and a pearlite structure (with a lamellar spacing of ~100 nm) in the Fe–C alloy. To compare (1) the differences in the average information on the surface and bulk and (2) in the chemical state of carbon in θ–Fe_3C depending on the morphology (grains and lamellar), the author applied the transmission and CEY methods simultaneously to perform a two-dimensional chemical-state mapping of the bulk and surface of the Fe–C alloy. In the grained θ–Fe_3C and pearlite microstructure of the Fe–C alloy, a clear difference existed between their spectra. It was found that the spectra obtained by the transmission method originated from the carbon in the sample. Furthermore, it was clarified that the C K-edge spectrum of the grained θ–Fe_3C was different from that of lamellar θ–Fe_3C of the pearlite. Finally, to examine the source of this difference, we performed first-principles calculations by considering the stress in the b-axis direction and crystal anisotropy. The calculations could not reproduce the experimental spectra.

As mentioned in Chapter 1, it has been known that the heterogeneity of the chemical state can determine the mechanical properties of structural materials. Structural materials exhibit a multiscale hierarchy. The mechanical properties of structural materials can be understood considering not only in single crystals or single phases but also in hierarchical microstructures and their heterogeneity. Moreover, observations with a high special resolution have shown that the analytical results from the microstructures and chemical structures are different, and in such a case, the chemical structures will be essential in understanding their mechanical properties.

Summarily, this study has afforded new insights and methodologies for understanding the relationship between the distribution of the chemical structure and the macroscopic mechanical properties of structural

materials. For the future aspect, more detailed researches are expected to fully elucidate the origin of the mechanical properties of structural materials. As described in Section 1.1, it is essential to perform the various analyses on a multiscale probe to understand the mechanical properties and destruction of structural materials.

In this study, the author focused on STXM, which is the most suitable method for observing carbon, as an analytical technique to obtain the information mentioned above. The author believes that it can contribute to a comprehensive understanding of structural materials by combining it with X-CT (X-ray computed tomography) and XAFS-CT (X-ray absorption fine structure-computed tomography) (Takeichi *et al*,, 2018), which enable in-situ observation of the chemical states of additional elements in steel.

Reference

Takeichi, Y., Watanabe, T., Niwa, Y., Kitaoka, S., Kimura, M., 3D Spectromicroscopic Observation of Yb-Silicate Ceramics Using XAFS-CT, *Microsc. Microanal.*, 2018, **24 (Suppl 2)**, 484.

Appendix A. List of Publications and Presentations

(I) Original papers

This present thesis is based on the works contained in following (3), (4), and (5);

[1ˢᵗ author]

(1) T. Harano, Y. Nemoto, R. Murao, and M. Kimura, "Accuracy improvement of the XRD-Rietveld method for the quantification of crystalline phases in iron sintered ores through the correction of micro-absorption effects" *Tetsu-to-Hagané* **107(3)**, 210-2018 (2021) (in Japanese)
(原野貴幸, 根本侑, 村尾玲子, 木村正雄, "XRD-Rietveld 法による焼結鉱中結晶相の定量におけるマイクロアブソープション効果の検証とその補正法の提案" *鉄と鋼* **107(3)**, 210-218 (2021).)

(2) T. Harano, Y. Nemoto, R. Murao, and M. Kimura, "Accuracy improvement of the XRD-Rietveld method for the quantification of crystalline phases in iron sintered ores through the correction of micro-absorption effects" *ISIJ Int.* **60**, 2851-2858 (2020).

(3) T. Harano, Y. Takeichi, T. Ohigashi, D. Shindo, E. Nemoto, D. Wakabayashi, S. Yamashita, R. Murao, and M. Kimura, "Azimuthal-rotation sample holder for molecular orientation analysis" *J. Synchrotron Radiat.* **27**, 1167-1171 (2020).

(4) T. Harano, Y. Takeichi, M. Usui, Y Arai, R. Murao, N. Negi, and M. Kimura, "Observation of distribution of π-orbital-oriented domains in PAN- and pitch-based carbon fibers using scanning transmission X-ray microscopy" *Appl. Sci.* **10(14)**, 4836 (2020).

(5) T. Harano, R. Murao, Y. Takeichi, M. Kimura, and Y. Takahashi, "Observation of the Interface between

Resin and Carbon Fiber by Scanning Transmission X-ray Microscopy" *J. Phys.: Conf. Ser.* **849**, 012023 (2017) .

(6) <u>T. Harano</u>, G. Shibata, K. Yoshimatsu, K. Ishigami, V.K. Verma, Y. Takahashi, T. Kadono, T. Yoshida, A. Fujimori, T. Koide, F.-H. Chang, H.-J. Lin, D.-J. Huang, C.-T. Chen, P.-H. Xiang, H. Yamada, and A. Sawa, "Phase diagramof $Ca_{1-x}Ce_xMnO_3$ thin films studied by X-ray magnetic circular dichroism" *Sol. Sta. Commun.* **207**, 50 (2015).

(7) <u>T. Harano</u>, G. Shibata, K. Ishigami, Y. Takahashi, V. K. Verma, V. R. Singh, T. Kadono, A. Fujimori, Y. Takeda, T. Okane, Y. Saitoh, H. Yamagami, T. Koide, H. Yamada, A. Sawa, M. Kawasaki, Y. Tokura, and A. Tanaka, "Role of doped Ru in coercivity-enhanced $La_{0.6}Sr_{0.4}MnO_3$ thin film studied by x-ray magnetic circular dichroism" *Appl. Phys. Lett.* **102**, 222404 (2013).

[2nd author-]

(1) R. Murao, <u>T. Harano</u>, I. -H. Jung, and M. Kimura, "Thermodynamic modeling of the SFCA phase $Ca_2(Fe,Ca)_6(Fe,Al,Si)_6O_{20}$", *Tetsu-to-Hagané* **105(5)**, 493-501 (2019). (in Japanses)
(村尾玲子, <u>原野貴幸</u>, 木村正雄, In-Ho Jung, "SFCA 相 $Ca_2(Fe, Ca)_6(Fe, Al, Si)_6O_{20}$ の熱力学モデルの構築" *鉄と鋼* **105(5)**, 493-501 (2019).)

(2) G. Shibata, K. Yoshimatsu, K. Ishigami, <u>T. Harano</u>, Y. Takahashi, S. Sakamoto, Y. Nonaka, T. Kadono, M. Furuse, S. Fuchino, M. Okano, J.-i. Fujihira, A. Uchida, K. Watanabe, H. Fujihira, S. Fujihira, A. Tanaka, H. Kumigashira, T. Koide, and A. Fujimori, "Anisotropic Charge Distribution Induced by Spin Polarization in $La_{0.6}Sr_{0.4}MnO_3$ Thin Films Studied by X-ray Magnetic Linear Dichroism", *J. Phys. Soc. Jpn.* **87**, 114713 (2018).

(3) G. Shibata, M. Kitamura, M. Minohara, K. Yoshimatsu, T. Kadono, K. Ishigami, <u>T. Harano</u>, Y. Takahashi, S. Sakamoto, Y. Nonaka, K. Ikeda, Z Chi, M. Furuse, S. Fuchino, M. Okano, J. Fujihira, A. Uchida, K. Watanabe, H. Fujihira, S. Fujihira, A. Tanaka, H. Kumigashira, T. Koide, and A. Fujimori, "Anisotropic spin-density distribution and magnetic anisotropy of strained $La_{1-x}Sr_xMnO3$ thin films: Angle-dependent x-ray

magnetic circular dichroism", *npj Quantum Materials* **3**, 3 (2018).

(4) R. Murao, T. Harano, M. Kimura, and I. -H. Jung, "Thermodynamic modeling of the SFCA phase $Ca_2(Fe,Ca)_6(Fe,Al,Si)_6O_{20}$" ISIJ int. **58(2)**, 259 (2018).

(5) K. Ishigami, K. Yoshimatsu, D. Toyota, M. Takizawa, T. Yoshida, G. Shibata, T. Harano, Y. Takahashi, T. Kadono, V. K. Verma, V. R. Singh, Y. Takeda, T. Okane, Y. Saitoh, H. Yamagami, T. Koide, M. Oshima, H. Kumigashira, and A. Fujimori, "Thickness-dependent magnetic properties and strain-induced orbital magnetic moment in $SrRuO_3$ thin films" *Phys. Rev. B* **92**, 064402 (2015).

(6) Y. Takahashi, V. K. Verma, G. Shibata, T. Harano, K. Ishigami, K. Yoshimatsu, T. Kadono, A. Fujimori, A. Tanaka, F. -H. Chang, H. -J. Lin, D. J. Huang, C. T. Chen, B. Pal, and D. D. Sarma, "Observation of magnetically hard grain boundaries in double-perovskite Sr_2FeMoO_6" *Europhys. Lett.* **108**, 27003 (2014).

(7) Y. Takahashi, T. Kadono, V. R. Singh, V. K. Verma, K. Ishigami, G. Shibata, T. Harano, A. Fujimori, Y. Takeda, T. Okane, Y. Saitoh, H. Yamagami, S. Yamamoto, and M. Takano, "Orbital magnetic moment and coercivity of SiO_2-coated FePt nanoparticles studied by x-ray magnetic circular dichroism" *Phys. Rev. B* **90**, 024423 (2014).

(8) G. Shibata, K. Yoshimatsu, E. Sakai, V. R. Singh, V. K. Verma, K. Ishigami, T. Harano, T. Kadono, Y. Takeda, T. Okane, Y. Saitoh, H. Yamagami, A. Sawa, H. Kumigashira, M. Oshima, T. Koide, and A. Fujimori, "Thickness-dependent ferromagnetic metal to paramagnetic insulator transition in $La_{0.6}Sr_{0.4}MnO3$ thin films studied by x-ray magnetic circular dichroism" *Phys. Rev. B* **89**, 235123 (2014).

(9) V. K. Verma, V. R. Singh, K. Ishigami, G. Shibata, T. Harano, T. Kadono, A. Fujimori, F.-H. Chang, H. -J. Lin, D. -J. Huang, C. T. Chen, Y. Zhang, J. Liu, Y.H. Lin, C-W. Nan, and A. Tanaka, "Origin of enhanced magnetoelectric coupling in $NiFe_2O_4$/$BaTiO_3$ multilayers studied by x-ray magnetic circular dichroism" *Phys. Rev. B* **89**, 115128 (2014).

(10) K. Yoshimatsu, H. Wadati, E. Sakai, T. Harada, Y. Takahashi, T. Harano, G. Shibata, K. Ishigami, T.

Kadono, T. Koide, T. Sugiyama, E. Ikenaga, H. Kumigashira, M. Lippmaa, M. Oshima, and A. Fujimori, "Spectroscopic studies on the electronic and magnetic states of Co-doped perovskite manganite $Pr_{0.8}Ca_{0.2}Mn_{1-y}Co_yO_3$ thin films" *Phys. Rev. B* **88**, 174423 (2013).

(II) Conference presentations (Only 1st author)

[International]

(1) (poster) <u>T. Harano</u>, Y. Takeichi, M. Usui, R. Murao, and M. Kimura, "The distribution of π-orbital orientation of PAN-based and pitch-based carbon fibers by scanning transmission X-ray microscopy" , Oulu, Finland (2020).

(2) (poster) <u>T. Harano</u>, M. Usui, T. Ohigashi, Y. Takeichi, J. Nakagawa, N. Negi., R. Murao, and M. Kimura, "Visualization of orientation distribution in carbon fibers by scanning transmission X-ray microscopy" International Young Researcher Workshop on Synchrotron Radiation Science (YRSR2019), Hiroshima, Japan (2019).

(3) (poster) <u>T. Harano</u>, Y. Yoshimoto, Y. Takeichi, T. Tanaka, D. Wakabayashi, S. Yamashita, , R. Murao, and M. Kimura, "Chemical State Mapping of Carbon in Tempered Martensite by Scanning Transmission X-ray Microscopy" International Conference X-ray Microscopy (XRM2018), Saskatoon, Canada (2018).

(4) (poster) <u>T. Harano</u>, R. Murao, Y, Takeichi, M. Kimura, and Y. Takahashi, "Observation of the Interface between Resin and Carbon Fiber by Scanning Transmission X-ray Microscopy" International Conference X-ray Microscopy (XRM2016), Oxford, UK (2016).

(5) (poster) <u>T. Harano</u>, K. Ishigami, V.K. Verma, G. Shibata, T. Kadono, A. Fujimori, K. Takedam T. Okane, Y. Saito, H. Yamagami, H. Yamada, A. Sawa, M. Kawasaki, Y. Tokura, and A. Tanaka, "Ru-doped $La_{0.6}Sr_{0.4}MnO_3$ thin film as a coercivity tunable material studied by x-ray magnetic circular dichroism" A3 Foresight Program "Joint Research on Novel Properties of Complex Oxides", Tokyo, Japan (2013).

(6) (poster) <u>T. Harano</u>, G. Shibata, K. Ishigami, V.K. Verma, V.R. Singh, Y. Takahashi, T. Kadono, A. Fujimori, Y. Takeda, T. Okane, Y. Saito, H. Yamagami, H. Yamada, A. Sawa, M. Kawasaki, Y. Tokura, and A. Tanaka, "Electronic and magnetic properties of Ru $4d$ states in the coercivity-tunable material Ru doped La$_{0.6}$Sr$_{0.4}$MnO$_3$" International Conference on Heavy Electrons and Novel Quantum Phases (ICHN 2012), Gyeongju, Korea (2012).

[Domestic]

(1) (poster) <u>原野貴幸</u>, 武市泰男, 大東琢治, 信藤大祐, 根本英治, 若林大佑, 山下翔平, 村尾玲子, 木村正雄, "cSTXM での試料回転ホルダーの開発と炭素 π 軌道配向イメージング" 第 34 回日本放射光学会年会・放射光科学合同シンポジウム, オンライン (2021).

(2) (poster) <u>原野貴幸</u>, 武市泰男, 大東琢治, 信藤大祐, 根本英治, 若林大佑, 山下翔平, 村尾玲子, 木村正雄, "cSTXM 専用試料回転ホルダーの開発" 2019 年度量子ビームサイエンスフェスタ, (2020).

(3) (poster) <u>原野貴幸</u>, 臼井雅史, 大東琢治, 武市泰男, 中川淳一, 禰宜教之, 村尾玲子, 木村正雄, "走査型透過 X 線顕微鏡による炭素繊維内部の配向分布の可視化" 第 79 回 分析化学討論会, 北九州国際会議場&AIM (2019).

(4) (oral) <u>原野貴幸</u>, 村尾玲子, "XRD-Rietveld 法による焼結鉱中結晶相の定量角度の X 線源依存性" 第 177 回 日本鉄鋼協会 春季講演大会, 東京電気大学 千住キャンパス (2019).

(5) (poster) <u>原野貴幸</u>, 武市泰男, 田中智仁, 村尾玲子, 木村正雄, "透過法と転換電子収量法の同時計測による鉄鋼材料中炭素の顕微化学状態イメージング" 2018 年度量子ビームサイエンスフェスタ, つくば国際会議場エポカル (2019).

(6) (poster) <u>原野貴幸</u>, 武市泰男, 田中智仁, 村尾玲子, 木村正雄, "透過法と転換電子収量方の同時 STXM 計測による鉄鋼材料中炭素の化学状態イメージング" 第 32 回日本放射光学会年会・放射光科学合同シンポジウム, 福岡国際会議場 (2019).

(7) (oral) <u>原野貴幸</u>, 村尾玲子, In-Ho Jung, "SFCA 相の熱力学モデルの平衡実験による検証", 第 174

回 日本鉄鋼協会 秋季講演大会, 北海道大学 (2017).

(8) (poster) 原野貴幸, 村尾玲子, 武市泰男, 木村正雄, 高橋嘉夫, "放射光を用いた炭素繊維強化プラスチックの顕微化学状態解析", 日本分析化学会 第 77 回分析化学討論会, 龍谷大学 深草学舎 (2017).

(9) (oral) 原野貴幸, 村尾玲子, 武市泰男, 木村正雄, 高橋嘉夫, "炭素繊維強化プラスチックの顕微化学状態解析", PF 研究会「PF 挿入光源ビームライン BL-19 の戦略的利用に関する研究会」, 高エネ研 小林ホール (2017) .

(10) (poster) 原野貴幸, 村尾玲子, 武市泰男, 木村正雄, 高橋嘉夫, "炭素繊維強化プラスチックの顕微化学状態解析", 第 30 回日本放射光学会年会・放射光科学合同シンポジウム, 神戸芸術センター (2017).

(11) (poster) 原野貴幸, 村尾玲子, 武市泰男, 木村正雄, 高橋嘉夫, "走査型透過 X 線顕微鏡（STXM）による炭素繊維強化プラスチックの樹脂・繊維界面観察", 2015 年度量子ビームサイエンスフェスタ, つくば国際会議場エポカル (2016).

(12) (oral) 原野貴幸, V.K.Verma, 石上啓介, 芝田悟朗, 高橋文雄, 吉松公平, 門野利治, 藤森淳, 小出常晴, F.-H. Chang, H.-J. Lin, D.-J. Huang, C.T. Chen, P.Xiang, 山田浩之, 澤彰仁, 田中新, "基板選択により磁気特性が変化する $Ca_{1-x}Ce_xMnO3$ 薄膜の X 線磁気円二色性", 日本物理学会第 68 回秋季大会, 横浜国立大学 (2012).

(13) (oral) 原野貴幸, 石上啓介, V. K. Verma, 芝田悟朗, 門野利治, 藤森淳, 竹田幸治, 岡根哲夫, 斎藤祐児, 山上浩志, 澤彰仁, 川崎雅司, 十倉好紀, "Ru 置換により保持力が増大した $La_{0.6}Sr_{0.4}MnO_3$ 薄膜の X 線磁気円二色性", 日本物理学会第 67 回 年次大会, 関西学院大学 西宮上ケ原キャンパス (2012).

(14) (poster) 原野貴幸, 石上啓介, V. K. Verma, 芝田悟朗, 門野利治, 藤森淳, 竹田幸治, 岡根哲夫, 斎藤祐児, 山上浩志, 山田浩之, 澤彰仁, 川崎雅司, 十倉好紀, 田中新, "Ru 置換により保磁力を

増強した La$_{0.6}$Sr$_{0.4}$MnO$_3$ 薄膜の X 線磁気円二色性", 第 29 回 PF シンポジウム, つくば国際会議場 エポカル (2012).

(15) (poster) 原野貴幸, 石上啓介, V. K. Verma, 芝田悟朗, 門野利治, 藤森淳, 竹田幸治, 岡根哲夫, 斎藤祐児, 山上浩志, 山田浩之, 澤彰仁, 川崎雅司, 十倉好紀, "Ru 置換により保磁力を増強した La$_{0.6}$Sr$_{0.4}$MnO$_3$ 薄膜の X 線磁気円二色性", 第 25 回 日本放射光学会年会放射光科学合同シンポジウム, 鳥栖市民文化会館・中央公民館 (2012).

(III) Commentary Articles/Reviews

(1) 渡邊稔樹, 武市泰男, 丹羽尉博, 木村正雄, 原野貴幸, 村尾玲子, "放射光 X 線顕微鏡を用いた炭素繊維強化プラスチック (CFRP) の計測", *検査技術* 2021 年 1 月号 (2021).

(2) 原野貴幸, 村尾玲子, 武市泰男, 木村正雄, 高橋嘉夫, "炭素繊維強化プラスチックの顕微化学状態解析", *配管技術* 2018 年 4 月号 (2018).

(3) T. Harano, R. Murao, "Microscopic Chemical-state Analysis of Carbon Fiber Reinforced Plastic by Synchrotron X-radiation", *NIPPON STEEL & SUMITOMO METAL TECHNICAL REPORT*, **118**, 85-89 (2018) .

(4) 原野貴幸, 村尾玲子, "放射光 X 線を用いた炭素繊維強化プラスチックの顕微化学状態解析", *新日鉄住金技報*, **408**, 89-93 (2017) .

(IV) Patents

(1) 渡邊耕太郎, 富士本博紀, 原野貴幸, "ガスシールドアーク溶接用フラックス入りワイヤ、及び溶接継手の製造方法" 特開 2018-192520.

(2) 高橋貴文, 原野貴幸, "水酸化カルシウムの製造方法" 特開 2018-104239.

(3) 原野貴幸, 村尾玲子, "結晶相の質量比率の補正方法" 特開 2018-044855.

(4) 金橋康二, 原野貴幸, 相本道弘, "固溶度の評価方法" 特開 2017-181503.

(V) Awards

(1) Best Poster Award: International Young Researcher Workshop on Synchrotron Radiation Science (Hiroshima, 2019).

(2) 産業界シンポジウム 若手ポスター賞: 日本分析化学会 第 79 回 分析化学討論会（北九州, 2019）.

(3) Best Poster Award: A3 Foresight Program "Joint Research on Novel Properties of Complex Oxides" Tokyo Meeting (Tokyo, Japan, 2013).

(4) Best Poster Award: International Conference on Heavy Electrons and Novel Quantum Phases (ICHN 2012) (Gyeongju, Korea, 2012).

Acknowledgements

It is my great pleasure to express my special gratitude to the following people for their help concerning my doctoral thesis and my life as a scientist and a corporate researcher. First of all, I would like to express my deepest gratitude to Professor Masao Kimura, my supervisor, a senior of Nippon Steel Corporation I have a cordial respect for, for enlightening guidance, constant encouragement, giving a lot of opportunities to participate in international and domestic conferences, teaching me how to advance research and write a paper and so on.

I am also deeply grateful to Assistant Professor Yasuo Takeichi, for teaching me the fundamental principle and technique of scanning transmission X-ray microscopy (STXM) and X-ray absorption spectroscopy (XAS), and how to analyze X-ray absorption images data and plan the experiments using synchrotron radiation X-ray, and so on.

I hope to express my acknowledgement to members of Material Characterization Research Laboratory, Advanced Technology Research Laboratories, Research & Development, Nippon Steel Corporation, especially "Chemical Structure Analysis Research Dept.". I would like to thank Dr. Reiko Murao, Dr. Takafumi Takahashi, Mr. Yuki Hata, Mr. Toru Takayama, Ms. Sonomi, Kawanami, Dr. Keiko Okushita, Dr. Akira Taniyama, Dr. Katsuhiro Nishihara, Mr. Ayuki Yoshizumi, Mr. Takashige Mori, Dr. Takafumi Amino, Dr. Daisuke Itabashi, Mr. Tomohito Tanaka, Mr. Yusuke Kohigashi, Mr. Shunsuke Taniguchi, Mr. Hideto Hiroshima, Ms. Mayuko Kikuzuki, Dr. Junichi Hirata, Mr. Yasuhiro Tobu, Mr. Norihiro Tsuji, and Dr. Michihiro Aimoto for providing me opportunities of conducting studies under the best condition and a lot of useful discussion. Regarding Dr. Reiko Murao, in particular, as my boss, she has been politely and kindly instructing me not only on these studies but also on my daily work in Nippon Steel Corporation.

I would like to express my gratitude here. I am grateful to Mr. Masafumi Usui, Mr. Negi Noriyuki (Nippon Steel Corporation), and Dr. Yutaka Arai (Nippon Steel Corporation , Nippon Steel Chemical & Material Co., Ltd., Nippon Graphite Fiber Corporation) for discussions about carbon fibers.

The STXM measurements were supported by the members of Photon Factory. I am grateful to Dr. Daisuke

Last but not least, my special thanks go to my family (Erika, Yukari, Yukiharu, Akiko, Toshiyuki, Hiroyuki, Kiyoko, Sadao, Fukue, and Yutaka), for their support and love, which cannot be termed in any word on earth.